Technische
Universität
Braunschweig

emg

Sara Nazari Asl

Development of a non-contact EEG hat using textile capacitive electrodes

Dissertation
Braunschweig 2019

Berichte aus dem **Institut für Elektrische Messtechnik und Grundlagen der Elektrotechnik**

Band **66**

Hrsg. Prof. Dr. Meinhard Schilling

Development of a non-contact EEG hat using textile capacitive electrodes

Von der Fakultät für Elektrotechnik, Informationstechnik, Physik
der Technischen Universität Carolo-Wilhelmina zu Braunschweig

zur Erlangung des Grades einer Doktorin

der Ingenieurwissenschaften (Dr.-Ing.)

genehmigte Dissertation

von Sara Nazari Asl, M.Sc.

aus Ghazvin, Iran

eingereicht am:	14.01.2019
mündliche Prüfung am:	05.06.2019
1. Referent:	Prof. Dr. rer. nat. Meinhard Schilling
2. Referent:	Prof. Dr. med. Peter Werning

Druckjahr: 2019

Dissertation an der Technischen Universität Braunschweig,
Fakultät für Elektrotechnik, Informationstechnik, Physik

Kurzfassung

Berührungslose, kapazitive Elektroden für bioelekrische Untersuchungen stellen eine interessante Alternative zu klassischen galvanisch gekoppelten Elektroden dar. Ein solches preisgünstiges Diagnosesystem kann ohne lange Vorbereitungszeit und in mobilen Umgebungen eingesetzt werden. Für gesteigerten Tragekomfort sind textile Elektroden von Vorteil.
In dieser Arbeit wird eine umfassende Beschreibung der elektronischen Rauscheigenschaften und des frequenzabhängigen Verhaltens von sowohl platinenbasierten, als auch textilen kapazitiven Elektroden vorgestellt. Die Einflüsse aller elektronischen Komponenten auf die resultierenden Rauscheigenschaften werden durch Messungen der entsprechenden Rauschspektren untersucht. Die wichtigste niederfrequente Rauschquelle kapazitiver Elektroden stellt der notwendige und zugleich hohe Bias-Eingangswiderstand dar, der in einem $1/f^2$ Rauschleistungsspektrum resultiert. Durch Vergleich der gemessenen Rauschspektren mit dem theoretischen Modell wird die Oberfläche der Elektroden als eine zusätzliche $1/f$-Rauschquelle identifiziert. Dabei ist die größtmögliche Kopplungskapazität vorteilhaft für ein niedriges Rauschen. Deshalb setzen wir im Folgenden Elektroden aus elektrisch leitfähigen Textilien ein. Mit diesen Elektroden ist es möglich, die Oberfläche der Elektrode unter gleichzeitiger Beibehaltung eines kleinen Abstandes zum Körper zu vergrößern. Dies maximiert wiederum die Kapazität. Wir zeigen zudem, dass die Verwendung textiler kapazitiver Elektroden die Rauscheigenschaften deutlich verbessert.
Desweiteren wird in dieser Arbeit die Konstruktion eines kapazitiven, berührungslosen EEG-Helmes (cEEG-Mütze) mit sieben Kanälen beschrieben. Dieser Helm profitiert von den guten Rauscheigenschaften der zuvor entwickelten und hier integrierten textilen Elektroden. Die gemessenen Rauschspektren zeigen ein niedriges Rauschen mit einer Spannungsrauschdichte von $10\,\mu V/\sqrt{Hz}$ bei 1 Hz und sogar $1.5\,\mu V/\sqrt{Hz}$ bei 20 Hz. Dies erfüllt viele Voraussetzungen für die Messung von Gehirnsignalen.
Die erstellte cEEG-Mütze lässt sich während langer Messzeiten und Schlafperioden angenehm tragen. Im Gegensatz zu herkömmlichen Methoden ermöglicht sie Messungen außerhalb von Laboratorien und im gewohnten Umfeld. Alle in dieser Arbeit gezeigten Schlafmessungen wurden in einer normalen Wohnung aufgezeichnet. Außerdem wird die Einsatzmöglichkeit für sogenannte "Gehirn-Computer-Schnittstellen" anhand der Messung von "steady state visually evoked potentials" (SSVEP) Signalen bei verschiedenen Frequenzen demonstriert.

Abstract

Non-contact capacitive electrodes for bioelectric diagnostics provide an interesting alternative to classical galvanically coupled electrodes. Such a low cost diagnostic system can be applied without preparation time and in mobile wireless environments. For even higher user comfort textile capacitive electrodes are preferable.
In this work, a comprehensive model for the electronic noise properties and frequency dependent responses of PCB-based, as well as textile non-contact capacitive electrodes, is presented. A thorough study of the influence of the electrical components on the resulting noise properties of these electrodes, is provided by independently measuring the corresponding noise spectra. The most important low frequency noise source of capacitive electrode is the necessary high input bias resistance, which in combination with the input capacity, results in an apparent $1/f^2$-power noise spectrum. By comparing the noise measurements with the theoretical noise model of the electrode, it is concluded that the surface of the electrode contributes to an additional $1/f$-power noise. It is also found that the highest possible coupling capacitance is most favorable for low noise behavior. Therefore, we implemented electrodes with electrically conducting fabric surfaces. With these electrodes, it is possible to enlarge the surface of the electrode while simultaneously maintaining a small distance between the body and the electrode over the whole surface area, thus maximizing the capacitance. We also show that the use of textile capacitive electrodes, reduces the noise considerably.
Furthermore, this thesis describes the construction of a capacitive non-contact textile electroencephalography measuring hat (cEEG hat) with seven measuring channels. This hat benefits from the low noise characteristics of the integrated developed textile capacitive electrodes. The measured noise spectrum of this cEEG hat shows low noise characteristics with a voltage noise density of $10\,\mu V/\sqrt{Hz}$ at 1 Hz and $1.5\,\mu V/\sqrt{Hz}$ at 20 Hz. This fulfills many requirements for measuring brain signals.
The implemented cEEG hat is comfortable to wear during very long measurements and even during sleep periods. In contrast to common methods, the cEEG hat provides a possibility of measuring EEG signal during sleep outside laboratories and in the comfort of home. EEG sleep measurements shown in this work, are recorded inside a normal apartment. The possibility of brain computer interface application is also shown by measuring steady state visually evoked potentials (SSVEP) at different frequencies.

Acknowledgements

This thesis would have been impossible without the aid and support of many people. Therefore, I would like to send my sincere thanks to:

- Prof. Schilling for giving me the opportunity of this PhD work and mentoring me during this time and for his support, understanding and brilliant ideas.
- Prof. Werning for being my second examiner.
- Prof. Ludwig for being the examination presidency and for his support in writing papers.
- B-IGSM for the financial support and providing nice and fruitful lectures, workshops and summer schools.
- Kerstin Franke for making my PCBs and being ready to try new and challenging methods.
- Tanja Coenen for preparing all the photos and posters during my work.
- Ralf Behme for his technical support.
- The workshop of the institute: Hartmut Müller, Jan Pförtner, and Harald Schmidt for their aid in construction of my measurement setup.
- all my lovely colleagues at the EMG that I will immensely miss in the future.
- my students: Lautaro Petrauskas, Maurice Walz, Claas Lennart Pudwell for their measurements and helps.
- Felix Pirch for being my test person for SSVEP measurements.
- my officemates Katharina Olze and Ilya Elenskiy for the nice time, helpful discussions and their supports in German language.
- my friends for their mental support and the nice time that I always have by being with them.
- my family: my parents and my siblings for their unconditional love and for believing in me and supporting me spiritually throughout my life.
- Last but not the least, my fiance, Dr. Michael Martens who brightened my heart and my life with his love and who supported this work brilliantly with intelligent discussions and proofreading.

Glossary

ADC	analog to digital converter
AEP	auditory evoked potential
A/D	analog-to-digital
BCI	brain computer interface
cEEG	capacitive electroencephalography
DFT	discrete Fourier transformation
ECG	electrocardiography
EEG	electroencephalography
EMG	Institute of Electrical Measurement Science and Fundamental Electrical Engineering
ENBW	effective noise equivalent bandwidth
EOG	electrooculogram
EP	evoked potential
FFT	fast Fourier transform
ICA	independent component analysis
IF	intermediate-frequency
LS	linear spectrum
LSD	linear spectral density
NENBW	normalized equivalent noise bandwidth
NREM	nonrapid-eye-movement
PCB	printed circuit board
PLA	polylactic acid
PS	power spectrum
PSD	power spectral density

REM	rapid-eye-movement
RAS	reticular activating system
rms	root mean square
SEM	scanning electron microscope
SPI	serial peripheral interface
SSEP	somatosensory evoked potential
SSVEP	steady state visually evoked potential
SWS	slow wave sleep
USART	universal synchronous/asynchronous receiver transmitter
VEP	visual evoked potential
VBW	video-bandwidth

Symbols

A_e	m^2	electrode surface area
B	Hz	bandwidth
C	F	capacity
C_air	F	air gap capacity
C_e	F	electrode capacity
$C_\mathrm{insulator}$	F	dielectric capacity
C_OA	F	input capacitance of operational amplifier
C_sh	F	parasitic capacitance
d	m	diastance
ϵ_0	F/m	vacuum permittivity
ϵ_r	F/m	dielectric permittivity
f	Hz	frequency
f_c	Hz	cutoff frequency
f_Ny	Hz	Nyquist frequency
f_res	Hz	frequency resolution
f_s	Hz	sampling frequency
I_dc	A	average dc current
I_sh	A	shot noise current
k	J/K	Boltzman's constant
q	C	electron charge
Q	C	electric charge
R	Ω	resistance
R_e	Ω	electrode resistance
R_bias	Ω	bias resistance
R_in	Ω	input resistance
R_OA	Ω	input resistance of operational amplifier
R_sh	Ω	parasitic resistance
$\sqrt{S^O_\mathrm{IOA}}$	$\mathrm{V}/\sqrt{\mathrm{Hz}}$	current noise of opamp at the output
S_v	V^2/Hz	power spectral density
$\sqrt{S_\mathrm{v}}$	$\mathrm{V}/\sqrt{\mathrm{Hz}}$	linear spectral density
$\sqrt{S_\mathrm{VFOut}}$	$\mathrm{V}/\sqrt{\mathrm{Hz}}$	total voltage noise at the output
$\sqrt{S^O_\mathrm{VOA}}$	$\mathrm{V}/\sqrt{\mathrm{Hz}}$	voltage noise of opamp at the output
$\sqrt{S_\mathrm{VOut}}$	$\mathrm{V}/\sqrt{\mathrm{Hz}}$	voltage noise at the output
$\sqrt{S^O_\mathrm{VRbias}}$	$\mathrm{V}/\sqrt{\mathrm{Hz}}$	voltage noise of bias resistor at the output
$\sqrt{S^O_\mathrm{VRe}}$	$\mathrm{V}/\sqrt{\mathrm{Hz}}$	output voltage noise of electrode resistor
T	K	temperature

$V_{\mathbf{eff}}$	V	effective voltage
$V_{\mathbf{LSB}}$	V	least significant bit voltage
$V_{\mathbf{max}}$	V	maximum voltage
$V_{\mathbf{min}}$	V	minimum voltage
$V_{\mathbf{rms}}$	V	rms voltage

Contents

1 Introduction

In the year 1924, Hans Berger recorded the first human electroencephalogram. This measurement technique is commonly used in the diagnosis of brain illnesses, sleep disorders, depth of anesthesia, coma, encephalopathies, and brain death [1–6]. Novel applications of electroencephalography (EEG) measurements increased the interest in it during recent years. Some of these important applications are: brain computer interface (BCI), robotic rehabilitation of patients, and the investigation of brain development [7–15].

EEG measurements are mostly done in hospitals and medical clinics with the use of contact wet electrodes. The process of measuring EEG signals by using these electrodes, is time consuming and complex. It has to be done under supervision of professionals. In this process, the head must be cleaned and the electrodes should be connected to the head with the help of conductive gel. This gel may dry out during the measurement, causing some measurement artifacts, and should usually be washed off from the head after the measurements. EEG measurements during sleep are even more complicated and uncomfortable for the patients. The patients should stay for a long time at the hospital or medical clinic while staying awake the whole first night. In this way, they are able to sleep afterwards despite being attached to the EEG measuring system.

The use of disposable galvanic Ag/AgCl-electrodes for each patient for hygienic reasons, increases the cost per diagnosis and produces tons of waste. This, in addition to the effort needed for EEG measurements with galvanic electrodes, has motivated many scientists to introduce new methods that are more effortless, time efficient, integrable in every day life, and appropriate for long-term measurements. [16–23] Among all the solutions, capacitive non-contact electrodes for measuring brain signals can offer significant advantages. With these electrodes, bio-signals can be measured through insulating materials like clothes or hair, no preparation

is needed prior to the measurement, they are integrable within clothes for every day bio-signal monitoring and long-term measurements. Moreover, these electrodes do not need to be kept wet, have no storage problems, and can always be available in regions with less infrastructure. [23–36]
Capacitive electrodes are usually constructed in a similar way, following proposals made in the middle of the last century [37, 38]. Afterwards, they have been gone under many improvements by several research groups [39–43].
The capacitive non-contact electrodes can be characterized by the coupling capacitance to the body through dielectric material and an air gap. This capacitance can be enlarged with a larger electrode surface, which is possible to achieve by using textile conductive surface for the electrode. [43–45] Moreover, textile capacitive electrodes are effortlessly integrable in clothings and offer more comfort to the users and patients.

Capacitive non-contact electrodes have been implemented in EEG and ECG (electrocardiography) measuring systems. [46–49] Textile capacitive non-contact electrodes in the ECG measurement area, are employed in the investigation of the driver's health while driving, and are implemented in car seats. [34, 50–52] These textile capacitive non-contact electrodes are proposed for implementation of an EEG hat [43].

Despite the benefits of using capacitive electrodes for measuring bioelectric signals, they are not commonly used for measuring nano-volt signals of the brain. This is due to their noise signal characteristics [53–56]. Since, the noise of these electrodes is normally high in the microvolts regime at low frequencies ($< 50\,\mathrm{Hz}$), it impedes the recording of some brain signals, which are occurring in the same frequency and voltage range.
Motivated by this, the presented work deals with the investigation of noise characteristics of capacitive and textile capacitive non-contact electrodes in details to introduce a comprehensive noise model for them. This provides a fundamental knowledge for understanding and further development of these electrodes. It is also shown that the noise voltage density of textile capacitive electrodes is quite low in comparison to rigid capacitive electrodes [43].
This thesis also presents the advantages of textile capacitive non-contact electrodes, and describes the implementation of a capacitive EEG (cEEG) hat.

In chapter 2, necessary information and background of the work is presented. In section 2.1, fundamental information about bioelectric signals, brain anatomy and its waves, and sleep patterns, which are required for understanding the subsequent measurements, are described. Section 2.2 focuses on the methods of the EEG measurements. In this section, different measuring EEG systems and electrodes are described with the emphasis on capacitive non-contact electrodes and previously implemented capacitive helmet systems at the institute of Electrical Measurement Science and Fundamental Electrical Engineering (EMG). Section 2.3 explains possible noise sources of these electrodes and the coupling noise sources in the

environment. In addition, digital signal processing which is needed for the evaluation of the measurements, is included in section 2.4. In chapter 3, the implemented setup and systems in this thesis are described including a noise measurement setup for the noise measurements of the capacitive electrodes, textile capacitive electrodes, and textile capacitive EEG hat. Chapter 4 includes the results in two main parts: the first part introduces a comprehensive noise model for capacitive electrodes by considering all the noise sources and their effect on the noise spectrum. The second part presents the noise characteristics of the cEEG hat, the evaluation method for the measurements, and different measurements, which are done with the cEEG hat. The thesis is concluded with a summary and outlook for future improvements in chapter 5.

2 Background and previous work

In this chapter, the theoretical background for the understanding of this thesis is provided. In addition, former developed non-contact capacitive helmet systems for electroencephalography in EMG institute, are presented.

2.1 Neurophysiological foundations

This section provides the medical and biological basics needed to understand the measurements done in this work. First, the origin of biosignals and the anatomy of the brain are presented, followed by EEG measurement, the resting rhythm of the brain, sleep patterns, and the signal response, which can be observed after an external stimulus.

2.1.1 Origin of bioelectric signals

Bioelectric signals are mainly generated by muscles and nerves due to diffusion and active transport of ions in the cells and nerve cells, which generates potential differences across the cell membrane. The origin of the membrane voltage is the same in muscle cells as in nerve cells. The membrane generates an impulse as a reaction to excitation, which propagates in both cell types in a same manner. The resting potential of the internal cell medium lies in the range of $-90\,\mathrm{mV}$ to $-40\,\mathrm{mV}$ (approximately $-70\,\mathrm{mV}$ in most cells), relative to the external medium around the cell. This negative potential is caused by concentration differences of potassium ions K^+ and sodium ions Na^+ inside and outside the cell, which happens due to the permeability of the resting membrane to K^+ and Cl^-, and the operation of sodium-potassium pumps. The concentration differences create a diffusion gradient that is directed outward across the membrane. [57]
The voltage- and time-dependent nature of the membrane permeabilities to K^+ and Na^+, generates an active potential. In this case, the sudden

rush of sodium ions to the cell, increases the potential (depolarization). Afterwards, with a short delay, the release of potassium ions brings the level of the differential potential low again (repolarization). The potential change of the transmembrane during an action potential, is shown in figure. 2.1. [57]

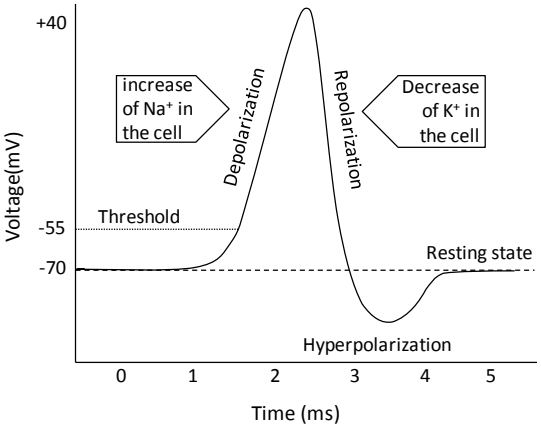

Figure 2.1: Transmembrane potential and membrane ionic conductance changes for sodium and potassium during the action potential.[58]

Nerve cells can be divided into three parts: cell body, dendrites, and axon. The body of the nerve cells is similar to that of other cells. The dendrites receive impulses from other cells and transfer them to the cell body. The axon transfers the action potential from the cell body to another nerve or a muscle cell as illustrated in figure 2.2. [57]

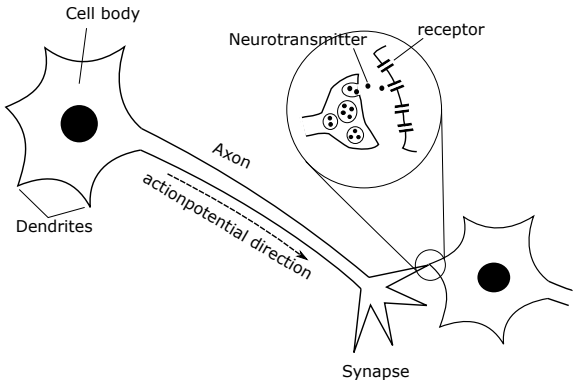

Figure 2.2: Signal transfer in between neurons via neurotransmitters, after [59].

2.1.2 Anatomy and function of the brain

The brain is the greatly modified and enlarged portion of the central nervous system located in the skull. The brain is divided into three main parts: cerebrum, brainstem, and cerebellum (see figure 2.3). The brainstem serves three major functions: (1) a connecting link between the cerebral cortex, spinal cord, and cerebellum; (2) an integrative center for several visceral functions (e.g., control of blood pressure and ventilation); and (3) an integration center for various motor reflexes. The cerebellum is the coordinator in the voluntary muscle system and works together with the brainstem and cerebral cortex to maintain balance and provide harmonious muscle movements. The conscious functions of the nervous system are localized within the cerebrum, which occupies a special dominant position in the central nervous system. [57, 60]
For EEG measurements, only the cerebrum plays a role since all the other parts of the brain are enclosed by it. Therefore, they are shielded from the EEG electrodes and cannot provide a contribution to the measurement signal. For this reason, they will not be discussed further in this work.
The cerebrum comprises 10 billion neurons in a strongly folded configuration, giving it a surface area of about $2\,\mathrm{m}^2$. The folded surface consists of sulci (grooves) and gyri (ridges). The cerebrum divides into two hemispheres that can communicate with each other through the corpus callosum, and four areas called lobes; the occipital, temporal, parietal, and frontal lobe.
Each of these four lobes has its own tasks, though, there is some functional overlap between them and for each task different parts of the brain may communicate with each other. The visual center, the so called visual cortex, is located in the occipital lobe. For the interpretation of what is seen, however, the frontal lobe, the parietal lobe, and the temporal lobe are accessed. [57, 60]

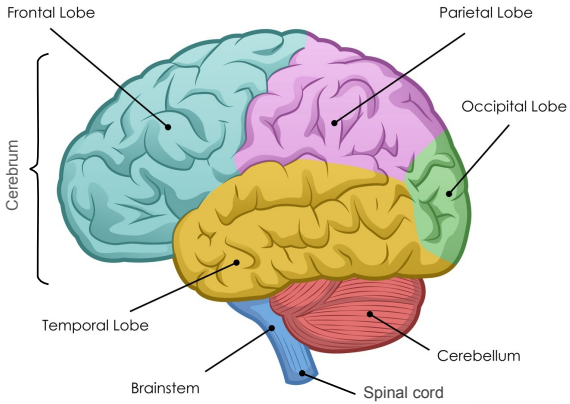

Figure 2.3: Simplified sketch of the brain showing four areas of the cortex, as well as the cerebellum and brainstem.[57]

2.1.3 The electroencephalogram

EEG plots cerebral activities as voltage versus time graphs. The foundations for today's EEG measurement were established in 1924 by the German physician Hans Berger with the first measurement of human brain signals. [61] The electrical activities are received from the electrodes, which are attached to the scalp. Today, the signals are digitized with analog to digital converters. The digital signals can then be filtered to reduce artifacts and then plotted in time domain.
The difficulty in receiving brain electrical activities from the scalp is the overwhelming electrical activities of other parts of the body (like the scalp muscles, eyes, tongue, and even heart) or electrical disturbances from the environment.
The most used system to mount the electrodes for monitoring the clinical EEG is the international federation 10–20 system shown in figure 2.4. There are different types of electrode installation. One is the bipolar installation, which in this case, each channel measures the difference between two adjacent electrodes. The second one is called referential installation. Here, each channel measures the difference between one electrode and a reference electrode. There is also an average reference installation, in which each channel measures the difference between one electrode and the average of all other electrodes, and a Laplacian installation, where each channel measures the difference between one electrode and a weighted average of the surrounding electrodes. The benefit of differential measurement in referential installation, is the reduction of disturbances and noise

that are common for all the electrodes. For that reason, the EEG helmet built in this work, uses the this method in which each channel compares one electrode with a reference electrode. [57, 62]

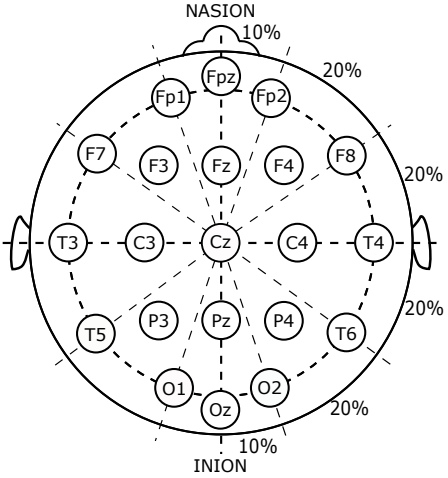

Figure 2.4: Electrode locations of the international 10-20 system for EEG recording. The head is shown from above with the nose on the upper side.[63]

2.1.4 Resting rhythm of the brain

The EEG recordings of the brain present continuous oscillating electric activity within the brain. These electric activities are called *brain waves*. The intensity and patterns of this electric activity are mostly determined by the overall excitation of the brain, resulting from functions in the brainstem reticular activating system (RAS).
The intensities of the brain waves on the surface of the brain can reach amplitudes of 10 mV, however those recorded from the scalp have a smaller amplitude of approximately 100 µV. The brain waves characteristics are strongly dependent on the degree of activities of the cerebral cortex. Therefore, the waves change significantly between states of wakefulness and sleep. Usually, the brain signals are irregular without any general observable pattern. Although, some brain abnormality may cause distinct patterns, such as in epilepsy. Others occur in normal persons and may be classified as belonging to one of five wave groups, which are explained below. [57, 64]

- Delta waves (0.1 – 4 Hz)
  Delta waves have the lowest frequency, though, highest amplitude. They represent the activity of the gray matter of the brain. They are found in all stages of sleep especially in stage 3 and 4 (see section 2.1.5). Delta waves are abnormal for adults, who are awake.

- Theta waves (4 – 8 Hz)
  Theta waves are related to subconscious activities. These occur mostly in the parietal and temporal regions in children, but they also occur during emotional stress in some adults, especially during periods of disappointment and frustration.

- Alpha waves (8 – 13 Hz)
  Alpha waves are seen commonly in adults, who are awake but relaxed with closed eyes. Their voltage is approximately between 20 µV and 200 µV. When the person is asleep, the alpha waves disappear completely. When the awake person's attention is directed to some specific type of mental activity, the alpha waves are replaced by asynchronous waves with higher frequency but lower amplitude. They represent the white matter of the brain and act as a bridge between conscious and subconscious states. They occur on both sides of the head though with slightly higher amplitude on the non dominant side and can be recorded from the occipital and parietal regions of the brain.

- Beta waves (13 – 30 Hz)
  Beta waves are related to behavior, actions, and senses. They usually can be recorded in both sides of the frontal and parietal lobes. Beta waves occur in active brain states like talking, problem solving, judgment, and decision making.

- Gamma waves (30 – 100 Hz)
  Gamma waves occur during hyper alertness with integration of

sensory inputs. Gamma waves indicate the combination of senses with memory activity.

The brain wave patterns are unique for each individual. It means, in some cases, distinguishing persons only according to their typical brain activities, is possible. For example, subjects, who are regarded as rational types or as intuitive types, may demonstrate certain higher activities in their frontal left and frontal right hemispheres respectively. [57, 64]

2.1.5 Sleep patterns

During normal state of wakefulness with open eyes, beta waves are dominant. In relaxation or drowsiness, alpha activity rises and during sleep, the power of lower frequency bands increases. When a person becomes drowsy and falls asleep, the alpha waves are replaced with other waves, which are higher in amplitude though lower in frequency. The EEG during drowsiness contains alpha and delta waves. In deep sleep, large, irregular delta waves are observed.
The average length of the sleep cycle in an adult man is 90 minutes [63, 65]. During a sleep cycle, the person is either in a rapid-eye-movement (REM) or nonrapid-eye-movement (NREM) sleep. The REM sleep occurs when the high amplitude low frequency waves are replaced by a rapid low voltage irregular activity similar to the awake state activities without sleep interruption. During this time the person has rapid eye movements. On the other hand, the NREM is a synchronized sleep. This sleep is classified as light NREM (stages 1–2), and deeper slow wave sleep (SWS, or stages 3–4). N1 (NREM stage 1) is when the person is drowsy or awake to falling asleep. Brain waves and muscle activity start to decrease at this stage. The EEG of stage 1 sleep contains theta and alpha waves in a frequency range of 4 Hz to 13 Hz with an appearance of vertex waves. N2 denotes the state, when the person experiences a light sleep. Eye movement has stopped before this stage. Brain wave frequency, heart rate, body temperature, and muscle tonus are decreased. The EEG of stage 2 contains more delta waves and shows sleep spindle related features. N3 or even N4 are the most difficult stages to be awakened. During this time, every part of the body is relaxed, breathing, blood pressure and body temperature are reduced [66]. The EEG of stage 3 has even more delta waves though less spindles. [57, 62, 63]
Dreaming happens during paradoxical or REM sleep and thermoregulation occurs normally during NREM sleep. Therefore, alternation between the stages maintains body temperature within an acceptable range. Approximately, 75% of the night is spent in NREM sleep and 25% in REM sleep. The transition between NREM and REM is abrupt in humans [57, 63].

2.1.6 Evoked potentials

Besides the normal activities of the brain that are mentioned above, it is also possible to change the potential in the EEG by external stimuli, which are then called event-related potentials. In addition to the potentials evoked by cognitive processes, the evoked potentials (EPs) are of particular importance because they are reproducible. The evoked potentials are differentiated according to the type of stimulus. There are three kinds of evoked potentials in widespread clinical use: auditory evoked potentials (AEP), usually recorded from the scalp but originating at brainstem level; visual evoked potentials (VEP), and somatosensory evoked potentials (SSEP), which are extracted by electrical stimulation

of peripheral nerves. In this work, only the visually evoked potentials are analyzed, which will therefore be explained in more detail. [38]
Visual evoked potentials are elicited by a flashing light or changing pattern on a monitor. This stimulus evokes a transient signal shown in figure 2.5 with the first positive peak at 100 ms, which can be seen in the EEG in the related area to the occipital cortex. [67]

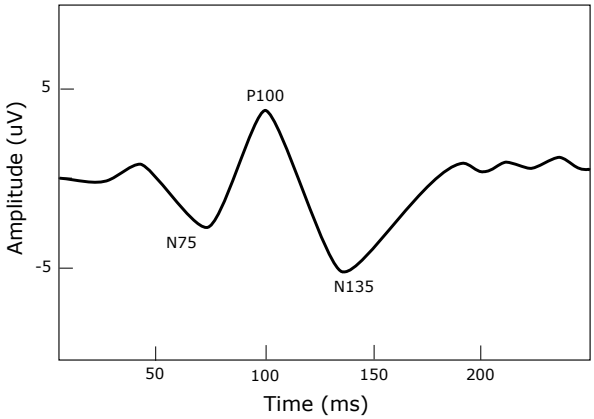

Figure 2.5: EEG recording of a visual evoked potential. The first positive peak is at 100 ms in between two minimums at 75 ms and 135 ms [68].

This transient signal appears in every stimulation. However, if the stimulation frequency is increased typically to frequencies higher than 6 Hz, the transient individual responses change to a steady state, which is then referred to as SSVEP (Steady State Visual Evoked Potential). The SSVEP is composed of a number of discrete frequency components. The frequency range associated with the SSVEPs normally includes the stimulation frequency as well as its harmonics. From about 40 Hz (proband dependent), however, this signal disappears again, because the eye can no longer resolve individual events. [69, 70]

2.2 EEG measuring devices

Common EEG measurement devices consist of bioelectric measuring electrodes to receive electrical signals from the scalp, analog-to-digital (A/D) converters, a processor, and a recorder. The main differences between these devices, from the hardware point of view, are the electrodes and connection method of different stages, which can be via cable, or wireless via bluetooth. [47, 49, 62]
The input electrodes are problematic in the routine recording of clinical EEGs. They have to be small, easily attachable to the scalp with minimal disturbance by the hair, they must cause no discomfort, and they must remain in place for extended periods of time.
In this chapter, bioelectric measuring electrodes are introduced with the focus on the capacitive electrodes. This is followed by a description of the EMG institute's EEG helmets.

2.2.1 Bioelectric measuring electrodes

The electrodes can be galvanic (wet or dry), capacitive or hybrid - a combination of galvanic and capacitive. The wet electrodes are made of silver/silver chloride (Ag/AgCl) materials and utilize an electrolytic gel to form a conductive path to the skin. Such electrodes are widely used in medical applications. Dry electrodes consist of normal metals, like stainless steel, and in this case no electrolyte is used. Capacitive electrodes consist of a metal, semiconductor, or conductive fabric with a thin dielectric surface layer, so that the bioelectric signal is capacitively coupled from the skin. [71]
In general, the electrodes are interfaces between ion based potentials of the body and electron based potentials of the electronic devices. On the interface between the electrode surface and the body, an insulating barrier called *Helmholtz electric double layer*, can appear, because the charge carriers on both sides accumulate at the interface. Therefore, an electric field is imposed on the barrier. The resulting change in the electrode potential at the double layer is called polarization. In this case, almost no charge exchange will take place and the behavior of the polarized electrodes is considered capacitive. Though, the resulting capacity is not always the same and it depends on the ion concentration inside the body. [26, 72]
Commonly used electrodes are non polarized, which means the charge carriers can move from one side to the other. These non polarized electrodes consist of metal salt materials to provide ions on both sides. The use of electrolyte in between the electrode and skin, supports this transmission. For each positive ion from the electrode side that solves into the electrolyte, one electron will be freed to transfer the electric charge. The most common metal/metal salt combination is Ag/AgCl which shows a minor polarization. The jellylike consistency of the electrolyte acts as a damper, hence, the measurements are less susceptible to motion artifacts. [71]
On the other hand, the use of galvanic electrodes in measuring EEG signals, suffers some disadvantages: the time consuming and laborious

procedure of the electrode installation (which contains degreasing the recording area, applying a conductive paste, gluing and fixing the electrodes on the head), temporary detachments of the recording electrodes called “electrode pop” artifact (which can further erode the EEG, or even imitate brain rhythms and seizures), and a vast usage of disposable electrodes. [57, 62]
Capacitive electrodes use another measuring principle and stay isolated from the body. Therefore, they do not need any electrolyte material. Instead, they have a thin dielectric material to form a capacitor between the body and electrode surface. The interesting advantages of these electrodes and their characteristics are discussed in the following.

Capacitive electrodes

With capacitive electrodes, biological signals can be measured through insulating materials like hair or clothes. They are especially interesting for long term diagnostics, since they don’t need any electrolytes, which dry out over time. This type of electrodes is usually constructed in a similar way, following proposals have been made in the middle of the last century. [37, 73] The common geometric arrangement of a capacitive electrode for bioelectric potential measurements is depicted in figure 2.6.

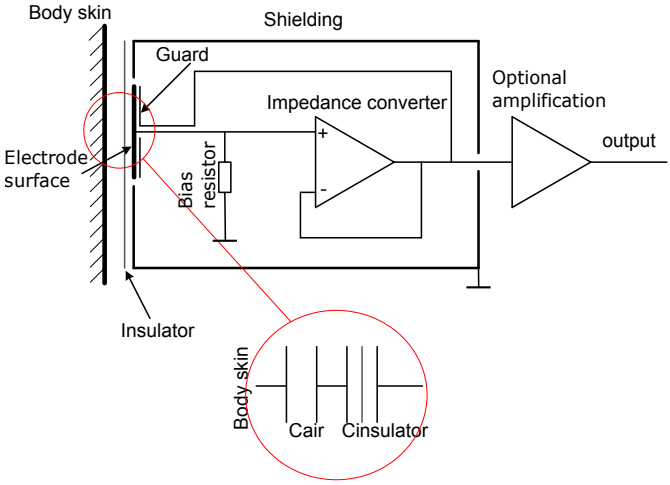

Figure 2.6: Block diagram of a capacitive electrode. The formed capacity between the electrode and skin is magnified. [43]

A capacitive electrode for bioelectric potential measurements consists of a measuring, printed circuit board (PCB) connected to a piece of conductive material, which forms a capacitor together with the body surface. The electric charges on the body surface, caused by the electric

body potentials, interact with corresponding charges in the conductive surface of the electrode.
In parallel to the electrode surface, another layer with the same potential exists to eliminate electrical couplings to the other side of the electrode surface. This layer called *guard* and is separated from the electrode surface with an insulation material.
The electrode is placed over the body surface and separated by some insulating material and an air gap. For an air gap capacitor (relative permittivity(ϵ_r) = 1) with $d = 1\,\text{mm}$ distance of the electrode from the body surface, a capacitance C_e per area A_e is about

$$C_\text{e}/A_\text{e} = \frac{\epsilon_0 \epsilon_r}{d} = 8.854 \times 10^{-13}\,\text{F/cm}^2. \tag{2.1}$$

ϵ_0 is the permittivity of the vacuum.
This air gap capacity C_air dominates the total electrode capacitance in a series connection with the second capacitor $C_\text{insulator}$ ($1/C_\text{e} = 1/C_\text{air} + 1/C_\text{insulator}$). The reason for this is that in C_air, ϵ_r is equal to one and in $C_\text{insulator}$, which contains other dielectric materials, it is more than one. This means $C_\text{insulator}$ is larger than C_air.
The size of the electrical current dipolar sources together with their depth inside the body results in a size of the electrodes between $A_\text{e} = 1\,\text{cm}^2$ and $A_\text{e} = 5\,\text{cm}^2$. If these capacitive electrodes are only made of rigid materials like FR-4 glass epoxy in PCBs, the distance d depends on the position of the electrode on a body, especially if it is placed on a head. Therefore, A_e is not the geometric area but an effective area which is the partial area with a minimum distance to the body. The capacitance C_e is 8.8 pF for $A_\text{e} = 10\,\text{cm}^2$.
This capacitance is part of an electronic high pass filter, together with the input resistance R_in of the circuit. The cutoff frequency f_c of this filter should be low enough to let the physiologically interesting frequency components pass. Normally, the lower frequency limit is chosen at 0.1 Hz in agreement with the bandpass filters used commonly in ECG or EEG [63]. This requires the capacity C_e or the input impedance R_in to be chosen high enough to provide the desirable cutoff frequency. The capacity of the common rigid surface electrodes cannot be easily increased, therefore, for the normal requirements ($C_\text{e} = 3\,\text{pF}$, $f_c = 0.1\,\text{Hz}$) the input resistance has to be

$$R_\text{in} \geq \frac{1}{2\pi \cdot f_c \cdot C_e} = 530 \times 10^9\,\Omega. \tag{2.2}$$

In figure 2.7, a simplified equivalent circuit diagram of the capacitive electrodes is shown.
The input capacitance C_OA and input resistance R_OA of the impedance converter and a parasitic conductance $1/R_\text{e}$ between the body and the electrode, which could easily be of the same order of magnitude as R_OA, are also included to the equivalent circuit diagram. Additionally, an

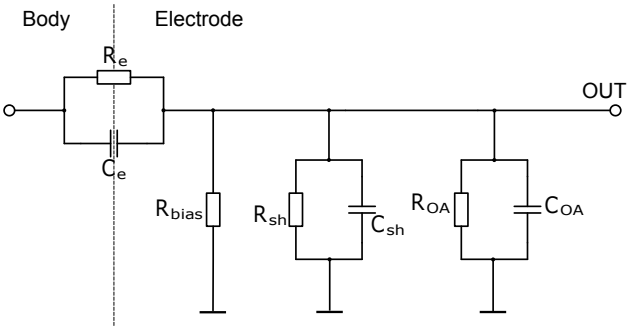

Figure 2.7: Equivalent circuit diagram of the electrode determining the frequency response. [47]

intentionally introduced bias resistor R_{bias} is included, which is needed to prevent the input of the amplifier from charging with its input bias current. Without this bias resistor, the operational amplifier would get saturated. The parasitic conductance $1/R_{\text{sh}}$ and parasitic capacitance C_{sh} of the electrode relative to the surrounding shielding enclosure have to be taken into account for a complete equivalent circuit diagram. The impedance converter can be realized by an appropriate operational amplifier with corresponding input resistance R_{OA} and capacitance C_{OA}. It can be seen from this equivalent circuit diagram that the parasitic capacitance C_{sh} and the capacitance C_{OA} are required to be considerably small. Otherwise, the capacitive voltage divider consisting of C_{e} and $C_{\text{OA}} \parallel C_{\text{sh}}$ reduces the measured voltage signal significantly. This capacitive voltage divider, even with a very small C_{OA}, always reduces the received voltage by a factor of $\frac{C_{\text{e}}}{C_{\text{e}}+C_{\text{OA}}\parallel C_{\text{sh}}}$. Therefore, it is clear that with a larger value of C_{e}, the receiving voltage from this stage will be less reduced.[27, 43, 47]
Also note that R_{in} is equal to R_{bias} since $R_{\text{in}} = R_{\text{bias}} \parallel R_{\text{OA}}$ and R_{bias} is significantly lower than R_{OA}.

Flexible capacitive electrodes

In principle, flexible capacitive electrodes are similar to the rigid capacitive electrodes but with flexible surfaces. This surface can be made from any conductive flexible material such as: conductive fabrics, conductive polymer foam, etc [44, 74]. The flexible surfaces of this electrodes make them comfortable to wear and provide a possibility of using them inside clothes for long term, every day monitoring of biosignals. In these electrodes, the input capacity C_{e} is larger than in rigid electrodes with the same surface size.
The distance between the curved surface of the body and electrode surface differs unpredictably in the rigid PCB-based capacitive electrodes. It varies from one electrode to another due to their different positions on

the body. Therefore, the introduced capacitance is difficult to specify. In contrast to these electrodes, textile capacitive electrodes can fit to the body curvature and provide a constant large capacitance at the input. This results in a smaller average effective distance and the geometric surface would be equal to the effective area. Regarding this fact, it is also possible to estimate the amount of C_e. Moreover, it is possible to provide a larger surface while maintaining a constant distance between the electrode and the body by using these electrodes. Therefore, textile capacitive electrodes provide higher input capacitance compared to rigid electrodes [44].

2.2.2 Capacitive EEG helmets

The EMG institute at TU Braunschweig, has utilized capacitive electrodes in implementing several measuring helmets. These are shown in figure 2.8. The use of these helmets is easy and very time efficient, because no preparation is required prior to the measurement.

(a) The first prototype of capacitive EEG helmet consisting of 28 measuring electrodes. The electrodes are positioned inside a motor-cycle helmet and it is connected via wire to the A/D converter box.[47]

(b) The second prototype of the capacitive EEG helmet consisting of 8 measuring electrodes. The electrodes are situated inside a gaming helmet. They are connected via wire to the A/D converter box.[47]

(c) The third prototype of the capacitive EEG helmet also consists of 8 measuring electrodes. The electrodes, A/D converter, and battery are situated inside a gaming helmet. This EEG Helmet communicates with a computer via bluetooth.[49]

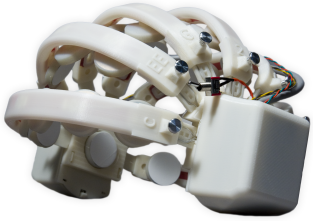

(d) The fourth generation of capacitive EEG helmet consisting of 25 measuring electrodes. This helmet is 3D printed and is adjustable to different sizes of heads. It is also wireless and the communication happens via bluetooth.[46]

Figure 2.8: Four generations of capacitive EEG helmets with rigid capacitive electrodes.

The used electrodes in these helmets employ a high-pass filter and low-pass filter in addition to the intrinsic high-pass filter at the input. The additional high-pass filter with a cutoff frequency of 200 mHz, suppresses very low, unwanted frequencies and the DC part of the measured signal.

The low-pass filter eliminates the probable high frequency coupling to the electronics and wires with a cutoff frequency of 159 kHz. In addition to the filters, the electrodes have an amplification by a factor of two. The electrodes are 28 mm in diameter and are individually shielded with an aluminium casing mounted on top of them. The rest of the system is not shielded.
There is a reference electrode in all the measuring helmets, which is located at the front part of the helmet. The measurement results of the other electrodes compare to this electrode in the instrumentation amplifier stage. Therefore, only the difference between the electrodes and reference electrode is amplified. In this case, some common disturbances among the electrodes and reference electrode, will be decreased. The amplification factor in this stage is equal to 100.
After the instrumentation amplifiers, signals are sent to A/D converters. This stage is either directly on the same PCB as the instrumentation amplifier, which is the case in wireless helmets, or is separated from the helmet and receives the signals via cable. Then, a microcontroller gathers the digitized signals and sends them to a computer via cable or bluetooth for further analysis.
For more information on these capacitive EEG helmets, refer to publications [46–49].

2.2.3 EEG artifacts

Due to the low amplitude of the EEG signals and high sensitivity requirements of brain signal measurements, various biological or technical artifacts may occur. [62, 75]

- The electrooculogram (EOG), which is the corneo-retinal standing potential that exists between the front and the back of the human eye, is superimposed to the EEG measurements in the frontal area.
- All muscle activities e.g. in the neck or jaw area couple as electromyography in the measurement signal. This can be reduced by training the patient.
- The ECG also leads to artifacts. This artifact can be detected and suppressed with the help of a simultaneous ECG recording. It can be also filtered electrically or in the software retrospectively.
- Sweating, which can affect the contact resistance of the electrodes and provoke artifacts, can be prevented by regulating the climate in the examination room.
- Interference from the outside into the system, which can be reduced or suppressed by proper design of the shielding, amplifiers, and by using appropriate filters.
- The electrolytic gel used for contact electrodes, can also cause artifacts by being applied in large amount or drying out during the measurement.

2.3 Noise and signal

The term noise is commonly used in practice instead of the term spontaneous fluctuations. The spontaneous fluctuations of electric charges, which exist in all conductors, produce random variation of the potential between the ends of the conductor. Electrical noise is significantly a problem in sensitive electrical circuits. It limits the resolution of an electrical circuit to the point at which the signal-to-noise ratio is below acceptable limits [76].
In this section, the relevant noise sources for this work, noise spectral density, the function of a spectrum analyzer, and a signal processing method for evaluation of the noise measurement results, are discussed.

2.3.1 Noise sources

For capacitive electrodes in biosignal measurements, which should be able to measure microvolt range brain signals, the noise should be considerably lower than a few microvolts. A list of possible noise sources in capacitive electrodes are mentioned below. In addition, the relevant ones are described in more details.

2.3.2 Intrinsic noise sources

The common intrinsic noise sources can be listed as bellow [76, 78]:

- Shot noise
  It is associated with current fluctuations. It normally occurs when electric charges pass a potential barrier, like a p-n junction in semiconductors, and also when electron-hole pairs generate or recombine randomly.
- Thermal noise
  The thermal agitation of electrons in passive resistive elements causes the thermal noise. This noise is also referred as Johnson or, Nyquist noise.
- Flicker noise
  This is also known as 1/f noise or excess noise. The spectral density of various conductors that decreases inversely proportional to frequency, shows the existence of flicker noise.
- Burst noise
  Also called popcorn noise. It occurs due to the defects in semiconductor junctions, usually in a form of metallic impurities, and it can only be eliminated by improving the manufacturing process.
- Avalanche noise
  It occurs in the p-n junctions if they are in the reverse breakdown operational mode. The strong reverse electric field gives the electrons enough kinetic energy that the random collusion between them and the atoms of the crystal produces more electron-hole pairs.

- Contact noise
  This noise occurs when there is fluctuating conductivity in between two conductor materials in imperfect contacts, such as in relays and switches.

Shot noise

Shot noise is associated with the current flow, as W. Schottky showed theoretically in 1918. [77] His proposed equation is as follows:

$$I_{sh} = \sqrt{2qI_{\mathrm{dc}}B}, \tag{2.3}$$

where q is the electron charge, I_{dc} is the average DC current, and B is the noise bandwidth. The shot noise is a white noise, which means its power density is constant over frequency. By dividing equation 2.3 by the square root of bandwidth we have:

$$\frac{I_{sh}}{\sqrt{B}} = \sqrt{2qI_{dc}} = 5.66 \times 10^{-10} \sqrt{\mathrm{A/Hz}} \cdot \sqrt{I_{dc}}. \tag{2.4}$$

From equation 2.4, it can be seen that the noise current per square root of Hz is only a function of average DC current passing through the device. Therefore, to obtain the amount of this noise, the DC current flowing through the device should be measured. Shot noise is independent of temperature.

Thermal noise

The thermal noise is also white noise, since the frequency distribution of its noise power is uniform. This noise is independent of the flowing current through the passive resistance. Although, it depends on the temperature and resistance. The root mean square (rms) noise voltage produced by a resistance R is equal to:

$$V_t = \sqrt{4kBTR}. \tag{2.5}$$

Where k is the Boltzman's constant, T is the absolute temperature in Kelvin, B is the noise bandwidth, and R is the resistance in Ω. The thermal noise of the resistor can be represented by adding an equivalent voltage or current source to the circuit as shown in figure 2.9.
This noise source exists in every resistance independent of its composition. For example, thermal noise of a 100Ω tantalum thin-film resistor exhibits the same amount of noise as a 100Ω carbon resistor. A resistor may show more noise than just thermal noise due to other noise sources but it exhibits never less noise.

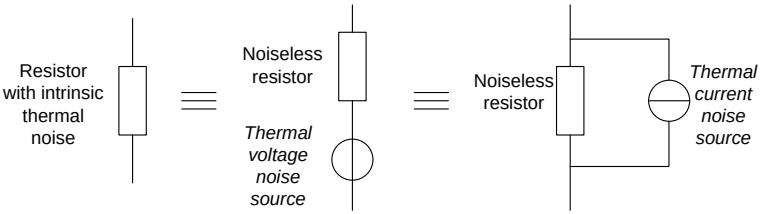

Figure 2.9: The equivalent circuits of a resistor with intrinsic thermal noise. The thermal noise source can be represented by a voltage source of $\sqrt{4kTBR}$ or current noise source of $\sqrt{4kTB/R}$.

Flicker noise

Unlike white noise, Flicker noise depends on frequency. Its power spectrum shows a 1/f-like slope towards lower frequencies. Flicker noise exists in all active devices and is originated from various sources. It is based on electron fluctuation in the conductance and can be associated with DC current flowing through the device.
All resistors show to some extent 1/f noise differing for different types. Since this noise is proportional to the DC current in the device [76], by maintaining the current low enough, the thermal noise will be the dominating noise source in the resistors.

Since burst noise, avalanche noise, and contact noise, are not relevant noise sources in our capacitive electrodes, they wont be discussed further in this thesis.

2.3.3 External coupled noise sources

As important as intrinsic noise sources in the electrodes, are external noise sources coupled from the environment. To eliminate and reduce these noise sources, the possible coupling approaches have to be understood. [78]

Conductively coupling noise

This is one of the most common coupled noise in electrical circuits. It occurs when the noise in the environment couples into the wiring especially the connecting wires. In this way, the wire collects the noises and transmits it to another circuit. The noise conducted to the circuit through power supply leads belongs to this category. The solution for this problem is decoupling the wire before connecting to the circuit. For that reason, we used a one to one transformer in between our measuring instruments and power line to eliminate the noise coupling to the measurement setup.

Coupling through Common Impedance

This happens when two circuits are connected to the same ground or power supply. In this way, the current from these circuits will flow through a common impedance (see figure 2.10). The voltage drops over the common impedance, caused by the current of one circuit, influences the other circuit. Therefore, the noise of one circuit couples to the other circuit.

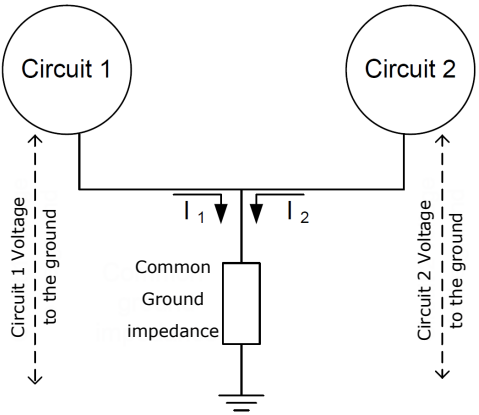

Figure 2.10: Two circuits with common ground impedance. The noise in one circuit couples via its current to the other circuit.[78]

Electric and Magnetic fields

The movement of charges through conductive materials radiates electromagnetic fields, which can couple to the other circuits as a noise signal. Similarly, electrical fields can couple capacitively to the circuit. In addition to these unintentional radiations, there are intentional radiated magnetic signals of transmitters.

Ground loop (Inductively coupling noise)

The ground loop may be formed when multiple electrical circuits are connected to the same ground. In effect, a closed loop forms as shown in figure 2.11. The existing ambient electromagnetic fields, for instance in the vicinity of electric power wiring, can couple by electromagnetic induction to the ground loop and induce a current. Therefore, the ground loop acts as a receiver of electromagnetic disturbances in the environment. To avoid this problem, the ground loop should be broken by means of some isolating transformer or discriminating device.

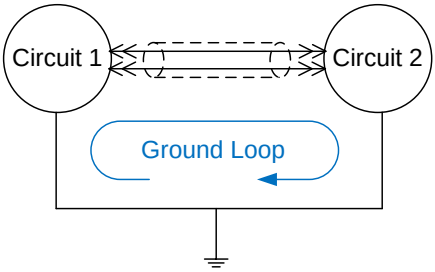

Figure 2.11: A typical ground loop formation between two circuits.[78]

2.3.4 Noise spectral density

Noise spectral density or noise power density is the power spectral density of noise or the noise power per unit of bandwidth. Spectral analysis is one of the most important signal processing techniques and consists of identifying the spectral content of a time-varying quantity. In principle, power spectral density (PSD) is a Fourier transformation of the auto-correlation function of the signal in time domain. A power spectral density has units of V^2/Hz or $V^2 s$. [79] The calculation of the discrete power spectral density is described in section 2.4.5.

2.3.5 Spectrum analyzer

For the better perception of the measurement results presented in this work, basic understanding of a spectrum analyzer is required.
Spectrum analysis is a type of measurement that preserves the amplitude and frequency information of sinusoidal components of a signal, though, ignores the phase information for spectral density. Each time signal can be developed into a superposition of sine waves, which are called spectrum. Figure 2.12 shows this concept.
The investigation of the frequency domain is especially useful for reconstruction of the harmonic components of a signal and inter-modulated distortions. Spectrum analysis is especially practical in noise measurements. It shows unwanted power of electric and electromagnetic disturbances coupled to the electronics in addition to the intrinsic power noise of the electronics itself. [80]
Commercially available spectrum analyzers are either analog, partially digital, or all-digital. The analog spectrum analyzer, also called superheterodyne analyzer, measures the amplitude only. This spectrum analyzer is suitable for higher frequencies above the audio range. A simplified block diagram of this type is shown in figure 2.13.

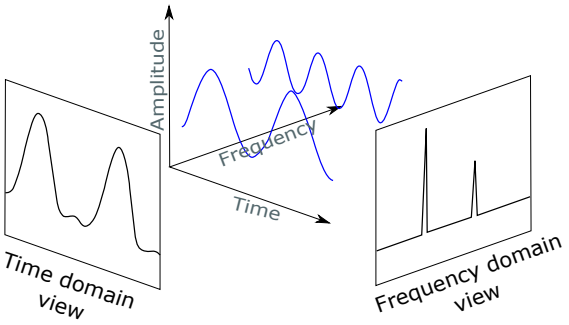

Figure 2.12: Relationship between time and frequency domain for periodic signals.[81]

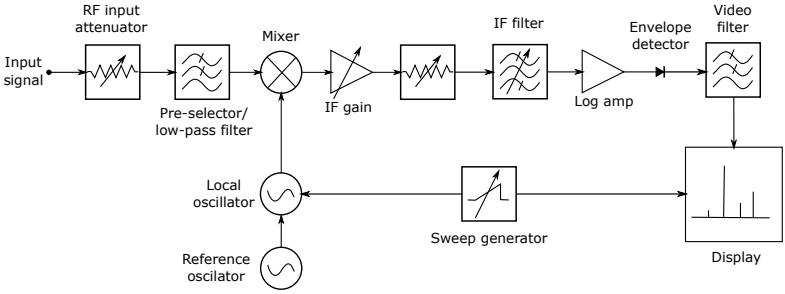

Figure 2.13: Block diagram of an analog spectrum analyzer.[80]

The input signal first goes through an attenuator to ensure an optimum input level of the signal into the mixer to prevent overload, gain compression and distortion. The low-pass filter prevents out-of-band signals from mixing with the local oscillator and creating unwanted responses. It can be replaced with a preselector in microwave spectrum analyzers, which is a tunable filter that rejects all undesired frequencies. The mixer mixes the filtered signal with a signal from the local oscillator. The mixing is a non-linear process, therefore its output includes not only the two original signals, but also their harmonics and the sums and differences of the original frequencies and their harmonics. The pass band of the intermediate-frequency (IF) filter eliminates these nonlinearity effects of the mixer. The envelope detector essentially rectifies the signal. Then after, the signal is filtered through the low-pass filter and displayed. A ramp generator creates the horizontal movement across the display from left to right. The ramp also tunes the local voltage controlled oscillator so its frequency change is proportional to the ramp voltage. [80]
In partially digital spectrum analyzers, some parts of the device, especially in the IF section, are replaced with digital circuits shown in figure 2.14.

Partially digital spectrum analyzers are faster, and more accurate in comparison with the analog versions. They have the ability to measure complex signals and also at lower frequencies. [80]

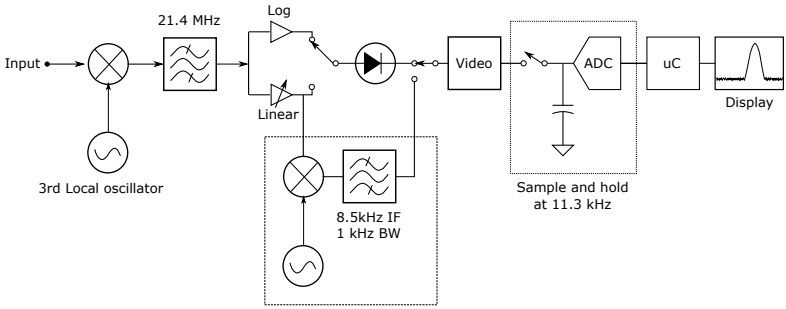

Figure 2.14: Block diagram of a partially digital spectrum analyzer.[80]

The all digital IF spectrum analyzer optimizes sweeps for the fastest measurements with combination of fast Fourier transform (FFT) analysis for narrow spans and swept analysis for wider spans. The digital spectrum analyzers can also keep the phase informations. In figure 2.15, the block diagram of an all digital IF spectrum analyzer is shown.

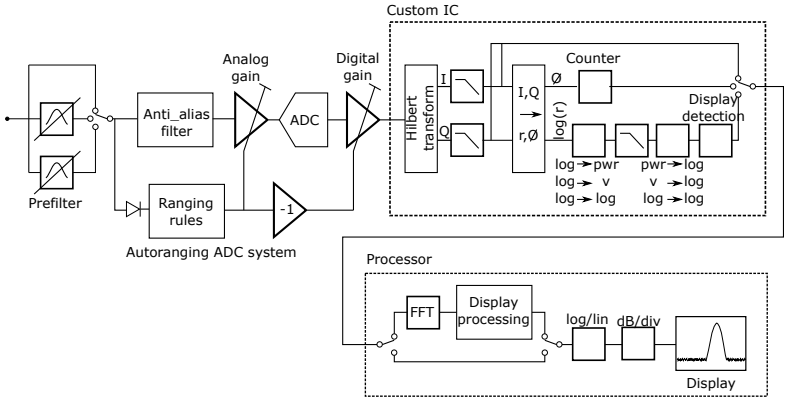

Figure 2.15: Block diagram of an all digital IF spectrum analyzer.[80]

This spectrum analysis begins with analog prefilters, which prevent producing third order distortions by succeeding stages. The anti-aliasing filter prevents the entrance of out-of -band signals into the ADC. It also has a delay of more than three cycles of the ADC clock, which makes it possible to detect an incoming large signal with an auto range detector

and to decrease the gain in front of the ADC. The digital gain after ADC compensates the analog gain before it. The custom IC splits the signal in two signals (I, Q) with half the rate of the original. The resulted signal is also filtered to achieve a narrower bandwidth. The filtered I and Q pairs, are then converted to magnitude and phase pairs. The magnitude signal is filtered with a video-bandwidth (VBW) filter, which is a low-pass filter to remove noises from the envelope and create a smoother display. Then samples are taken through the display detector circuit. At the end, computing the FFT, scaling, and display selection, occur inside the processor. [80]
In this work, an all digital IF spectrum analyzer of type Agilent 35670A, is used.

2.4 Digital signal processing

The estimation of the Fourier transform and spectral density of digital signals is considerably different from that of analog signals. Although, these calculations are rather straightforward, there are normalizations and scaling that should be considered in practice. [79, 82–85] Since the analog signals received from the capacitive electrodes in the EEG hat introduced in this work, are converted to digital data for further processing with a computer, it is necessary to regard the required considerations in data analysis of these digital signals.
A sinusoidal signal in time x(t) with a frequency of 17 Hz and an amplitude of 1 μV_{rms} is considered as an example signal in this section. The sampling rate of this signal is considered to be 500 Hz in agreement with the sampling rate of the introduced EEG hat in this thesis.
The power spectral density shows the power distribution of a time series against frequency. Mathematically, it is the Fourier transformation of the autocorrelation sequence of the time series. It has a unit of V^2/Hz. The *linear* spectral density is the square root of the *power* spectral density and has a unit of $V/\sqrt{Hz}$. In this work, for power spectral density the symbol S_V and for linear/voltage spectral density the symbol $\sqrt{S_V}$ is used. The important relation between power spectral density and the rms fluctuation of voltage V_{rms} in the frequency range of $f_1 \leq f \leq f_2$ is [83]:

$$V_{\mathrm{rms}} = \sqrt{\int_{f_1}^{f_2} S_{\mathrm{V}} df}. \tag{2.6}$$

2.4.1 A/D conversion

The binary data received from the measuring instrument are the digitized biosignals from the analog to digital (A/D) converter. Therefore, the first necessary scaling factor is the back-conversion of the received bits in binary to the original format of Volts. For this purpose, the binary signed integer data convert to floating point numbers by multiplying with the factor [83]:

$$V_{\mathrm{LSB}} = \frac{V_{\mathrm{max}} - V_{\mathrm{min}}}{2^n}. \tag{2.7}$$

Where V_{LSB} is the voltage corresponding to the least significant bit, n is the number of bits or effective resolution of the A/D converter and V_{max} and V_{min} are the highest and lowest voltage bins. Here, 2^{n} is the number of intervals that the measurement range is divided into.
The maximum peak value and root mean square (rms) amplitude of an input signal that can be digitized, are given by:

$$V_{\mathrm{max,pk}} = \frac{2^n}{2} \cdot V_{\mathrm{LSB}} = 2^{n-1} \cdot V_{\mathrm{LSB}}. \tag{2.8}$$

$$V_{\mathrm{max,rms}} = \frac{V_{\mathrm{max,pk}}}{\sqrt{2}} = \frac{2^{n-1}}{\sqrt{2}} V_{\mathrm{LSB}}. \tag{2.9}$$

The A/D converter represents continuous (analog) voltages perfectly as long as they are integral multiples of V_{LSB}. Any intermediate input voltage will cause the A/D converter to produce a best estimate digital data value. The inaccuracies in this process are called *quantization errors/noise*, because an A/D output least significant bit is an indivisible quantity. This situation is illustrated in figure 2.16.

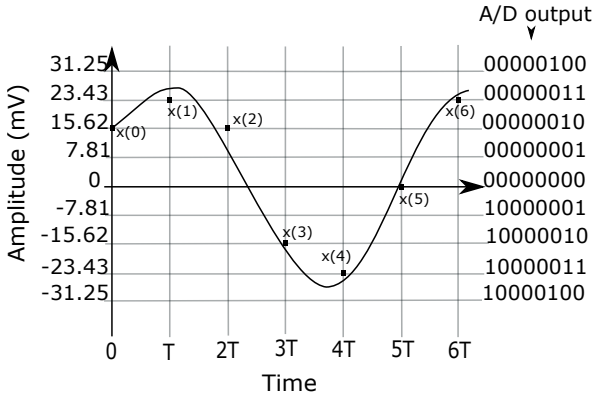

Figure 2.16: A/D quantization error in time domain for 8-bit A/D converter with sampling point T. For the measurement with an input signal voltage range of ±1 V, the least significant bit represents 7.81 mV. [86]

An example for the quantization noise of a 24bit A/D converter with $V_{\mathrm{LSB}} = 0.054\,774\,\mu\mathrm{V}$ in time and frequency domain is illustrated in figure 2.17.
The noise linear spectral density of A/D converter is given by:

$$\sqrt{S_{\mathrm{V,A/D}}} = \frac{V_{\mathrm{LSB}}}{\sqrt{6 \cdot f_s}}, \tag{2.10}$$

where f_s is the sampling frequency. This noise level, like V_{LSB}, is inversely proportional to the number of bits of the A/D converter. [83, 86].

2.4.2 Discrete Fourier Transformation (DFT)

The DFT is a discrete sequence of the Fourier transform of a signal rather than a function of a continuous variable. It corresponds to equally spaced frequency samples. The DFT generates a vector of N complex numbers y_m, m=0....N-1 from a vector of N complex numbers x_k, k=0...N-1. There

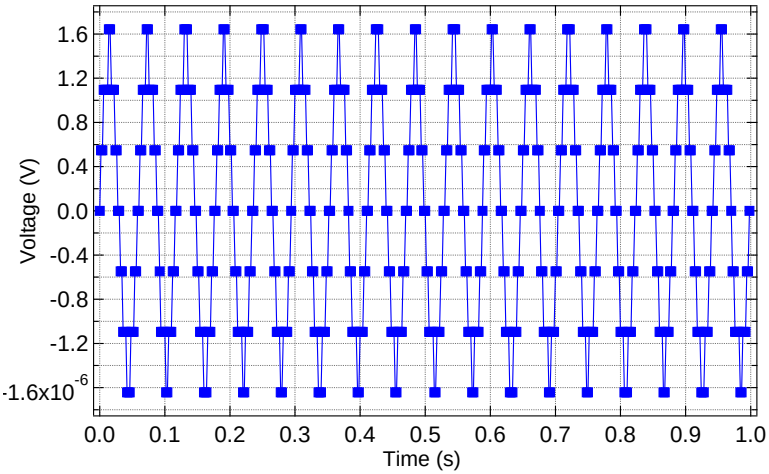

(a) Output signal of A/D converter in time domain including quantization noise.

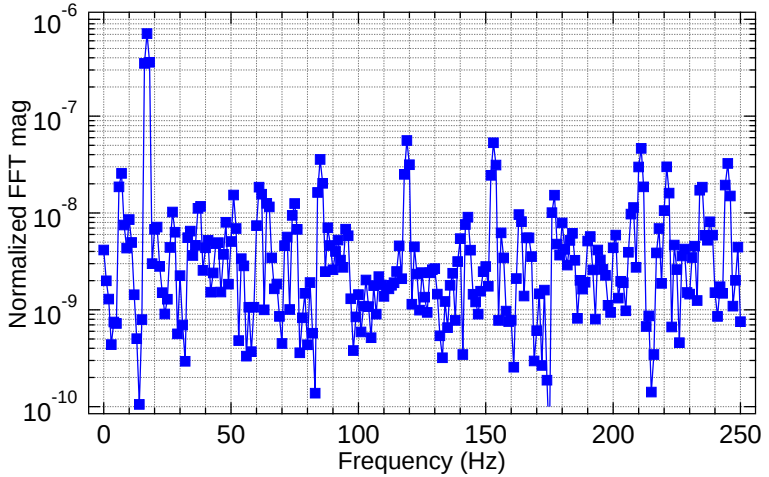

(b) Quantization noise in frequency domain.

Figure 2.17: Simulated output signal of 24 bit A/D converter with $V_{\mathrm{LSB}} = 0.054\,774\,\mu\mathrm{V}$ in time domain and its FFT conversion to show the quantization noise in time and frequency domain. The signal has the voltage rms of $\pm 1\,\mu\mathrm{V}$ and the frequency of 17 Hz.

are commonly three different methods of forward DFT calculations that differ in the normalization factors. [79, 85]

- $$y_m^{(1)} = \sum_{k=0}^{N-1} x_k \exp\left(-2\pi j \frac{mk}{N}\right), \quad m = 0...N-1, \tag{2.11}$$

  Most FFT subroutine packages use formula 2.11 for computer based DFT calculations.

- $$y_m^{(2)} = \frac{1}{\sqrt{N}} y_m^{(1)}, \tag{2.12}$$

  This is the only symmetrical way to define forward and backward DFT (the backward DFT has a different sign of the exponent $2\pi i \frac{mk}{N}$) that can produce the original data by applying the forward and backward DFT successively.

- $$y_m^{(3)} = \frac{1}{N} y_m^{(1)}. \tag{2.13}$$

  This will simplify the calculation of the spectrum. Because, this formula makes the amplitude of the signal independent from N. Normally, with increasing N, $y^{(1)}$ receives more signal and in the same frequency interval, the amplitude increases proportionally to N.

The use of equation 2.11 and 2.13 on our sinusoidal test input signal with 1 µV amplitude and 17 Hz frequency is shown in figure 2.18.
The time series of the digitized input signal are real numbers, though, they are considered as complex numbers in the general definition of the DFT with imaginary part equal to zero. Therefore, the following relationship is true for the output array y^m:

$$y_{N-m} = y_m^*, \tag{2.14}$$

where $*$ denotes complex conjugation. Mathematically, when N is even, y_0 and $y_{N/2}$ are real. Therefore, in most of the FFT computing packages, the upper half of the array, $y_{N/2+1}...y_{N-1}$, is redundant and not computed. For that reason, in this section and later on in receiving signals from the EEG hat, the number of the points N is always considered to be even.
The amplitude of the DFT is a non-negative real number, which is the absolute value of the complex number of the DFT output.[82, 83]

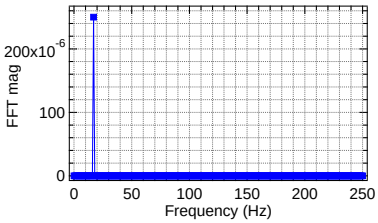

(a) Calculated DFT using equation 2.11 for a sampling time of one second and $N = 500$.

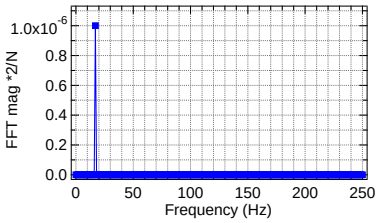

(b) Calculated DFT using equation 2.13 for a sampling time of one second and $N = 500$. Factor 2 results from not computing the negative frequencies in DFT.

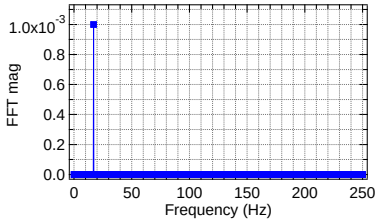

(c) Calculated DFT using equation 2.11 for a sampling time of four seconds and $N = 2000$.

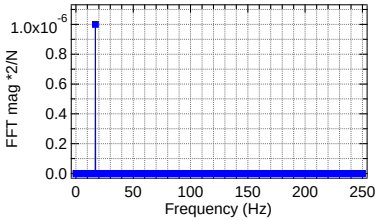

(d) Calculated DFT using equation 2.13 for a sampling time of four seconds and $N = 2000$. Factor 2 results from not computing the negative frequencies in DFT

Figure 2.18: In (b) and (d), the normalized output of equation 2.13 produces a signal in the frequency domain with the same amplitude as the time domain signal, which is in this case 1 µV regardless of the number of input samples N. Sampling frequency is considered as 500 samples per second. In contrast, (a) and (c) used the non-normalized formula 2.11.

2.4.3 Sampling time and frequency bins

The DFT transformation converts N numbers of input data to N number of output, regardless of the sampling frequency f_s. This sampling frequency should essentially be considered for a correct interpretation of DFT results. From the Nyquist theorem, the maximal useful frequency (Nyquist frequency) is half of the sampling rate of a discrete signal processing system. With a fixed sampling rate, the only possibility to increase the frequency resolution f_{res}, is by increasing the length N of the DFT. The resolution is given by:

$$f_{\text{res}} = \frac{f_s}{N}. \tag{2.15}$$

Note that this frequency resolution is not the same as the ability of separating two nearby peaks in the spectrum, which is also called frequency resolution.
The DFT produces $\frac{N}{2} + 1$ distinct complex numbers corresponding to the frequencies:

$$f_m = m f_{\text{res}}, \quad m = 0...\frac{N}{2}. \tag{2.16}$$

Therefore, $\frac{N}{2}$ frequency bins with the resolution of $\frac{f_s}{N}$ will be obtained in the output practically. There is no loss of information because the output of the DFT are complex numbers while the input time signal samples are real numbers.
The first and last element of the obtained output, y_0 and $y_{N/2}$, have no imaginary part. This is due to the fact that y_0 corresponds to the DC average of the signal and $y_{N/2}$ corresponds to the Nyquist frequency $f_{N/2} = (N/2)f_{res} = f_s/2 = f_{Ny}$, which has also no imaginary number according to equation 2.11 for $m = N/2$ of the imaginary sinusoidal component.[83]

2.4.4 Window function

The input signal to be processed can be of some adjustable or selectable extent, however, this extent must be necessarily finite. Because otherwise, the power will spread across the spectrum and for instance it won't be a sharp peak in one frequency bin for a sinusoidal signal. The reason for this is the DFT assumption that the signal is periodic, which means the time series of length N repeats itself infinitely. In this case, when the frequency of the periodic input signal is not an exact multiple of the frequency resolution f_{res}, the DFT will perceive discontinuity between the last sample and the first sample of the next data package due to the cyclic continuation.

To avoid this problem, the input signal in time region should be multiplied with a 'window function' before applying the DFT. The window functions start at zero or near to it, then raise to maximum at the center of the time series, and afterwards descend again. Thus the use of window functions eliminates the discontinuity, it usually involves some compromises. These compromises usually include the width of the resulting peak in the frequency domain, amplitude accuracy and the 'spectral leakage', which means a given spectral component at $f = f_0$ will contribute output at another frequency $f = f_a$ according to the gain of the window centered at f_0 and measured at f_a.[83, 87]
There are different window functions. The Hanning window as one of them is commonly used in noise and vibration measurements purposes, which has been also used in this thesis.

Hanning window

The Hanning window has reasonably low spectral leakage and bandwidth therefore it has been used as standard window function in many commercial spectrum analyzers. To apply a window function, the time series $x_j, j = 0...N-1$ is multiplied by window function w_j before performing the DFT.
The effect of the Hanning window on the example input sinusoidal signal is shown in figure 2.19b. The Hanning window (shown in figure 2.19a), is defined as follow:

$$w_j = \frac{1}{2}\left[1 - \cos\left(\frac{2\pi \cdot j}{N}\right)\right]; \quad j = 0...N-1. \tag{2.17}$$

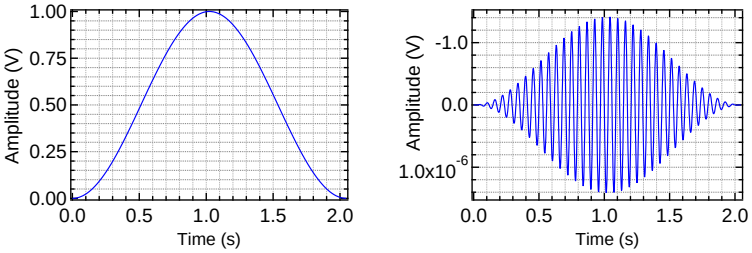

(a) (b)

Figure 2.19: (a) The Hanning window in the time domain, and (b) The effect of Hanning window on sinusoidal signal.

For an even length N, the Hanning window has the symmetry of:

$$w_j = w_{N-j}. \tag{2.18}$$

There are also two summation values that are used for normalization of the final results as follow:

$$S_1 = \sum_{j=0}^{N-1} w_j, \tag{2.19}$$

$$S_2 = \sum_{j=0}^{N-1} w_j^2. \tag{2.20}$$

The normalized equivalent noise bandwidth (NENBW) of the window in frequency domain is:

$$NENBW = N\frac{S_2}{(S_1)^2}. \tag{2.21}$$

The effective noise bandwidth (ENBW) can be written as:

$$ENBW = NENBW \cdot f_{\mathrm{res}} = NENBW \cdot \frac{f_{\mathrm{s}}}{N} = f_{\mathrm{s}}\frac{S_2}{(S_1)^2}. \tag{2.22}$$

The NENBW is equal to 1.5 bins for the Hanning window. The measurement results should be divided by this equivalent noise bandwidth when they are to be expressed as spectral density. [83, 87]

2.4.5 Normalized power spectrum and power spectrum density

Assume the complex vector y_{m} of length $N/2+1$ is the FFT conversion of the multiplication of the input time series x_j of length N with the window function. [85] The power spectrum (PS) interpretation of the resulting FFT, expressed as V_{rms}^2, is calculated as follow:

$$PS_{\mathrm{rms}}(f_{\mathrm{m}} = m \cdot f_{\mathrm{res}}) = \frac{2{\cdot}|y_{\mathrm{m}}|^2}{S_1^2}; \quad m = 0...N/2. \tag{2.23}$$

A resulting power spectrum of an example digitized sinusoidal signal with A/D converter and after applying Hanning window, is shown in figure 2.20. Both the length of N of the DFT and the gain of the window function are included in the S_1 factor. Using the efficient FFT algorithm that does not compute the redundant results for negative frequencies, results in appearing factor 2 in the equation. The desired power spectral density

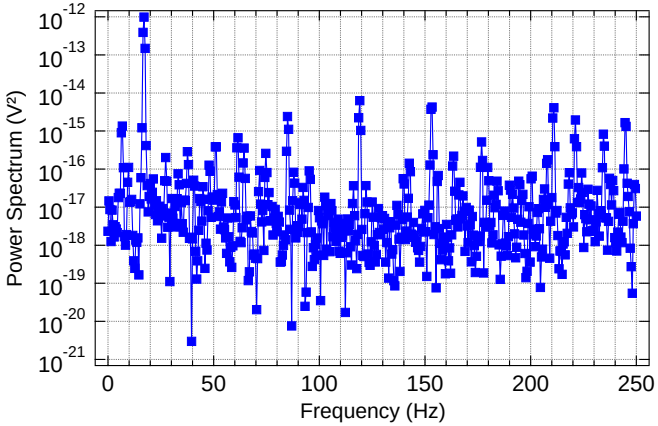

Figure 2.20: The power spectrum of a sinusoidal signal (1 µV amplitude, 17.1 Hz frequency) after applying Hanning window and with consideration of quantization noise of the A/D converter.

expression in V^2/Hz of the results, is obtained by dividing the power spectrum by effective noise equivalent bandwidth as follow:

$$PSD_{\mathrm{rms}}(f_m = m \cdot f_{\mathrm{res}}) = \frac{PS_{\mathrm{rms}}(f_{\mathrm{m}})}{ENBW} = \frac{2 \cdot |y_{\mathrm{m}}|^2}{f_{\mathrm{s}} \cdot S_2}; \quad m = 0...N/2. \tag{2.24}$$

A resulting power spectral density of an example digitized sinusoidal signal with A/D converter and after applying Hanning window, is shown in figure 2.21.
In the normalization according to equation 2.23, the amplitude of the peak of the input signal, remains constant by changing the length of N. The amount of white noise in the spectrum, however, varies inversely proportional to N. The reason is that the width of one frequency bin reduces by increasing N and, consequently, less white noise power will be contained in one frequency bin. This effect can be compensated by using equation 2.24 for computation of power spectral density. As a result, the constant level of white noise independent from N will be obtained. The peak of the signal, however, increases with the increase of N. As is shown in figure 2.22.[83]
Further processing of the output in obtaining a linear spectrum (LS) (expressed in V) or linear spectral density (LSD) (expressed in $V/\sqrt{Hz}$), is as follow:

$$LSD = \sqrt{PSD}, \tag{2.25}$$

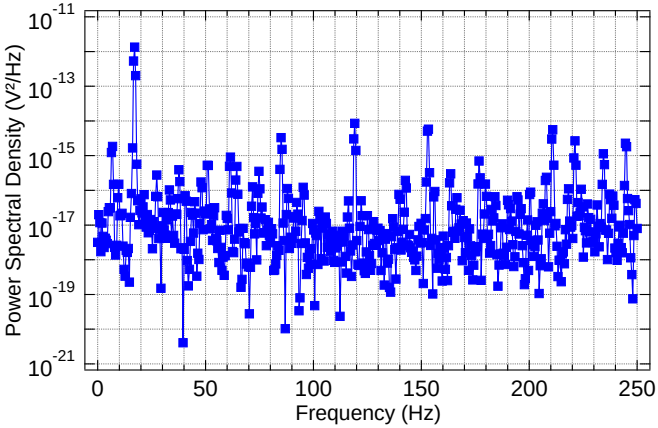

Figure 2.21: The power spectral density of a sinusoidal signal (1 µV amplitude, 17.1 Hz frequency) after applying Hanning window and with consideration of quantization noise of the A/D converter.

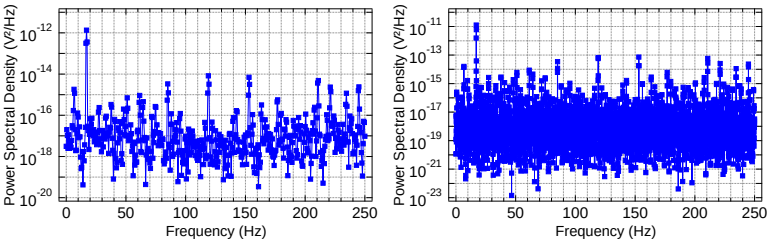

(a) N=1000 (b) N=10000

Figure 2.22: Calculated power spectral density for a sinusoidal signal regarding to equation 2.24, with different number of samples. The amount of white noise remains almost the same but the peak is higher for larger N.

$$LS = \sqrt{PS}. \tag{2.26}$$

Figure 2.23 shows the linear spectral density of the example digital signal.

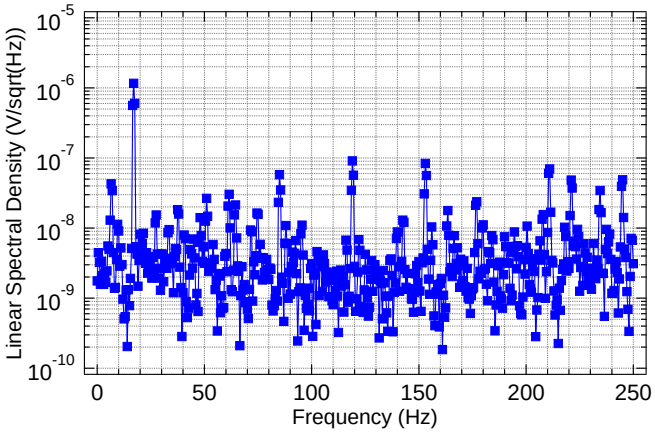

Figure 2.23: The linear spectral density of a sinusoidal signal (1 µV amplitude, 17.1 Hz frequency) after applying Hanning window and with consideration of quantization noise of the A/D converter.

2.4.6 Averaging

The resulting signal from equations 2.23 or 2.24 may appear noisier than it really is. The reason is that for a stochastic signal in each frequency bin, the standard deviation of the spectrum estimate is equal to the estimate itself. Increasing the length of the N, reduces the width of the frequency bin without improving the variance, therefore, does not help with the situation. The remedy in this case is averaging. The average of M estimates, reduces the standard resolution by a factor of $1/\sqrt{M}$.
Figure 2.24 shows a stream of window functions that can split a continuous data stream into several non-overlapping segments of length N. As it can be seen in the figure 2.24, applying this window to the data stream causes loss of a significant portion of the data due to the fact that the window function is very small or zero near its boundaries. The solution is using a stream of windows that has overlaps as shown in figure 2.25. For Hanning window this overlap is 50%. To avoid the complications regarding phase differences of the divided time signal, the averaging takes place on power spectrum or power spectral density.[83, 86]
The averaged power spectral density of the example signal of section 2.4.4 is shown in figure 2.26. The noise level after averaging is reduced considerably in comparison to figure 2.21. The difference between averaging with and without overlap is not significant in this special example.

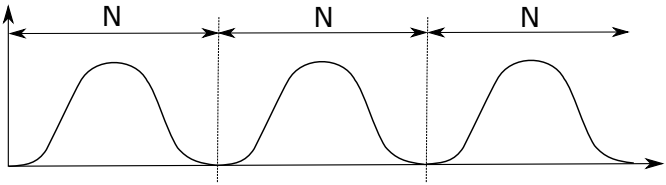

Figure 2.24: Segmenting window stream without overlap.

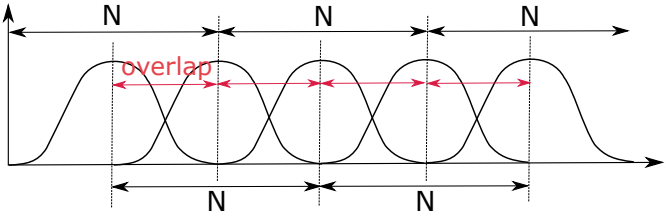

Figure 2.25: Segmenting window stream with overlap.

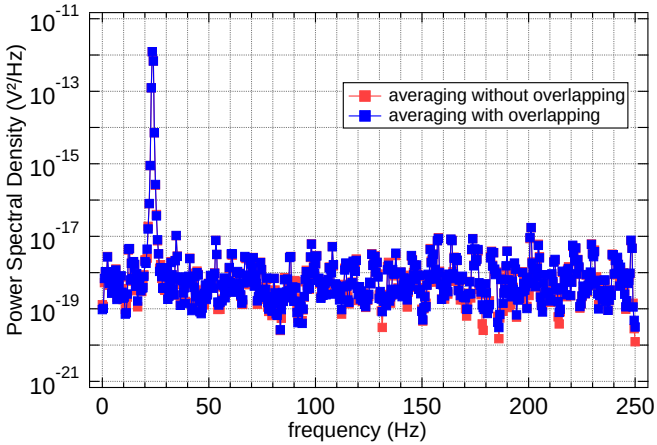

Figure 2.26: Power spectral density of the example signal after averaging.

3 Method and implementations

In this chapter, the developments done during this work are presented. These developments consist of: a noise measurement setup, textile capacitive electrodes, and a textile capacitive EEG hat.

3.1 Noise measurement setup

The noise measurement of capacitive electrodes is a very demanding process. The complication is mainly due to the fact that the interesting region of measurements lies at low frequencies. In this situation, any external disturbances in the low frequency ranges like building vibrations, power-line noise, noise on the protective earth connection, and – depending on the form and thickness of the shielding box – sound in the environment, can make the noise measurement of the capacitive electrodes impossible. The mechanical vibrations can cause a slight distance change between two sides of the input capacitor, which consequently alters the corresponding capacity. This capacity alteration contributes to the voltage noise spectra, as is shown in figure 3.1. In this figure, one measurement (shown in red) is recorded on the fourth floor of a building and inside a cubic shielding box, with thin aluminum walls (3 mm), and the other measurement (shown in blue) is recorded in the basement and in the implemented measuring setup, described below. The effect of mechanical vibrations can be seen on the red curve in the frequency range of 1 Hz to 100 Hz.

To prevent external mechanical and electrical disturbances, the phantom capacitive electrode is placed inside a heavy, thick wall (1 cm) aluminum cylindrical shielding container. The thick wall and cylindrical form of the container reduce the penetration and resonance of the acoustic signals inside the shielding. The aluminum material of the container prevents the coupling of electrical interferences. To reduce the other mechanical vibrations, the shielding container is placed on two wooden plates, which have four rubber balls in between them as dampers. The influence of the

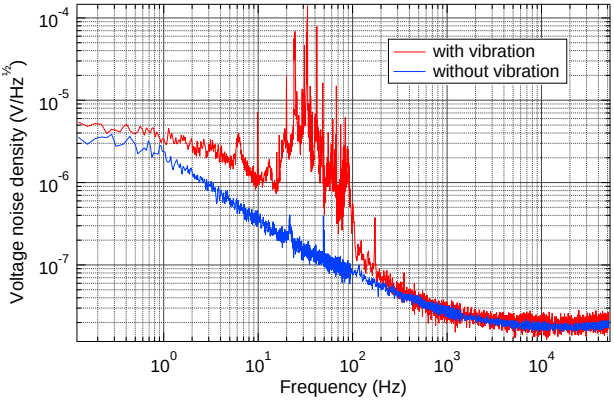

Figure 3.1: Measured influence of environmental vibrations on the voltage noise. The blue curve is the noise measurement of the capacitive electrode in the introduced measurement setup in the basement. The measurement done on the fourth floor and inside a thin, cubic shielding box is shown in red. [43]

usage of different dampers on the spectrum is illustrated in figure 3.2.

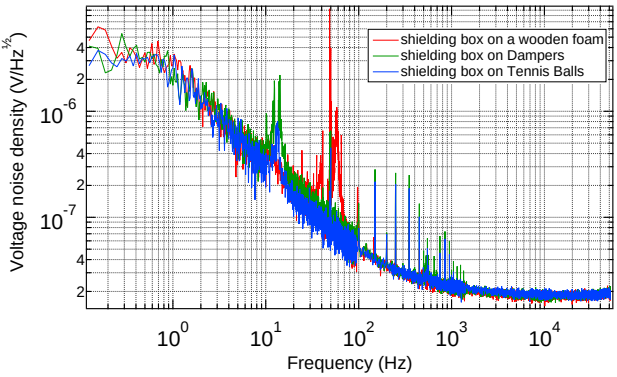

Figure 3.2: The influence of dampers on the measured spectra. It shows measurements: Without dampers on wooden foam plate, with rubber dampers, and with tennis balls as dampers.

To eliminate the protective earth connection disturbances, the ground of the measurement setup is provided by batteries. These batteries supply

electrical energy to the electrodes. The power supply of the spectrum analyzer is also decoupled from the power-line by an isolating transformer. In this way, the protective earth connection noise cannot couple into the measurements. The full measurement setup is shown in figure 3.3.

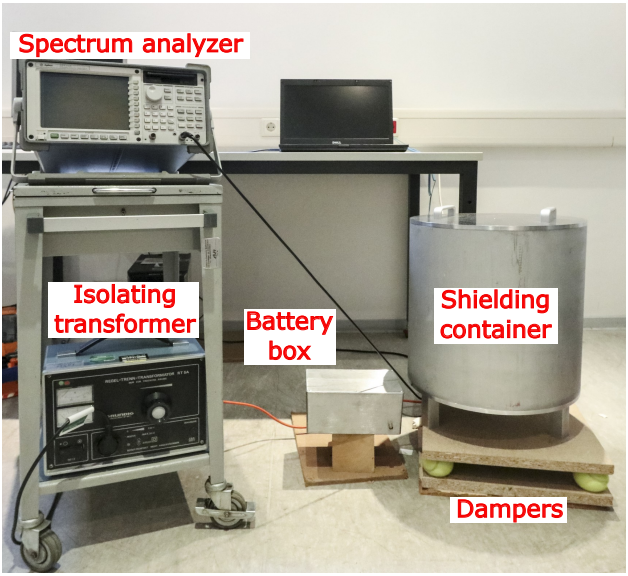

Figure 3.3: View of the measurement setup. The electrode is placed inside the shielding container and is connected to the spectrum analyzer via a coaxial cable. A portable computer is used for data acquisition and analysis.

The electrodes are supplied with a voltage of $\pm 5\,\mathrm{V}$ by the electronic board shown in figure 3.4. LM317TS and LM337TS are used as voltage regulator chip for positive and negative 5 V respectively. The PCB also contains an amplification factor of 49.8 for the output signal of the electrode. Without this amplification, the noise of the electrode may lie beneath the intrinsic noise of the spectrum analyzer. Figure 3.5 shows the intrinsic noise level of the Agilent 35670A spectrum analyzer for different input ranges. The power supply board is located at the bottom of the shielding container (see figure 3.6). The resulting spectra should then be divided by this amplification factor to obtain the actual noise level of the measured electrode only.
The measurements were performed by using a phantom electrode with ground potential at a defined distance (0.15 mm) to the capacitive electrode. A sheet of paper was installed between this phantom and the electrode plate as an insulator in these measurements. The capacitive

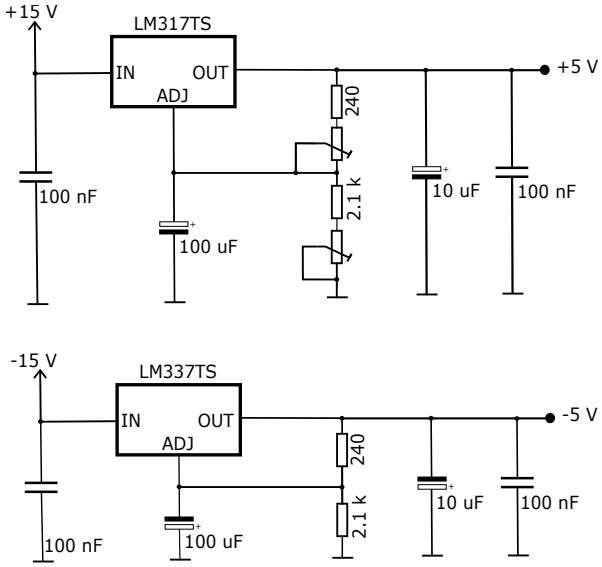

Figure 3.4: Circuit diagram of the power supply electric board.

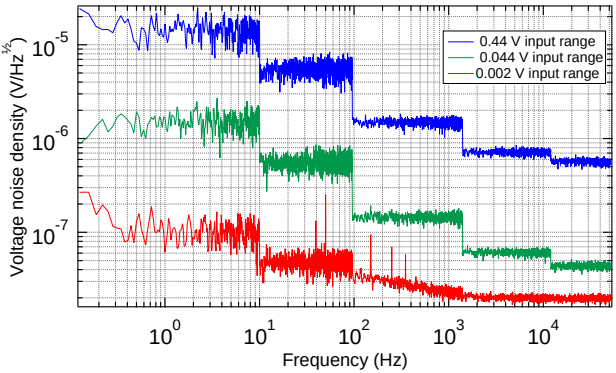

Figure 3.5: Intrinsic noise level of the spectrum analyzer for different input ranges.

electrode was placed inside the shielding container during the measurements. The noise voltage spectra were recorded with the Agilent 35670A spectrum analyzer. The spectrum analyzer was turned on at least one hour before the measurements to warm up. For each measurement, several spectra of adjacent spectral ranges are joined to obtain one single

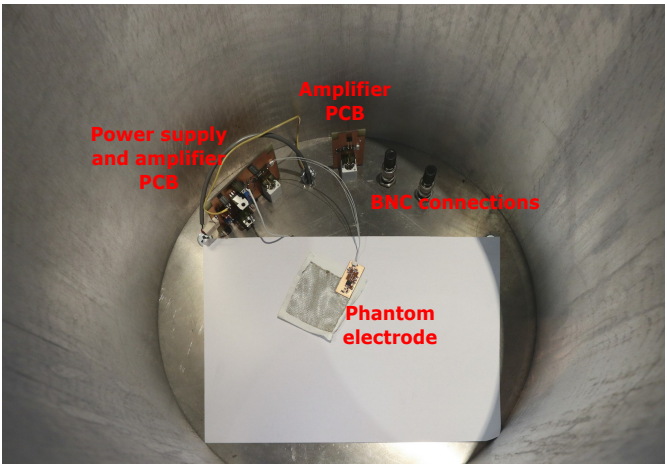

Figure 3.6: Inside view of the shielding container. Illustrating the power supply PCB, connectors, a paper sheet as an insulator, and the phantom electrode at the bottom of the container.

spectrum with a maximum spectral resolution.

3.2 Textile capacitive electrodes

The implemented textile capacitive electrodes in this work, use silver plated nylon fabric named *Shieldex Balingen* from *Statex Produktions and Vertriebs GmbH* [88] as a electrode surface and guard. This fabric is woven from 20 µm thick, silver coated, nylon threads, shown in figure 3.7. The same fabric is used for the shielding of the whole structure of the textile capacitive hat. This fabric cannot be soldered and should be pasted to the PCB with conductive paste.

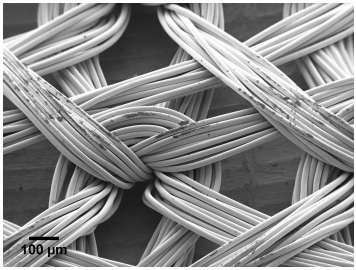

(a) Woven conductive fabric.

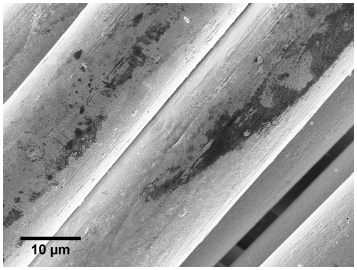

(b) Conductive threads.

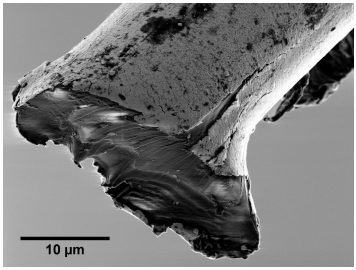

(c) A cut of conductive thread that shows the insulating material inside and the coating of conductive material on top.

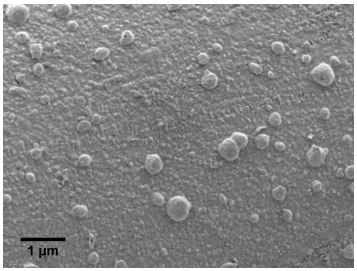

(d) Silver coating on the threads.

Figure 3.7: Scanning electron microscope (SEM) images of the used conductive fabric.

The edges of the conducive fabric are cut by burning the edges with a soldering iron to eliminate distribution of the small conductive threads over the electrical circuits and prevent shortcuts. This occurs when the fabric is simply cut with scissors. This fabric is hard to handle especially when pasting on a very small surface is required. In capacitive electrodes, two layers of this fabric are needed for the surface and guard layer. Isolation of these two layers from each other on the PCB surface is very challenging. To solve this problem, the electrode is made from two thin, 0.75 mm thick, PCBs, which are sticked together from the back. The

conductive fabric for the guard layer is connected from between these two PCBs to the electrode and the conductive fabric for the surface of the electrode is connected to the back of the electrode. This method prohibits the possibility of any connection between the surface of the electrode and guard at their attaching points to the electrode's PCB. Furthermore, a layer of polyurethane fabric is used as an insulator in between the surface of the electrode and guard layer.

A picture of the, in this work developed, textile capacitive electrode and a rigid PCB-based electrode with their dimensions, is depicted in figure 3.8.

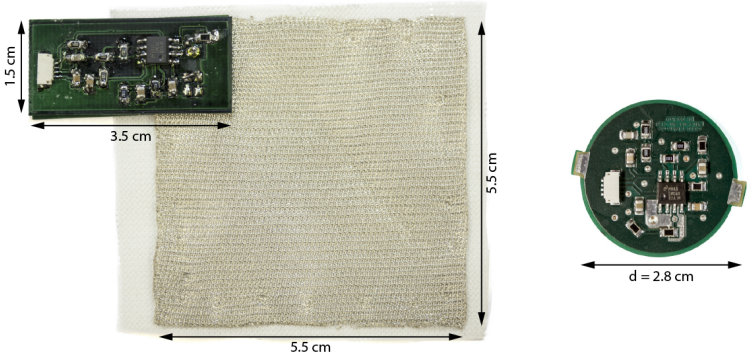

Figure 3.8: Photograph of non-contact capacitive electrodes. On the left side, the textile capacitive electrode and on the right, the rigid PCB-based capacitive electrode are shown.

The measured transfer functions of the electrodes with three different surface areas are depicted in figure 3.9. From that, we obtain cutoff frequencies of each case by reading the frequency at -3 dB attenuation. These measurements are done with the spectrum analyzer (Agilent 35670A). The input to the electrode is connected to the source output of the spectrum analyzer, which provides a swept sine signal in the frequency range of 62.5 mHz to 51.2 kHz. The output of the electrode is then read with the same spectrum analyzer.
The corresponding capacitances for each of the surface areas can be calculated by inserting these cutoff frequencies f_c into equation 3.1 and considering the bias resistor to have the value of 1 GΩ (see TABLE 3.1). The small deviation from expected 0 dB at higher frequencies shows some reduction due to the voltage divider between C_e and C_{sum}.

$$f_c = \frac{1}{2\pi \cdot R_{in} \cdot C_e} \tag{3.1}$$

Table 3.1: Corresponding cutoff frequency f_c and capacity C_e for different areas of the conductive fabric by considering the input resistor R_{bias} to be 1 GΩ.

Surface area (cm^2)	f_c (Hz)	C_e (pF)
64	0.85	185.0
32	1.43	111.3
16	2.50	63.6

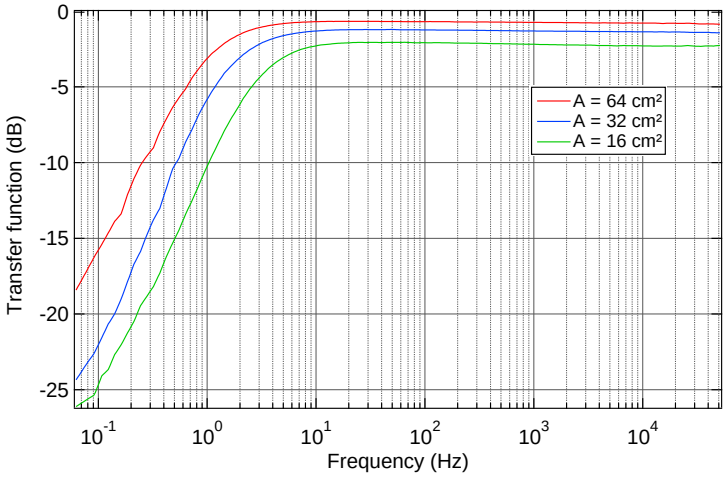

Figure 3.9: Measured transfer function for different areas A of the conductive fabric surfaces.

3.3 Textile capacitive EEG hat

Although, the introduced EEG helmet systems in section 2.2.2, made the EEG measurements effortless and time efficient, the heavy weight and rigid format of these helmets, impose unbearable pressure on the subject's head. This disadvantage causes the mentioned capacitive helmets to be unsuitable for long-term measurements.
The textile capacitive hat, on the other hand, is light and stretchable. It fits to the form of the skull and imposes minimal pressure on the head during EEG measurements. Therefore, it is suitable for very long-term measurements. More importantly, this hat is applicable for sleep disorder studies, since it is comfortably wearable during sleep.
Furthermore, a capacitive EEG hat uses flexible capacitive electrodes explained in section 3.2 with textile surface shown in figure 3.8. Besides being comfortable to wear, these electrodes have a larger input capacity and lower noise (see section 4.1.1).
The electrodes and electronics of the EEG hat are easily detachable and the fabric parts can be washed.

3.3.1 Textile capacitive electrodes of the cEEG hat

The textile surface area of each electrode is chosen to be $32\,\mathrm{cm}^2$, which corresponds to 111 pF capacitance at the input (see table 3.1). The bias resistor is chosen to be $10\,\mathrm{G}\Omega$. Therefore, the cutoff frequency of these electrodes is at 0.143 Hz.
On the textile capacitive electrodes, in addition to the high-pass and low-pass filters at 200 mHz and 159 kHz respectively, there is an amplification by a factor of 10. This extra amplification reduces the effect of coupling noises through the wires in between the electrodes and the electronics [89]. The amplification on the electrode circuit should be moderate because otherwise it may drive the following stages to saturation. A complete configuration of the textile capacitive electrode circuit diagram with emphasis on the amplification and filters is shown in figure 3.10.

3.3.2 Electrode configuration of the cEEG hat

The textile capacitive EEG hat includes eight textile capacitive electrodes. The positioning of the electrodes on the hat is illustrated in figure 3.11. One of these electrodes, which is placed at the front part of the hat, is the reference electrode. Therefore, this hat provides seven measurement channels. The electrodes are placed inside pockets sewed on top of the hat. The implemented EEG hat without final shielding is depicted in figure 3.12.

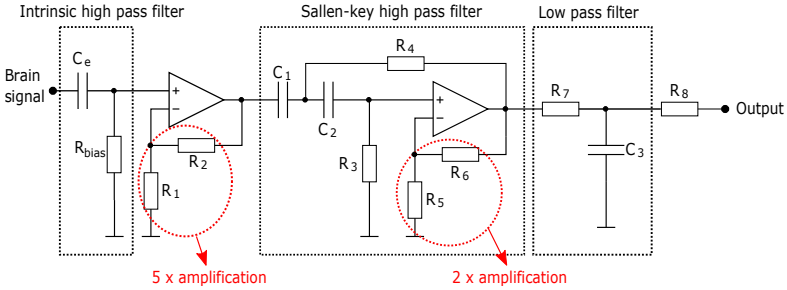

Figure 3.10: A complete equivalent circuit diagram of the textile capacitive electrode configuration. The cutoff frequency of the intrinsic high-pass filter is 0.143 Hz, for the Sallen-key high-pass filter 159 kHz and for the low-pass filter 200 mHz. The circuit also provides an amplification by a factor of 10.

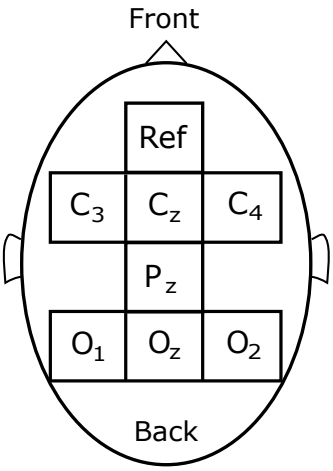

Figure 3.11: Electrode placement on the EEG hat. Electrodes: O_1, C_z, C_3, C_4, O_z, O_2, and P_z represent channels 1 to 7 of the electronics respectively. (Ref) denotes the reference electrode.

3.3.3 Implemented measuring electronics

The additional electronics of the system, such as the second stage amplifiers, A/D converters, and microcontroller, are placed inside a box on top of the hat. This box is 3D printed from electrically conductive polylactic acid (PLA) filament [90] to avoid electrostatic charging.
The power supply PCB and the battery are not integrated on top of the hat and are connected via cable to the electronics to eliminate extra weight of them from the hat.
The electronic circuits of this capacitive EEG hat are similar to that of the wireless capacitive EEG helmet systems [48, 49]. The outputs of the electrodes are compared with the output of the reference electrode by an

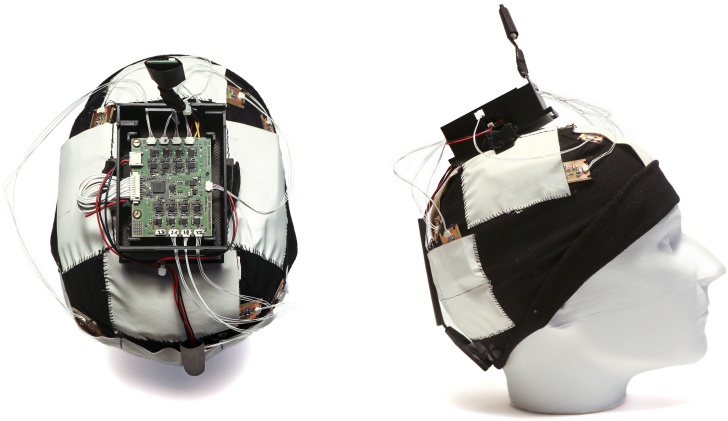

(a) Top view.

(b) Side view.

Figure 3.12: Picture of the newly implemented cEEG hat. The box on top of the hat contains the second stage amplifiers, A/D converter, and microcontroller. The white pockets contain the textile capacitive electrodes.

instrumentation amplifier stage. Here, *INA333* from *Texas Instruments*, is used as an instrumentation amplifier. This stage also contains an amplification by a factor of 100 and an anti-aliasing filter with a cutoff frequency of 69 Hz. Then, the resulting signals are digitized with *ADC ADS1258* from *Texas Instruments*. This can operate 16 channels in single-ended mode, has a resolution of 24 bits and a data rate in auto-scan mode of 23.7 kS/s. This A/D converter requires a precise voltage of 4.096 V as a reference for the quantization of the input signals. It is provided by the *ADR444B* voltage reference chip from *Analog Devices*.
The output data from the A/D converter is received by a microcontroller via serial peripheral interface (SPI). The used microcontroller is *ATXMEGA256A3* from *Atmel*. The microcontroller is clocked via an external 16 MHz quartz with $\pm 10 ppm$ accuracy, which also serves as a clock for the A/D converter. The software of the microcontroller reads the channels sequentially from the A/D converter and sends them via USART (Universal Synchronous/Asynchronous Receiver Transmitter) to the bluetooth module.
The bluetooth module is type *WT12* from *Bluegiga*. It sends the data in 24 bit long two's complement format to the computer's virtual serial port with 921.6 kbit/s (baud rate: 921600) subsequently. With each data packet, the bluetooth module sends 45 bytes to the computer. The first four bytes are filled with zeros for synchronization. Then, 39 bytes follow corresponding to 13 channels. Since the EEG hat is using 7 channels, the remaining channels are filled with zeros. The last two bytes are again zero.

After receiving the data from the bluetooth module and converting the two's complement, the ratiometric value of the A/D converter according to *ADC ADS1258* data sheet, should be calculated and the amplification factor of 1000 (factor 10 by the electrode and factor 100 by the main electronics) should be divided from the data.

The power supply circuit provides 5 V for the instrumentation amplifier and A/D board, 3.3 V for the digital part of the measuring system like microcontroller and bluetooth module, and ±2.5 V as supply for the electrodes. It uses a 7.4 V lithium-ion battery, type *BP-511*, with a capacity of 1300 mA h. To provide 5 V, the linear regulator *LT1763CS8-5* from *Linear Technology* is used. A step-down switching regulator of a type *LTC1707* from *Linear Technology*, reduces the produced 5 V to 3.3 V. The ±2.5 V is provided from the 5 V output with the use of a virtual ground. In addition, a low-pass filter and a clamping circuit are included at the end to reduce high frequency disturbances and possible spikes. [48, 49]

3.3.4 Shielding of the cEEG hat

The completed capacitive EEG hat includes a shielding that covers the entire measuring system placed on the hat, except for the bluetooth module. This is another advantage of our cEEG hat in comparison with former EEG helmets which do not have shielding except for the electrodes. The same conductive fabric as for the construction of the textile capacitive electrodes is used for the shielding. The fabric is sewed to a stretchable, cotton hat, which acts as an insulator between the shielding and electrical circuits. All the used insulating materials in construction of the EEG hat, are not electrostatically chargeable. For instance, any plastic or 3D printed material with non-conductive filament, is not suitable since it imposes disturbances and may saturate the amplifiers. The shielding is removable and is not sewed or permanently affixed to the cEEG hat. Figure 3.13 shows the final version of the cEEG hat including the shielding.

(a) Top view of the cEEG hat with shielding.

(b) Side view of the cEEG hat with shielding.

Figure 3.13: Picture of the completed cEEG hat including the shielding layer. For the shielding the same conductive fabric as for the electrode surface is used.

3.3.5 Sleeping with cEEG hat

For the study of some sleep disorders, EEG measurements have to take place during sleep. These measurements should occur in a laboratory under the supervision of professionals. This procedure can be very uncomfortable for many patients. On the other hand, the developed cEEG hat can measure the brain signals without any prior preparations. They use textile capacitive electrodes in a cotton hat that makes the observation of brain activities during sleep possible. The procedure of EEG measurement in this way does not need any supervision and can take place at home.
In implementing the cEEG hat, all the electrical circuits except for the electrodes are placed inside a box, which is located on top of the hat. In this way, they are not imposing inconvenience during sleep as is shown in figure 3.14.

Figure 3.14: Demonstration of the possibility of sleeping with the cEEG hat. The implemented textile capacitive electrodes impose no pressure on the head and the measuring electronics are located in a box on top of the head, which does not cause inconvenience.

4 Results and discussions

In this chapter, the results of different measurements of single electrodes and the cEEG hat are presented and discussed. In section 4.1, the development of a comprehensive noise model for capacitive and textile capacitive electrodes is introduced. It is followed by the measurement results from the cEEG hat in section 4.2.

4.1 Noise model for capacitive electrodes

The noise sources of the electrodes should be investigated in order to improve the noise characterization of the capacitive electrodes, as has been done for the galvanically coupled electrodes [91, 92]. Despite work that has been done in this area [93, 94], capacitive electrodes lacked a comprehensive noise model that fits closely to the noise measurements of these electrodes while offering anticipations of the behavior of their noise characteristics in accordance with possible changes. In this section, the noise sources of the electrode, and their influence on the resulting noise spectrum are illustrated. Furthermore, a noise model to fit closely to the measured noise spectra of the capacitive electrodes is presented.

4.1.1 Noise sources of capacitive electrodes

To evaluate the noise characteristics of the capacitive electrodes, first the noise sources of the circuit should be considered. By considering the equivalent circuit diagram of the capacitive electrode illustrated in figure 2.7, the corresponding noise sources of the circuit elements are added resulting in noise equivalent circuit depicted in figure 4.1. [43]
For the experimental determination of the noise properties, the capacitive electrode is measured against a ground plane to exclude external noise sources and control its capacitance reliably. Here, the Nyquist noise sources of the parasitic conductance $1/R_{\mathrm{e}}$, (S_{VRe}), and the bias resistor

R_{bias}, (S_{VRbias}) are added. The capacitances of C_{sh} and C_{OA} are connected in parallel $C_{\mathrm{sum}} = C_{\mathrm{sh}} + C_{\mathrm{OA}}$. The input voltage noise source V_{OA} and the input current noise source I_{OA} of the impedance converter have to be additionally taken into account.

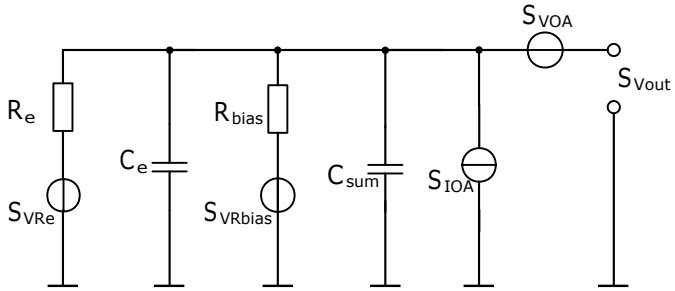

Figure 4.1: Equivalent noise circuit of capacitive electrode, by considering the thermal noise of the resistors, and the intrinsic noise of the amplifier. [43]

The following voltage noise contributions at the output of the equivalent circuit, by considering the spectral densities of Nyquist noises ($S_{\mathrm{VR_e}} = 4\,k_b T R_{\mathrm{e}}$, $S_{\mathrm{VR_{bias}}} = 4\,k_b T R_{\mathrm{bias}}$), op amp input voltage noise S_{VOA}, and op amp input current noise S_{IOA}, are:

$$\sqrt{S^O_{\mathrm{VRe}}} = \frac{R_{\mathrm{bias}}}{R_{\mathrm{bias}} + R_{\mathrm{e}} + j\omega R_{\mathrm{bias}} R_{\mathrm{e}} \left(C_{\mathrm{e}} + C_{\mathrm{sum}}\right)} \cdot \sqrt{S_{\mathrm{VRe}}} \tag{4.1}$$

$$\sqrt{S^O_{\mathrm{VRbias}}} = \frac{R_{\mathrm{e}}}{R_{\mathrm{e}} + R_{\mathrm{bias}} + j\omega R_{\mathrm{e}} R_{\mathrm{bias}} \left(C_{\mathrm{e}} + C_{\mathrm{sum}}\right)} \cdot \sqrt{S_{VR_{\mathrm{bias}}}} \tag{4.2}$$

$$\sqrt{S^O_{\mathrm{VOA}}} = \sqrt{S_{\mathrm{VOA}}} \tag{4.3}$$

$$\sqrt{S^O_{\mathrm{IOA}}} = \frac{R_{\mathrm{e}}\, R_{\mathrm{bias}}}{R_{\mathrm{e}} + R_{\mathrm{bias}} + j\omega R_{\mathrm{e}}\, R_{\mathrm{bias}} \left(C_{\mathrm{e}} + C_{\mathrm{sum}}\right)} \cdot \sqrt{S_{\mathrm{IOA}}} \tag{4.4}$$

The total voltage noise $\sqrt{S_{\mathrm{VOut}}}$ is determined from the square root of the sum of all noise contributions i.e. by adding the corresponding noise power spectral densities of the uncorrelated noise sources [76, 95]:

$$\sqrt{S_{\mathrm{VOut}}} = \sqrt{S^O_{\mathrm{VRe}} + S^O_{\mathrm{VRbias}} + S^O_{\mathrm{VOA}} + S^O_{\mathrm{IOA}}} \tag{4.5}$$

These calculations provide the corresponding voltage noise model for the individual circuit.

The dominating noise source is the bias resistor R_{bias} despite the fact that the parasitic resistance R_{e} has the higher noise spectral density. Its contribution is smaller by orders of magnitude, since it is reduced at the output terminal by the ratio $R_{\text{bias}}/R_{\text{e}}$. Therefore, the noise voltage contribution only increases by the square root of this quotient.

The simulated frequency response of the capacitive electrode and corresponding voltage noise spectrum of the equivalent circuit are shown in figure 4.2 and figure 4.3 respectively. The cutoff frequency of the high pass filter in the frequency response, is determined by the bias resistor and capacitance of the electrode relative to the body surface. The higher both values are, the lower this cutoff frequency is. The cutoff frequency also determines the frequency at which the voltage noise spectrum becomes constant towards lower frequencies. The decrease of the effective noise voltage between 1 Hz and 1 kHz frequencies is proportional to f^{-1} in voltage noise density $\sqrt{S_V}$ and f^{-2} in power noise density S_V. This results from the low-pass filter characteristics of the network in the voltage noise spectrum, with respect to the voltage noise sources of R_{bias} and R_{e}. The noise contribution decreases towards higher frequencies until reaching the white noise level of the input voltage noise of the impedance converter.

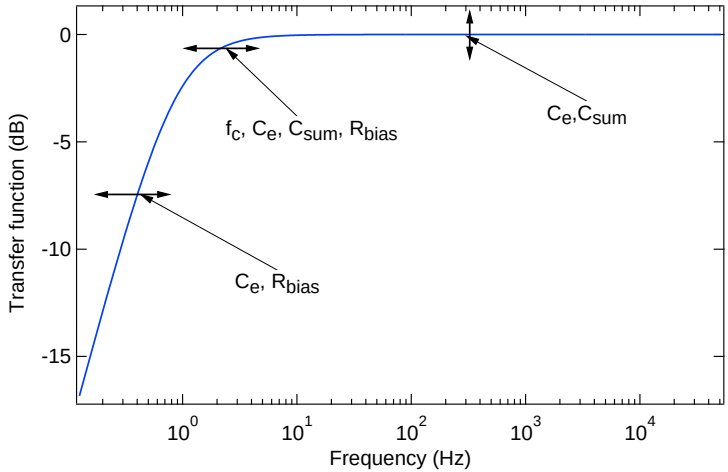

Figure 4.2: Simulated frequency response with the main influencing factors. [43]

In the following, the effect of each possible noise source is investigated with different measurements.

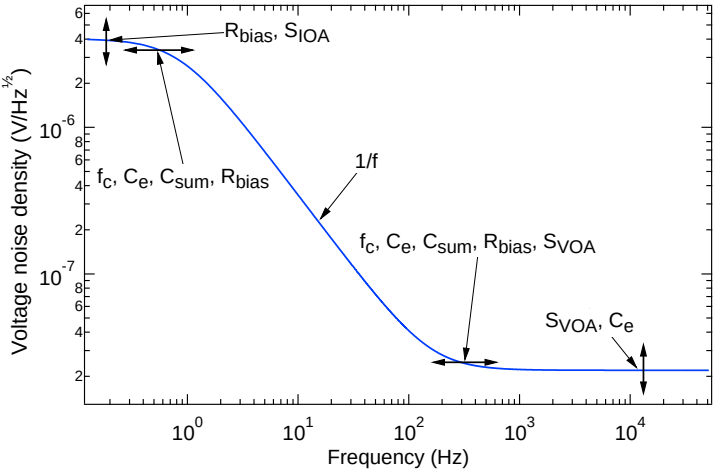

Figure 4.3: Simulated voltage noise spectrum according to equation (4.5) with the main influencing factors. [43]

Bias Resistor

One of the most important noise sources in capacitive electrodes is the bias resistor. To investigate this noise source, different discrete thick film resistors of 2.5 GΩ, 20 GΩ, and 200 GΩ, were used as the bias resistor. The measured voltage noise spectra with different values of the bias resistor R_{bias}, are depicted together with the corresponding calculated noise model in figure 4.4. The input capacity is constant for all the measurements. For impedance conversion, a *LMC6082* op amp from *Texas Instruments* is employed. Measurements with different types of op amps are presented later.

In the low frequency range (10 mHz − 1 Hz), all the measurements are in agreement with the model and show a noise, corresponding to the Nyquist noise of the bias resistor. In the mid-frequency range between 1 Hz and 1 kHz, the measured curves of voltage spectral density, show a combination of 1/f-noise from the low pass behavior of the Nyquist source and $1/\sqrt{f}$-noise, which is not included in the depicted noise model. This $1/\sqrt{f}$-noise is equal for all the applied bias resistors. At high frequencies, the three curves end to a white noise, which attributes to the op amp's voltage noise. The level of the white noise is in some measurements a factor of two higher than the value predicted by the model. It is independent of the bias resistor, but depends on the input capacitance. Therefore, the white noise in textile electrodes, which have higher capacities, is almost the same as the model prediction.

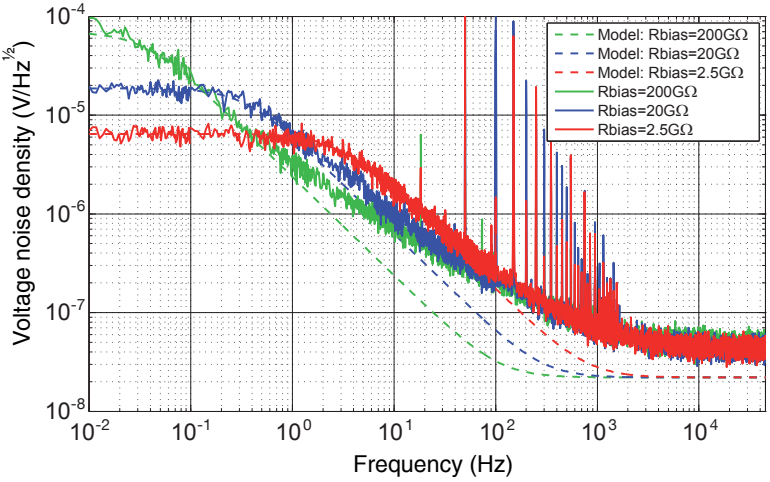

Figure 4.4: Measured voltage noise and calculated noise model for different bias resistors. In the mid-frequency range, the slope is not steep enough to be explained exclusively by 1/f-voltage noise. [43, 47]

Operational amplifiers (op amp)

From the noise model introduced in this section, we expect the influence of the impedance converter mostly on the white noise region due to the voltage noise source of the op amp, and on very low frequencies due to the current noise source of it. Though, it is necessary to determine whether the op amps have influence on the $1/\sqrt{f}$-noise. Therefore, different op amps were used in geometrically and electrically identical electrodes, to evaluate their influence on the noise spectrum especially on $1/\sqrt{f}$-noise. The corresponding voltage noise spectra of five different op amps, in this capacitive electrode setup, are depicted in figure 4.5. These selected op amps should meet the requirements of a small input bias current, to avoid any charging effect, and large input resistance.

There are two important results from these measurements to obtain. First, the $1/\sqrt{f}$-noise is nearly equal, for all the investigated types of op amps. Second, the white noise level at high frequencies, strongly depends on the specific op amp.

The LMC6082 has the lowest voltage noise density in these measurements. Therefore, it has been used as the impedance converter in the capacitive electrodes of this thesis. By connecting the op amp input to the ground potential, the measured noise spectrum is equal to the intrinsic noise of the op amp (shown in figure 4.6). At high frequencies, this spectrum matches the white noise of the electrode.

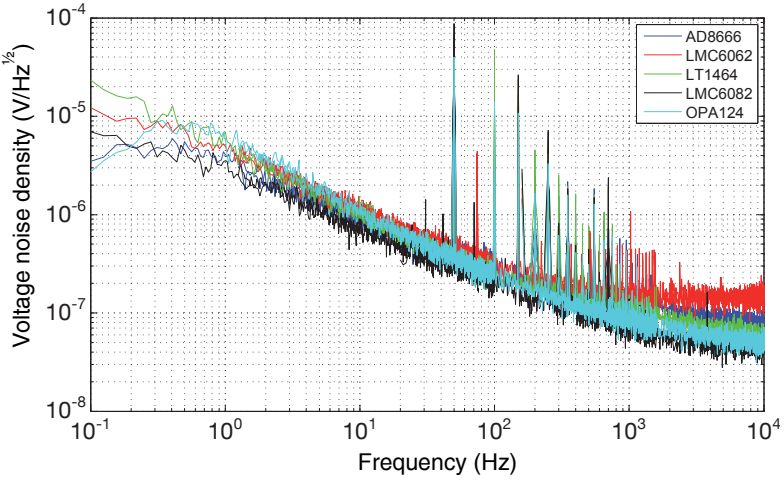

Figure 4.5: Measured voltage noise for different op amps. [43, 47]

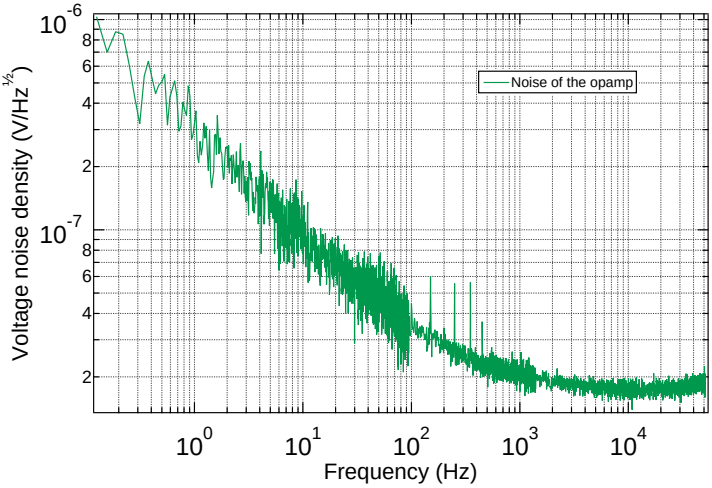

Figure 4.6: Noise spectrum of LMC6082.

Input Capacitance

To realize different input coupling capacitances, the surface area of the capacitive electrodes is changed. The resulting input capacitances were measured with a precision impedance analyzer (Agilent 4294A). When the

area of the electrode changes, it influences the coupling capacity to the shield. This has also been measured and used as a model parameter. The input capacitances range from 4 pF to 16 pF. Figure 4.7 shows the voltage noise spectra for four different input capacities and their corresponding calculated noise model.

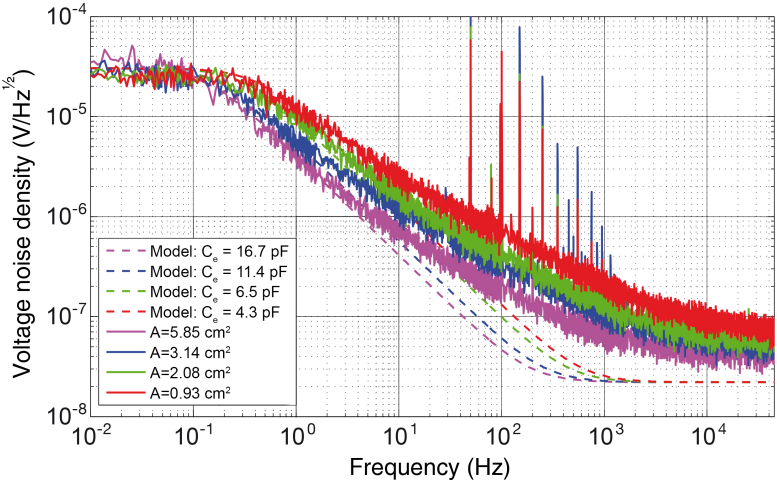

Figure 4.7: Measured voltage noise and calculated noise model for different input capacities. [43, 47]

The voltage noise density is dominated by the noise of the bias resistor in the low frequency regime ($f < 0.1\,\mathrm{Hz}$). In the mid-frequency range, a combination of 1/f-noise and $1/\sqrt{f}$-noise are present. The levels of both noise spectra are affected by the area of the capacitors. This result is especially important for including the $1/\sqrt{f}$-noise in the noise model. At frequencies above 1 kHz, the spectra show white noise behavior, which is also influenced by the input capacities. The noise level in the mid and high frequency regions decreases with an increase of coupling capacitance.

Textile Surface

Textile electrodes, which use conductive fabric as a surface of the electrodes, provide desirable advantages for biosignal measurement systems. Regarding noise characteristics, they provide larger surfaces and consequently larger input capacities for the electrodes, which shift the cutoff frequency to lower frequencies and consequently, reduce the noise at the frequency region of interest. It is also of importance to investigate their influence on the $1/\sqrt{f}$-noise.

The output noise voltages of the electrodes with different areas of the conductive fabric are shown in figure 4.8.

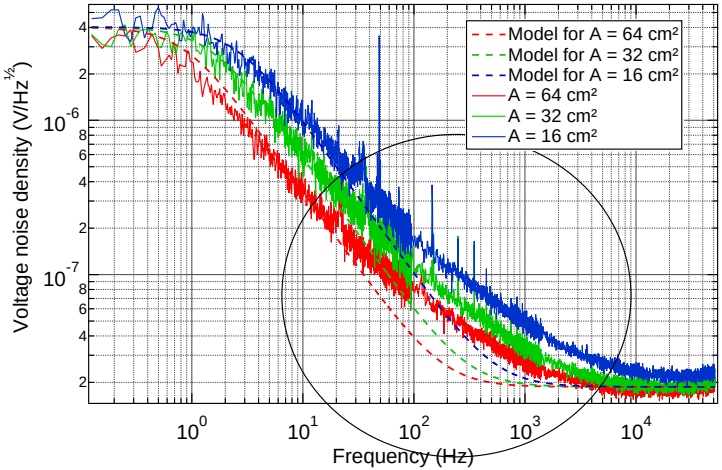

Figure 4.8: Measured voltage noise and calculated noise model for different areas of the conductive fabric surface. The deviation is marked by a circle. [43]

Increasing the bias resistor in order to increase the input resistance is not desirable, as it results in higher noise at the low frequencies. Therefore, enlarging the input capacitance by using textile surfaces, is a preferable option.
The larger input capacity of textile electrodes reduces the noise at high frequencies to the noise of the op amp (see figure 4.6 and figure 4.8). That being the case, the only region left not fitting to the noise model is in between 20 Hz and 3 kHz (see marked region in figure 4.8). The noise in this region corresponds to the $1/\sqrt{f}$-noise, which also changes with the surface area of the electrode. This change in $1/\sqrt{f}$-noise raises the question of which characteristics of the surface causes it. To determine weather the value of the input capacitor causes this influence, a measurement with a discrete ceramic capacitor with a value of 120 pF instead of the input capacity, is conducted.
Figure 4.9 shows the noise spectrum of the electrode with 120 pF discrete capacitor at the input, additionally, the noise of the electrode with the surface area of 32 cm^2 with the corresponding capacity of 111 pF, for comparison.
The discrete capacitor of 120 pF shows small additional noise at the frequency range of 40 Hz - 3 kHz, also at the frequencies less than 40 Hz the additional noise is not present. The comparison between the voltage noise spectra of the discrete capacitor and the electrode with surface area of

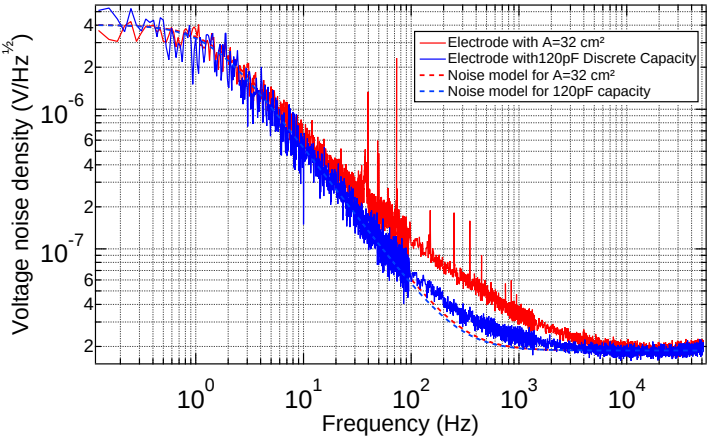

Figure 4.9: Measured voltage noise for the electrodes with fix ceramic capacity, and surface size of $32\,\mathrm{cm}^2$.

$32\,\mathrm{cm}^2$, reveals once more the influence of the capacitor on the additional $1/\sqrt{f}$-noise. Although, the corresponding noise spectrum of the electrode with the 120 pF ceramic capacitor as the input capacity in figure 4.9, shows a small deviation from the noise model. This deviation is smaller than the one of the electrode with the surface area of $32\,\mathrm{cm}^2$, though, there is not a large difference between their capacities. It shows that the additional noise is related to the surface, and dielectric of the capacitor and not to its value.

Shapes of the Electrode

One important feature of the surface of the electrode is the shape of it. The influence of different shapes and circumferences of the electrode on the noise spectrum has been investigated. Therefore, the noise characteristics of the same surface area electrodes with different circumferences have been measured. The surface areas of the electrodes in these measurements are equal to $32\,\mathrm{cm}^2$. The first electrode has a circular shape with 6.4 cm diameter, the second electrode is a square with sides of 5.6 cm, and the third one is a rectangle with 8.0 cm hight and 4.0 cm width. The circumferences respectively are: 20.2 cm, 22.4 cm, and 24.0 cm. The resulting input capacity for all these electrodes is 111.3 pF. The measurement results are shown in figure 4.10

The measurement result does not show any difference in the noise spectra for these three different cases.

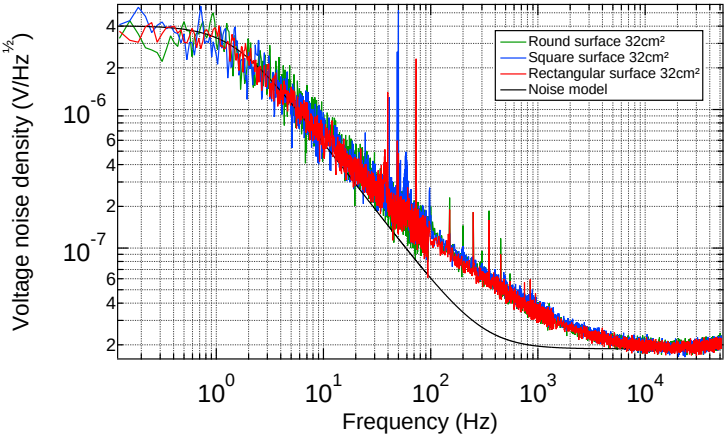

Figure 4.10: Measured voltage noise density and calculated noise model for different shapes of conductive fabric surfaces. [43]

Dielectrics of the Input Capacity

Another important feature to consider is the effect of the dielectric between the electrode surface and ground plate on the noise spectrum at the 1 Hz - 5 kHz frequency region. The noise spectra of the electrode with three different dielectrics, such as paper, PMMA resist *AR-P 642.12* from *Allresist GmbH*, and acrylic based conformal coating *Plastik 70* from *Kontakt Chemie*, are shown in figure 4.11.

The surface condition (roughness, thickness) of these dielectrics changes the average distance d of the dominating air capacity C_{air} and consequently, it changes the resulting input capacity C_{e}. The capacities resulting from different dielectrics have been measured with an impedance analyzer (Agilent 4294A) and are shown in table 4.1.

Table 4.1: Resulting capacities for different dielectrics between the electrode surface (32 cm^2) and the ground plate

Insulator	Capacity (pF)
PMMA	244.88
PLASTIK 70	201.83
Paper	111.30

The differences seen between the spectra in figure 4.11, are caused because of the capacity differences. Deviations from the noise model are present for all the measured cases.

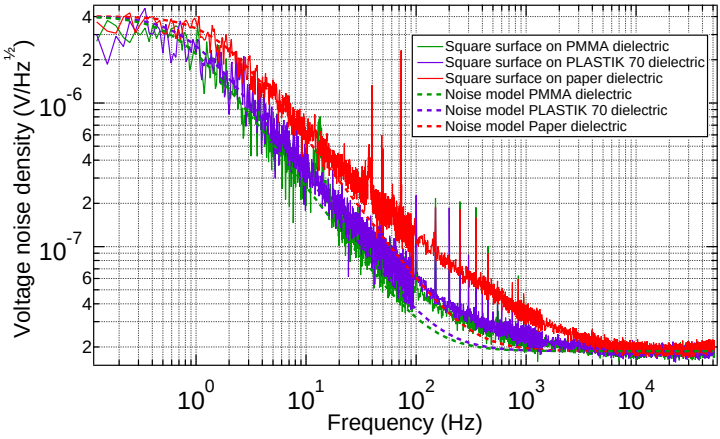

Figure 4.11: Measured voltage noise and calculated noise model for different dielectrics between the conductive fabric surface and the ground plate. [43]

4.1.2 Comprehensive noise model

The influence of all the elements of the circuit and possible noise sources are investigated to include the observed $1/\sqrt{f}$-noise into the noise model. The effect of changing the bias resistor only appears at very low frequencies of the noise spectrum. Although, it has an influence on the cutoff frequency, it has no effect on the deviations of the noise spectrum from the noise model. The operational amplifier has an influence on the white noise at very high frequencies of the noise spectra ($> 3\,\mathrm{kHz}$) but contributes less at the mid-frequency range. The op amp has a very low noise at the frequencies below 1 kHz, which does not significantly contribute on the general noise of the electrode in this region.
The input capacity of the electrode however, shows higher effect on the frequency region between 1 Hz and 5 kHz. Although some of this influence is due to the change of cutoff frequency, it also considerably changes the noise spectrum for frequencies higher than this frequency.
The deviation from the noise model between 20 Hz and 5 kHz in the measurements is independent from the value of the capacitor and it changes with the surface area, yet it is also independent from the shape and circumference of the electrode surface (compare figure 4.8 with figure 4.10). According to literature, 1/f-power noise (and by that $1/\sqrt{f}$-voltage noise) is often caused by statistical fluctuations of charges inside a material [78]. The particular situation in this case, is the extremely high input resistance in combination with the very low coupling capacitance. The charge count on this capacitor can be calculated with respect to the capacity and the voltage value.

By applying the empirical Hooge model for 1/f-power noise in solid materials [96, 97], the 1/f noise power density of the input capacitor S_{VC}, can be calculated as

$$S_{\mathrm{VC}} = \frac{k \cdot V_{\mathrm{eff}}^2}{f}. \tag{4.6}$$

With the voltage on the capacitor $\delta V = \delta Q/C$, this can be written as

$$S_{\mathrm{VC}} = k \cdot \frac{\delta Q^2}{f \cdot C^2}. \tag{4.7}$$

Where δQ is the fluctuation of charges on the capacitor and k is a constant. Extending the noise model (equation 4.5) by (equation 4.7), results in

$$\sqrt{S_{\mathrm{VFOut}}} = \sqrt{S_{\mathrm{VOut}} + S_{\mathrm{VC}}}. \tag{4.8}$$

The comprehensive fitting noise model $\sqrt{S_{\mathrm{VFOut}}}$ for three different values of the coupling capacitor is shown in figure 4.12.
The fluctuation of charges δQ have been obtained from fitting the model to the measured spectra. Constant k has been considered to be equal to 1 for simplicity, since the relative changes of δQ is of importance. For the electrode with $32\,\mathrm{cm}^2$ surface area $\delta Q/e = 600 \pm 30$ has been obtained. This number is independent of the type of the used dielectric. In the case of the noise spectrum of the electrode with 120 pF discrete ceramic capacity, the noise deviation and the value of δQ are considerably smaller than in the case of the electrode with $32\,\mathrm{cm}^2$ surface area. This number increases with the surface area; for the electrode with $64\,\mathrm{cm}^2$ surface area $\delta Q/e = 700 \pm 30$, and for the electrode with $16\,\mathrm{cm}^2$ surface area $\delta Q/e = 400 \pm 30$ have been obtained. The scaling of the fluctuation of charges with the surface area and the fact that the voltage noise is independent of the circumference (see section 4.1.1), indicates that the fluctuation of charges are homogeneously distributed across the surface and that the excess noise is not an edge effect.

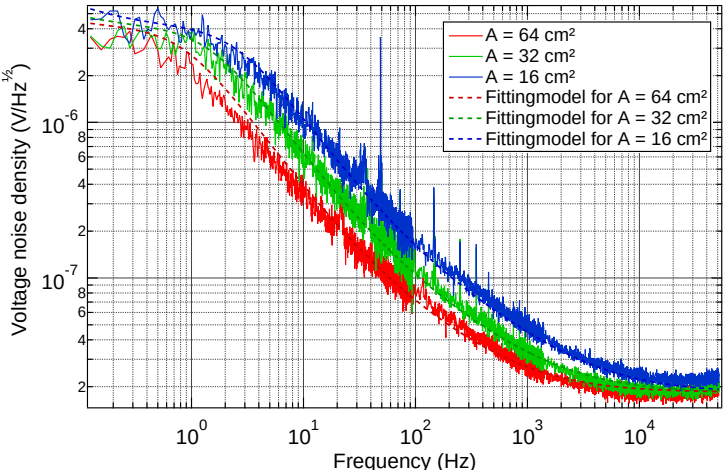

Figure 4.12: Measured voltage noises of three different electrode surface areas and corresponding fitting noise models. The fitting parameters are $\delta Q/e = 700 \pm 30$, 600 ± 30 and 400 ± 30 respectively. [43]

4.2 cEEG hat measurements

The cEEG hat introduced in section 3.3 is applicable in short and long-term EEG measurements as well as during sleep. It includes seven measuring channels, and sends the received data from these channels via bluetooth to the computer. With sampling rate of 500 S/s, this hat can measure up to a maximum frequency of 250 Hz.
The textile shielding of this hat provides an impressive electrical protection against electrically coupled disturbances.
For the calculation of linear (voltage) spectral density of the signals and averaging, the process introduced in section 2.4 is applied. In this section, noise measurements of the cEEG hat, digital signal processing, as well as alpha waves, brain waves during sleep, and SSVEP measurements, are presented.

4.2.1 Effects of averaging

To reduce the influence of arbitrary disturbing signals from the measurement, averaging must be performed. Power spectral densities of data sets are used for the calculation of the averaged signal to eliminate the problem of phase differences. Here, the process described in section 2.4.6 is used. The difference between averaging with and without overlap is shown in figure 4.13. Averaging reduces the noise, however, it also reduces the resolution and signal through windowing. To compensate for the signal loss, averaging with overlap is preferable and to counteract the reduction of resolution, measurements should be done for a longer time to obtain more data points (see equation 2.15).
The applied averaging process without overlap, divides the signal into three parts, then applies the Hanning window function on each part. Afterwards, the PSD is calculated for each part, therefore, the phase information is consequently excluded. The resulting data can be averaged afterwards.
In the process of averaging with overlap, signal is divided into three parts first. Then, two additional overlapping sets of data with a same size are constructed, which result in five sets of data. The rest of the process is the same as the averaging process without overlap.

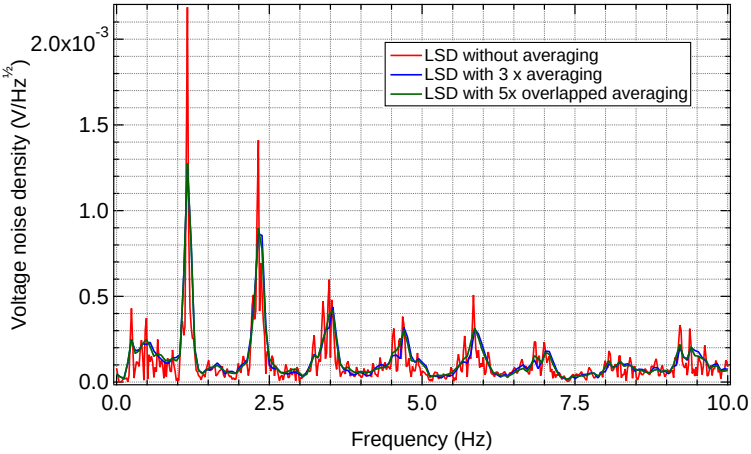

Figure 4.13: Linear/voltage spectral density of an example signal. Averaging without overlap is done three times and with overlap five times. The large peak at 1 Hz and its harmonics are related to pulse wave disturbance. Averaging decreases the noise and disturbances, also reduces the resolution.

4.2.2 Noise of the cEEG hat

The intrinsic noise level of the cEEG device is a very important factor that defines the possible level of signal that can be measured with the device. The cEEG hat by using textile capacitive electrodes, exhibits low noise characteristics. The voltage spectral density of one of the cEEG hat electrodes, is shown in figure 4.14. This measurement has been recorded for one of the electrodes separately in the noise measurement setup described in section 3.1.

The effect of the employed high-pass filter with 200 mHz cutoff frequency can be seen at very low frequencies. A slightly higher noise at around 1 Hz is observable in comparison with the results shown in figure 4.12 for the electrode with a surface area of 32 cm. This is expected, since the textile electrodes on the cEEG hat have a larger bias resistance of 10 GΩ in comparison with the measured electrodes in section 4.1, which have a 1 GΩ bias resistor. As it is described in section 4.1.1, a larger bias resistor causes higher level of noise at low frequencies.

In figure 4.15, the voltage spectral density of all the channels of the cEEG hat is shown. The cEEG hat has been measured against ground potential in this measurement. The ground potential is provided by a grounded aluminum layer that covers a phantom head, which wears the cEEG hat. The result has been averaged five times with overlapping. The

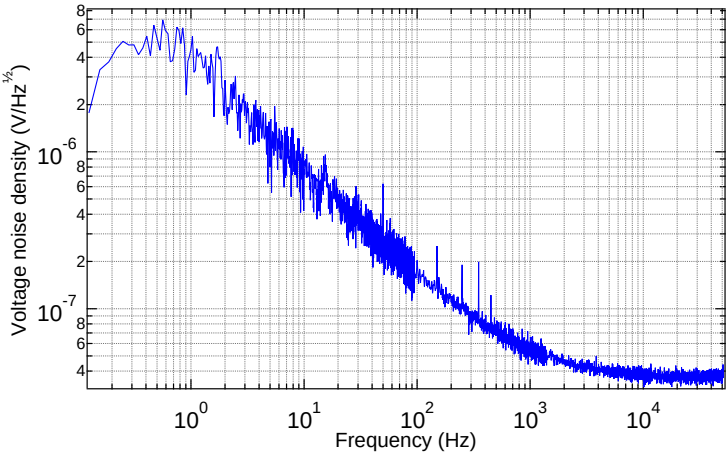

Figure 4.14: Voltage spectral density of one of the cEEG hat electrodes. The electrode has 10 GΩ bias resistor and low-pass and high-pass filters at 159 kHz and 200 mHz respectively. This measurement has been recorded from one of the cEEG hat electrodes separately in the noise measurement setup.

measurement has been recorded in a magnetic shielding chamber (Vacuumschmelze AK3b). However, some influence of German train system power line signal at 16.7 Hz can still be observed.
The voltage noise spectrum from the cEEG hat in figure 4.15 is quite similar to the voltage noise spectrum from the single electrode shown in figure 4.14. A slightly higher noise level for the cEEG hat is due to noise contribution of the other electronics of the cEEG hat.
This voltage noise spectrum of the cEEG hat also shows that signals with amplitudes higher than 10 µV can be easily measured at low frequencies, which is acceptable, since the brain waves of interest for sleep disorder measurements at lower frequencies have higher amplitudes. At frequencies higher than 20 Hz, which is the region of interest for SSVEP signals, the noise level is even lower than $1.5\,\mu V/\sqrt{Hz}$. Therefore, this EEG measuring device is definitely appropriate for SSVEP measurements and can measure signals as low as 2 µV in this frequency range.
A very important feature of the introduced cEEG hat is a fabric shielding layer that covers the cEEG hat almost entirely (except for the bluetooth module). This reduces coupling of disturbances considerably and consequently, makes the EEG measurement outside laboratories possible.
To show this effect, two noise measurements are done in a normal environment of an apartment with all lights and electrical devices switched off inside a closed room. The first noise spectrum, shown in figure 4.16, depicts all channels of the cEEG hat without shielding cover. This can be

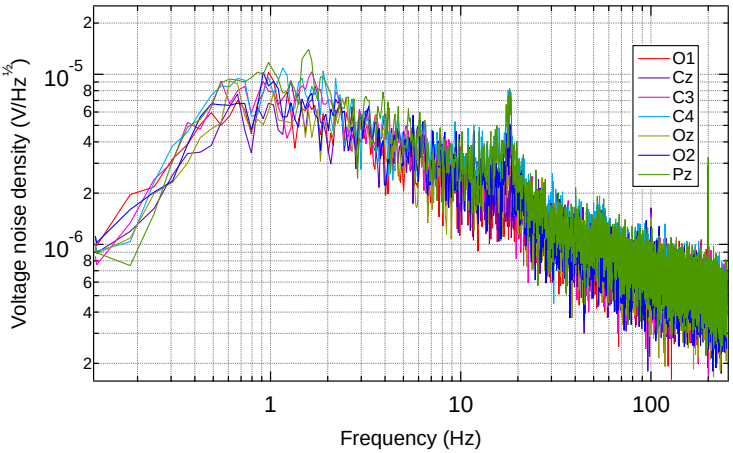

Figure 4.15: Linear spectral density of the cEEG hat with 7 channels. This measurement is done inside the electromagnetic shielding chamber. The cEEG hat has its electric shielding attached. The noise spectra of each channel are shown in different colors. The measurement is done in 49 s and has been averaged 5 times.

compared to the second spectrum, shown in figure 4.17, with the shielding layer attached. Each of these measurements has been recorded for 60 s and averaged 5 times with overlap.
Here, the impact of the shielding cover on the resulting noise spectrum is obvious. With the shielding layer, the power line signal at 50 Hz in the spectrum is considerably reduced compared to the noise spectrum for cEEG hat without a shielding. This attributes in addition to other disturbances over the spectrum. However, at frequencies lower than 1 Hz, the noise spectra are quite similar in both cases. The noise characteristics with shielding cover is almost identical as the one measured in a shielded area of the laboratory (compare figure 4.15 and figure 4.17). This prevention of extra noise and disturbances by using a shielding layer, provides the possibility of measuring with less effort and at home.

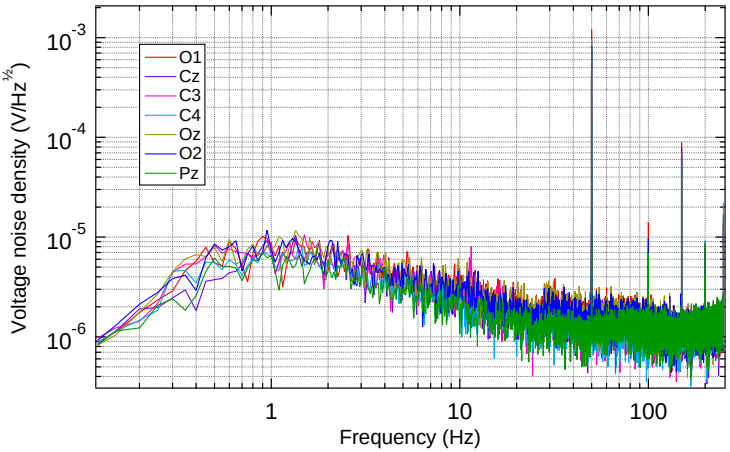

Figure 4.16: Noise spectrum of the cEEG hat without shielding in normal environment inside an apartment. The noise spectra of each channel are shown in different colors. The measurement has been recorded in 60 s and averaged 5 times.

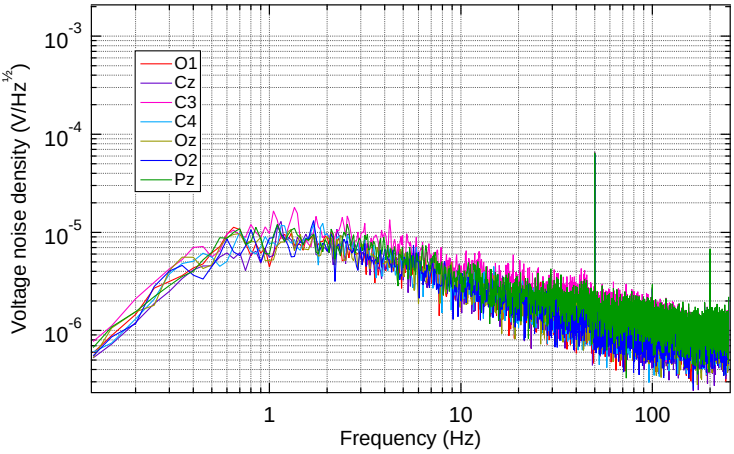

Figure 4.17: Noise spectrum of cEEG hat with electrical shielding layer in normal environment inside an apartment. The noise spectra of each channel are shown in different colors. The measurement has been recorded in 60 s and averaged 5 times.

4.2.3 Digital signal processing and reduction of disturbances

In addition to analog filters that are implemented in the electrical circuits of the cEEG hat and the electrodes, digital filtering and signal processing assists with excluding inevitable disturbances, like heartbeat, and power line signals, which may couple in small amount despite shielding.
The heart signal detected in EEG measurement is actually the pulse wave that is produced by surface blood vessels in the scalp. This pulse causes a movement and consequently distance change between the electrode surface and the head. This disturbance appears in pulse shaped format in the EEG measurements. By applying more pressure on the electrodes to the head, the effect of this movements can be reduced. This is shown in figure 4.18, where the time signal of channel O2 shows a reduction of the pulse signal by applying extra pressure by wearing a headband around the cEEG hat. The shielding layer of the cEEG hat allows the usage of different headbands and other elastic materials to apply extra pressure on the electrodes, which would be impossible to use without it due to the sensitivity of these electrodes to electrostatic charges.

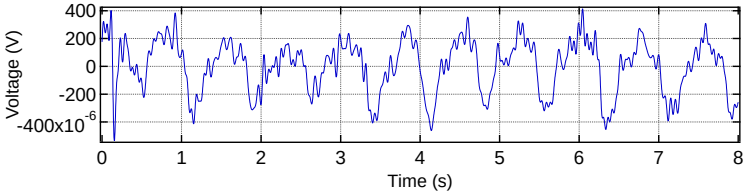

(a) Received signal from channel O2 of the cEEG hat in time domain without applied extra pressure.

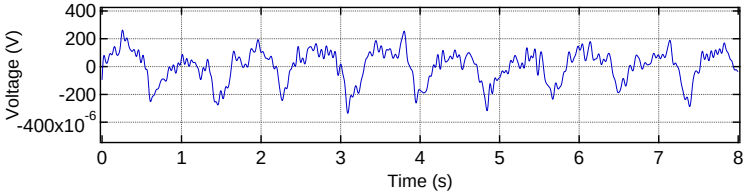

(b) Received signal from channel O2 of the cEEG hat in time domain with applied extra pressure of a headband.

Figure 4.18: The time signal of channel O2 with and without headband. After applying pressure with a headband, the apparent pulse wave is reduced.

A digital band-pass filter is used to eliminate possible drifts and high frequency coupling disturbances. The effect of the band-pass filter in time domain on a measured signal from the cEEG hat is shown in figure 4.19.

Here, a Butterworth band-pass filter is used to acquire a frequency response as flat as possible [98]. The used Butterworth filter, has cutoff frequencies of 0.2 Hz and 15 Hz with an order of 10 to achieve a sharp cutoff frequency.

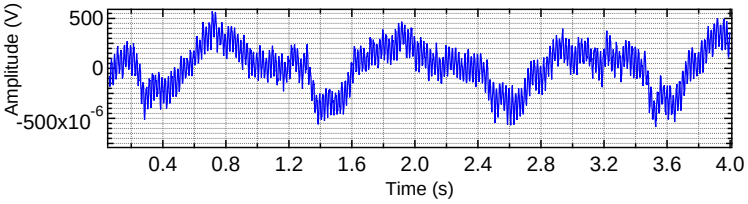

(a) Received signal from the cEEG hat in time domain. The apparent short-time oscillations result from the 50 Hz noise of the power line.

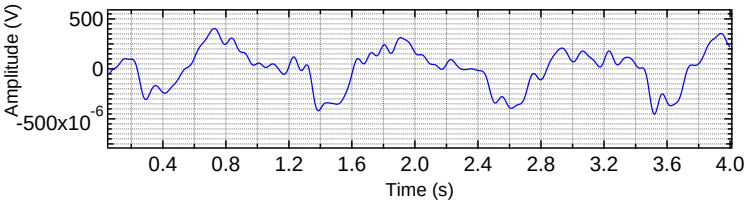

(b) Signal in time domain after filtering with a band-pass filter to eliminate high frequency interferences. The effect of the pulse wave signal with about 1 Hz is observable.

Figure 4.19: Measured time signal (a) before and (b) after filtering. After filtering, the influence of power line interference is eliminated from the signal.

Excluding heart/pulse wave signal is much more challenging. The use of a notch filter that can exclude this signal and its harmonics, is not recommendable since many interesting brain signals appear in the same frequency range. With a technique called "independent component analysis" (ICA), the pulse wave signal can be distinguished as a separate component which can then be rejected from the signal. To benefit most from this method, a parallel ECG measurement is recommendable to detect the consequent artifact of the heart beat. [99] The ECG signal supports the algorithm to calculate the heart frequency and also to estimate the exact time of the occurrence of the pulse wave in the time domain, by adding some time delay to the ECG signal. This delay is for the time that is needed for the blood to reach the head. Therefore, the algorithm can successfully detect the pulse wave component from the EEG signal. [100] To be able to use this algorithm effectively without measuring a simultaneous ECG, the EEG signal should be measured for a long time (at least two minutes) and the measured signal should be without any extra dis-

turbances like movement artifacts. Otherwise, this algorithm may not be able to detect the patterns of EEG signal components at lower frequencies appropriately. [101] For the SSVEP signal analyzes, on the other hand, the ICA method can be effectively used, when the signal is band-pass filtered on the frequency region of the stimulus frequencies in advance.
Another less elaborate and efficient approach, since the pulse wave disturbance appears on all the electrodes almost with the same intensity, is to average the output signal of some chosen electrodes that may not have interesting biological signals and subtract it from the other electrode's signal with anticipated interesting signals. The effect of this method on channel Pz is shown in figure 4.20. Here, channel C3, C4, and Cz are used to calculate an average value signal. This method can reduce the pulse signal artifact very effectively without the need of having an additional ECG signal or a longer measurement. However, a slight effect of the pulse wave remains (see figure 4.20b). This is due to the slight time differences of the exact occurrences of the pulse wave and its intensity for different electrodes.

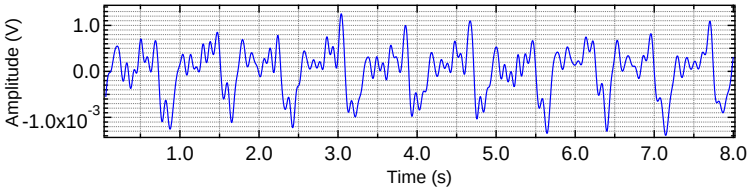

(a) Signal of channel Pz after filtering of the line noise.

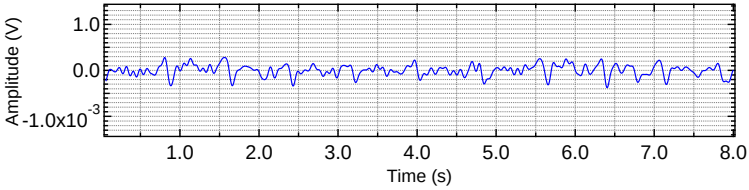

(b) Signal of channel Pz after filtering of the line noise and subtracting the average value of three other channels C3, C4, and Cz.

Figure 4.20: The effect of subtraction of the averaged signal of three electrodes from the time signal of interest. The pulse wave effect is effectively reduced from the signal in 4.20b.

Other artifacts that may be caused by body movements, should be visually detected and manually rejected from the data.

4.2.4 Alpha wave measurements

To show the applicability of the cEEG hat, some alpha wave measurements are performed. The alpha signals are common signals to be measured, which have an sufficient amplitude of some hundred microvolts. These signals are in the frequency range of 8 Hz to 13 Hz.
Alpha signal measurements with opened and closed eyes on all the channels, are shown in figure 4.21. Alpha waves normally appear with a higher amplitude when the eyes are closed and smaller when the eyes are open. These measurements have been recorded, while the shielding cover of the cEEG hat was attached. The signals are only filtered with a band-pass filter between 8 Hz and 20 Hz. Since alpha waves are located at frequencies higher than the heart beat disturbance, simple band-pass filtering suffices in most cases.

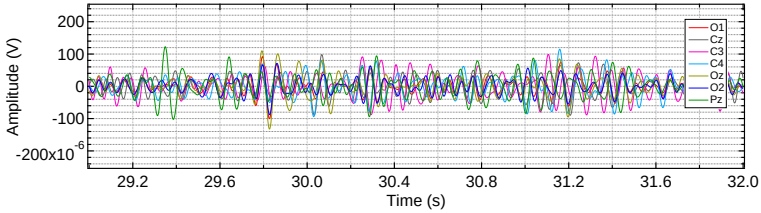

(a)

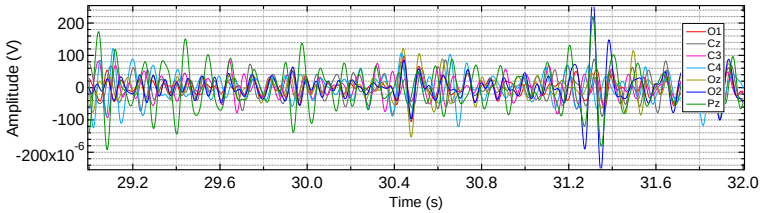

(b)

Figure 4.21: Alpha signal on all channels with (a) eyes opened and (b) eyes closed. Signals are band-pass filtered between 8 Hz and 20 Hz.

Figure 4.21 shows the dominant alpha wave with a frequency of about 11 Hz and amplitude between 20 µV and 200 µV, which has the expected characteristics.

In figure 4.21, an enhancement of alpha waves with closed eyes can be seen, especially on channel Pz. Therefore, the alpha wave measurements for channel Pz are shown separately in figure 4.22.

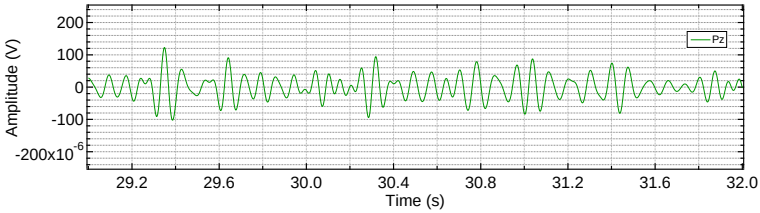

(a)

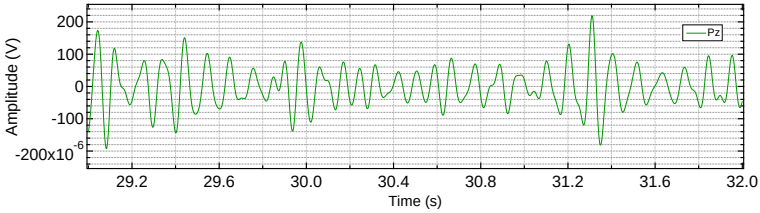

(b)

Figure 4.22: Alpha signal on channel Pz with (a) eyes opened and (b) closed. Signal is band-pass filtered between 8 Hz and 20 Hz.

4.2.5 SSVEP measurement

A very important application of the cEEG hat is in the BCI field. The precision of measurement in addition to wearing comfort of our hat, makes it a suitable device for long-term BCI measurements. The interface between brain and computer are evoked potentials. The computer produces different stimulus signals and reads the responses of the brain in form of steady state evoked potentials.
We used a visual stimulus signal in form of a blinking checkerboard on the computer monitor. The colors of the checkerboard are black and white, which are inverted with a defined frequency. Therefore, it appears as a blinking pattern. With each change of pattern, the eye produces an evoked potential, which is measurable on the back of the head above the visual cortex. The stimulus frequency that evokes signal on the head is two times the frequency of the blinking pattern on the monitor. The computer can produce different stimulus signals with different pattern frequencies, and by reading the SSVEP, distinguish the watched pattern. This simple procedure can be used in many applications in BCI field.
To provide a reliable stimulus frequency on the monitor, an application programming interface to the hardware (DirectX) is used. DirectX can bypass most layers of the Windows operating system and access the graphic card of the computer directly in real time. This allows images to be displayed on the monitor with minimal delay. [48, 102] There is just a slight phase shift depending on the rendering pattern of the monitor from

one end of the checkerboard to the other. However, if the person stares at the same spot of the checkerboard, there would be no inaccuracy in the stimulus signal.
The evoked potential is observable on the electrodes on the back of the head, though, prominently on just one of these electrodes. It is different between the individuals on which electrode the evoked potential can be seen, however, channel O1, O2, and Oz are mostly prone to it. The SSVEP responses of channel O2 to signals with five different stimulus frequencies for the same individual are presented in figure 4.23.

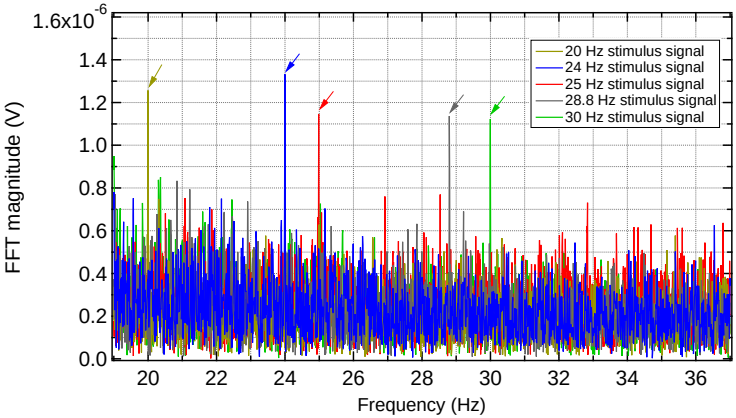

Figure 4.23: FFT response of channel O2 to different stimulus signals. Each measurement has been recorded for 90 seconds. The SSVEP responses to each stimulus frequency in the spectra are marked with arrows. The signal amplitudes are in all cases larger than 1 µV.

Different colors denote SSVEP responses to different stimulus frequencies. The SSVEP responses are approximately two to three times higher than the noise level and by that significant.

In figure 4.24, the FFT response of all the channels to a 24 Hz stimulus signal is illustrated.

In this figure, it can be seen that the evoked signal appears only on channel O2 at 24 Hz.

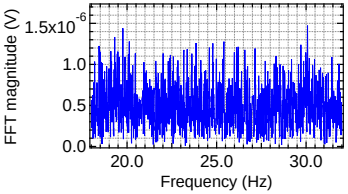

(a) FFT of the signal on channel O1

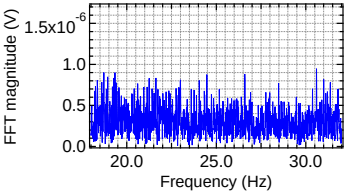

(b) FFT of the signal on channel Cz

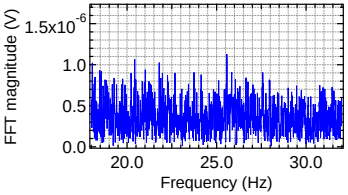

(c) FFT of the signal on channel C3

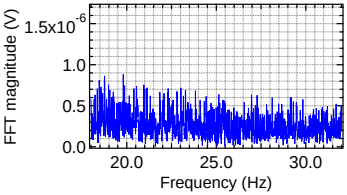

(d) FFT of the signal on channel C4

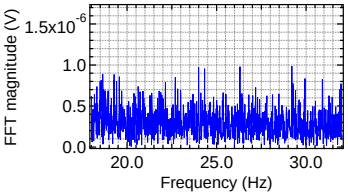

(e) FFT of the signal on channel Oz

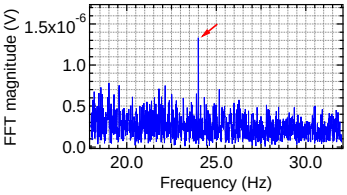

(f) FFT of the signal on channel O2

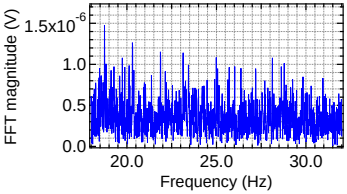

(g) FFT of the signal on channel Pz

Figure 4.24: SSVEP results on all channels with a stimulus frequency of 24 Hz. Only channel O2 exhibits the evoked state. The calculated and normalized FFT magnitude is plotted against frequency.

The use of the ICA algorithm can additionally assist with finding the SSVEP components, if disturbances are coupled into the measurements. This effect is shown in figure 4.25. The used stimulus frequency in this measurement is at 20 Hz. The evoked frequency can be seen in the FFT result of channel O2. However, the coupled disturbances are of higher amplitude. The ICA algorithm considers the signals on all the channels and finds their corresponding components separately. One of these components is the SSVEP response. To use the ICA method, the signal should be band-pass filtered to exclude high amplitude signals at lower frequencies and 50 Hz.

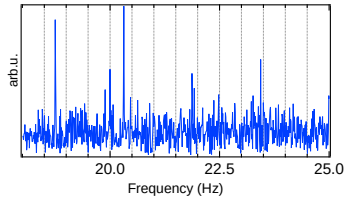

(a) FFT result from channel O2 with applied 20 Hz stimulus signal.

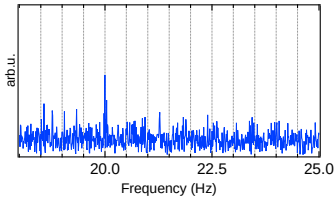

(b) FFT of one ICA component of the same channel.

Figure 4.25: FFT of (a) response of channel O2 to the 20 Hz stimulus signal, (b) of the corresponding ICA component.

4.2.6 Sleep measurements

An additional important application of the cEEG hat is EEG measurement during sleep. With the cEEG hat, sleep measurements are possible outside laboratories and in normal situation at the patient's home. Sleep measurements in this work, have been recorded on a normal bed in an apartment.
The measurements have been recorded through the night in 49 s epochs. The measured signals on channels O1, O2, Oz, and Pz at 23:46 pm and 00:18 am are shown in figures 4.26 and 4.27 respectively.

The signals are filtered with a band-pass filter between 0.2 Hz and 25 Hz to exclude drifts and high frequency disturbances. The output signal of channels C3, C4, and Cz are used for the calculation of an averaged signal, since they don't contain valuable signals for this measurement. This reference is then subtracted from channel O1, O2, Oz, and Pz signal to diminish the pulse wave disturbance.
At 23:46 pm, the test person is lying on the bed with closed eyes and in the drowsiness state in stage 1 and 2 of sleep (see figure 4.26). Here, alpha waves in the frequency range of 8 Hz to 11 Hz and theta waves in the frequency range of 4 Hz to 8 Hz are apparent as expected (see section 2.1.5). At 00:18 am, the test person is in deeper sleep (see figure 4.27). Signals with higher amplitudes and at lower frequencies are observable. This determines the appearance of delta waves, which are expected during deep sleep in stage 3 and 4.

The calculated FFT of the signals on channel O1 at 23:46 and 00:18 am are shown in figures 4.28 and 4.29 respectively.
Figures 4.28 and 4.29 show that some effect of pulse signal and its harmonics are still apparent. This indicates that with subtracting the averaged signal, the whole pulse wave would not be excluded and it will appear with lower amount in the resulting signal. It can also be seen that the heart beat has decreased from 1.2 Hz at 23:46 pm in drowsiness to 0.9 Hz at 00:18 am in deep sleep.
The level of alpha waves is slightly higher in figure 4.28 in comparison with figure 4.29. However, theta waves are clearly higher in the drowsiness state. Delta waves appear dominantly in figure 4.29 which indicate the state of deep sleep of stage 3 and 4.
The measurements during the night showed different periods of dominating alpha and theta waves or delta waves in the signals, which are following each other in some patterns. These patterns for different nights are not uniform and change from one night to the other.

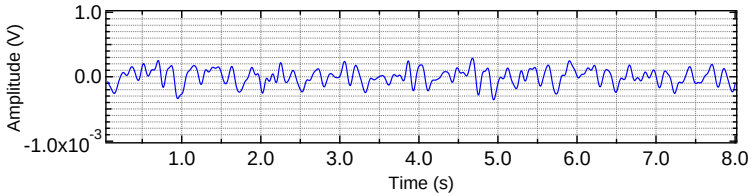

(a) Signal on channel O1 during drowsiness at 23:46 pm

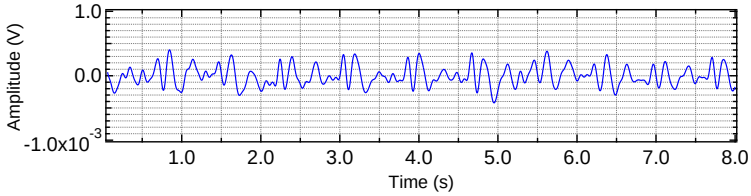

(b) Signal on channel O2 during drowsiness at 23:46 pm

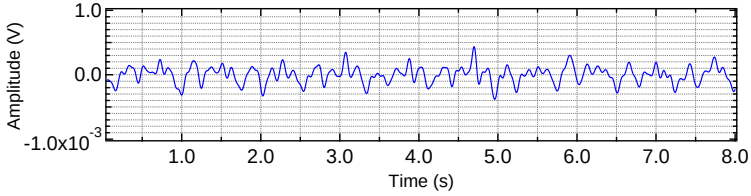

(c) Signal on channel Oz during drowsiness at 23:46 pm

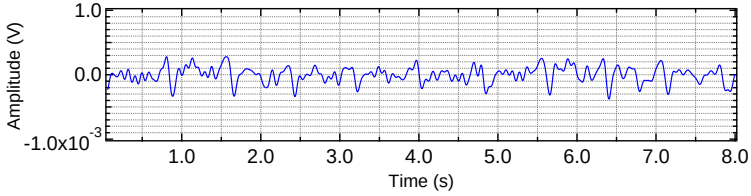

(d) Signal on channel Pz during drowsiness at 23:46 pm

Figure 4.26: Brain signals on channels O1, O2, Oz, and Pz before sleep and in a state of drowsiness at 23:46. The signals have been band-pass filtered between 0.2 Hz and 25 Hz and the averaged signal has been subtracted from them. Some waves in a frequency range of 4 Hz to 11 Hz are observable.

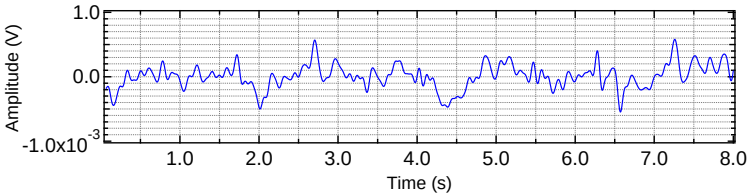

(a) Signal on channel O1 during sleep at 00:18 am

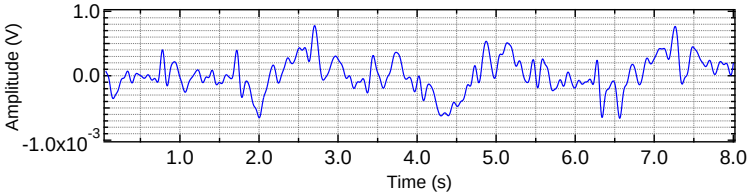

(b) Signal on channel O2 during drowsiness at 00:18 am

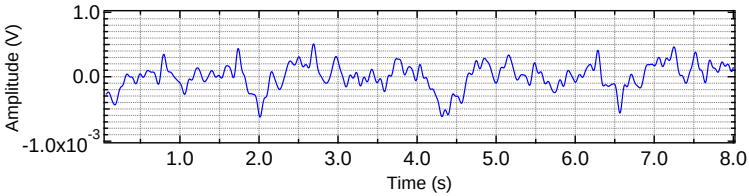

(c) Signal on channel Oz during sleep at 00:18 am

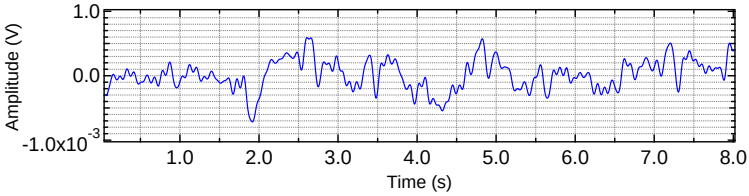

(d) Signal on channel Pz during sleep at 00:18 am

Figure 4.27: Brain signals on channels O1, O2, Oz, and Pz during deep sleep at 00:18. The signals have been band-pass filtered between 0.2 Hz and 25 Hz and the averaged signal has been subtracted from them. Dominating delta waves with higher amplitude and lower frequencies are observable in the measurements.

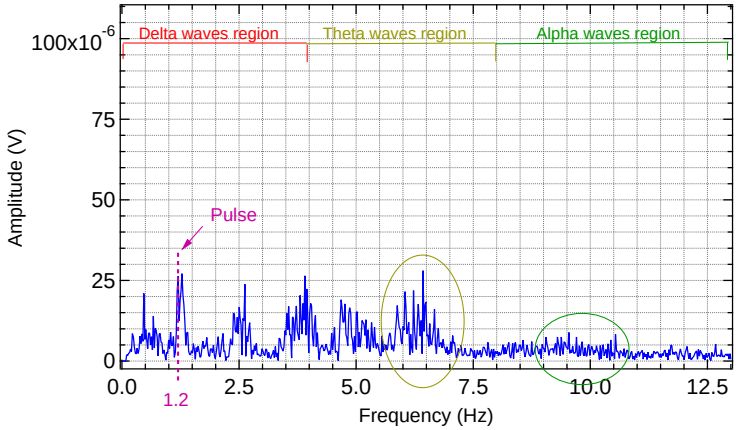

Figure 4.28: Calculated FFT of the signal on channel O1 during sleep at 23:46 pm. The subject is lying on the bed with closed eyes and in a drowsiness state. The signal has been band-pass filtered between 0.2 Hz and 25 Hz and the averaged signal has been subtracted from it. The region of brain waves are illustrated here. Higher theta and alpha signals are observable.

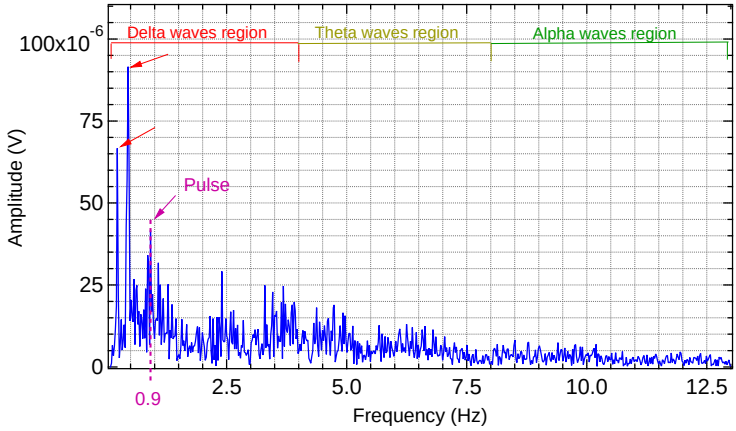

Figure 4.29: Calculated FFT of the signal on channel O1 during sleep at 00:18 am. The signal has been band-pass filtered between 0.2 Hz and 25 Hz and the averaged signal has been subtracted from it. The high level of the observed delta waves indicates that the test person is in deep sleep, stage 3 and 4.

5 Conclusion and Outlook

This thesis is concerned with the optimization of capacitive non-contact electrodes for biosignal measurements as well as the implementation of a textile capacitive EEG hat using these optimized electrodes.
In this thesis, a comprehensive noise model of capacitive non-contact electrodes for bioelectric potential measurements is introduced. This model explains the noise characteristics of the capacitive and textile capacitive electrodes in the frequency range of 0.1 Hz to 50 kHz. In the white noise regime above 1 kHz, the noise spectrum is dominated by the white noise level of the employed operational amplifier with its very high input impedance. At lower frequencies, an increase of the noise voltage is observed, which can be explained by the low pass filter behavior of the parasitic electronic network of such an electrode. In the frequency range between 1 Hz and 5 kHz, the fluctuation of charges on the surface of the electrode is increasing the noise level. The fluctuation of charges only increases with the increase of the electrode surface area and is not dependent on the dielectric material or edge length of the electrode surface. At very low frequencies, the voltage noise shows no frequency dependence due to the dominating white noise contribution of the bias resistor.

The cut-off frequency of the high-pass filter of the capacitive electrode is determined by the input capacitor, which originates from the electrode surface parallel to the body surface, and input resistor. In order to have a lower cut-off frequency and to reduce the voltage noise at around 10 Hz, the value of the input resistor or capacitor should be increased. An increase in the bias resistance, increases the voltage noise at lower frequencies. Therefore, it is more desirable to choose a high input capacity. The use of conductive fabric as an electrode surface, allows the enlargement of the electrode surface quite considerably while maintaining a small average effective distance. This consequently results in a well defined and larger input capacity, though, the larger surface area of the textile electrodes increases the $1/\sqrt{f}$-voltage noise. If the flexible surface of the electrode is large enough, the value of the bias resistor can be reduced. The com-

bination of the lower bias resistance and higher input capacity in textile electrodes results in a considerable reduction of the voltage noise.
To use the outstanding benefits and unique characteristics of the textile capacitive electrodes in practice, an EEG measuring device is implemented in the form of a hat. The introduced capacitive EEG hat uses eight low noise textile capacitive electrodes each with a surface size of $32\,\mathrm{cm}^2$ for the measurement of brain signals. One of these electrodes, which is placed at the front part of the hat, is used as a reference electrode. The output of the other seven electrodes is compared to this electrode for the reduction of common mode disturbances. The measured signals are sent wirelessly via bluetooth to a computer for further processing and evaluation.
The elasticity of the hat allows it to fit to many different sizes and shapes of the heads without being uncomfortable. This, in addition to the light weight of the cEEG hat, makes very long measurements possible. Long term measurements are especially important for BCI applications and EEG measurements during sleep, which may take several hours. The applicability of this cEEG hat in BCI and EEG measurements during sleep, are demonstrated in this thesis by several SSVEP measurements, and EEG measurements during sleep on all the channels at two different times.
The EEG hat makes use of a shielding layer that covers the whole electrodes and electronics. This shielding layer reduces electrical disturbances considerably and allows EEG measuring in electrically noisier situations outside laboratories.
The effect of pulse wave disturbance is apparent in the measurements at low frequencies. This effect is especially observable because of the light weight of the cEEG hat and little amount of pressure that this hat applies to the head. Since the important brain waves are also at lower frequencies, it makes the filtering of pulse waves more challenging. Since this disturbance appears on all the electrodes, an average signal of multiple channels, which do not have interesting biosignals for each measurement, is calculated and subtracted from the remaining channels. This method reduces the pulse wave disturbance considerably.
To better profit from the ICA algorithm, a simultaneous ECG measurement is beneficial. Therefore, it is recommended to add this feature to the EEG hat in the future.
The implemented EEG hat provides seven measuring channels, however, this number can be expanded and more textile electrodes can be included inside the hat. In this way, each individual electrode will have a smaller surface, nevertheless, due to the flexibility of the electrode surfaces, the effective distance between them and the skull remains constant and small over the surface. Therefore, the input capacities of the electrodes will be higher compared to rigid electrodes even with a same size.
Producing EEG hats in different sizes is another improvement that should be considered in the future. The introduced EEG hat is suitable for a normal size of an adult head. For children, teenagers, or people with over sized heads, other EEG hats should be realized. Since the electrodes and electronics can be easily dismantled from the cEEG hat, only different sizes of the hat with pockets for electrodes should be provided.

Concerning the software, there is a wide range of improvements possible. The software used in this thesis is adequate for receiving data from the cEEG hat and the evaluation of these data. Though, using these data in different applications and also the on line presentation and evaluation of them can still be improved.
In this work, the applicability of the EEG hat in different situations and fields is shown. Yet, clinical surveys with a larger number of test persons are pending.

Scientific publications

- S. N. Asl, F. Ludwig, and M. Schilling:
  Noise properties of textile, capacitive EEG electrodes
  Current Directions in Biomedical Engineering, vol. 1, pp. 34–37, 2015
- S. N. Asl, M. Oehler, and M. Schilling:
  Noise Model of Capacitive and Textile Capacitive Noncontact Electrodes for Bioelectric Applications
  IEEE Transactions on Biomedical Circuits and Systems,pp. 851–859, 2018

List of Figures

List of Tables

References

[1] H. Moldofsky, L. Rothman, R. Kleinman, S. G. Rhindand, and J. D. Richardson, "Disturbed EEG sleep, paranoid cognition and somatic symptoms identify veterans with post-traumatic stress disorder", *BJPsych Open*, vol. 2, pp. 359–365, 2016 (page 1).

[2] L. Tarokh, J. M. Saletin, and M. A. Carskadon, "Sleep in adolescence: physiology, cognition and mental health", *Neurosci Biobehav*, vol. 70, pp. 182–188, 2016 (page 1).

[3] G. Luca, J. H. Rubio, D. Andries, N. Tobback, P. Vollenweider, G. Waeber, P. M. Vidal, M. Preisig, R. Heinzer, and M. Tafti, "Age and gender variations of sleep in subjects without sleep disorders", *Annals of Medicine*, vol. 47, no. 6, pp. 482–491, 2015, PMID: 26224201 (page 1).

[4] G. Roks, E. S. C. Korf, W. M. van der Flier, P. Scheltens, and C. J. Stam, "The use of EEG in the diagnosis of dementia with Lewy bodies", *Journal of Neurology, Neurosurgery & Psychiatry*, vol. 79, no. 4, pp. 377–380, 2008 (page 1).

[5] M. Modarreszadeh and R. N. Schmidt, "Wireless, 32-channel, EEG and epilepsy monitoring system", in *Proceedings of the 19th Annual International Conference of the IEEE Engineering in Medicine and Biology Society. 'Magnificent Milestones and Emerging Opportunities in Medical Engineering' (Cat. No.97CH36136)*, vol. 3, 1997, pp. 1157–1160 (page 1).

[6] A. A. Raymond, D. R. Fish, S. M. Sisodiya, N. Alsanjari, J. Stevens, and S.D.Shorvon, "Abnormalities of gyration, heterotopias, tuberous sclerosis, focal cortical dysplasia, microdysgenesis, dysembryoplastic neuroepithelial tumour and dysgenesis of the archicortex in epilepsy: Clinical, EEG and neuroimaging features in 100 adult patients", *Brain*, vol. 118, no. 3, pp. 629–660, 1995 (page 1).

[7] K. K. Ang, K. S. G. Chua, K. S. Phua, C. Wang, Z. Y. Chin, C. W. K. Kuah, W. Low, and C. Guan, "A Randomized Controlled Trial of EEG-Based Motor Imagery Brain-Computer Interface Robotic Rehabilitation for Stroke", *Clinical EEG and Neuroscience*, vol. 46, no. 4, pp. 310–320, 2015, PMID: 24756025 (page 1).

[8] F. Pichiorri, G. Morone, M. Petti, J. Toppi, I. Pisotta, M. Molinari, S. Paolucci, M. Inghilleri, L. Astolfi, F. Cincotti, and D. Mattia, "Brain-computer interface boosts motor imagery practice during stroke recovery", *Annals of Neurology*, vol. 77, no. 5, pp. 851–865, 2015 (page 1).

[9] J. R. Wolpaw, R. S. Bedlack, D. J. Reda, R. J. Ringer, P. G. Banks, T. M. Vaughan, S. M. Heckman, L. M. McCane, C. S. Carmack, S. Winden, D. J. McFarland, E. W. Sellers, H. Shi, T. Paine, D. S. Higgins, A. C. Lo, H. S. Patwa, K. J. Hill, G. D. Huang, and R. L. Ruff, "Independent home use of a brain-computer interface by people with amyotrophic lateral sclerosis", *Neurology*, vol. 91, no. 3, e258–e267, 2018 (page 1).

[10] C. Chen, M. Xue, Y. Wen, G. Yao, Y. Cui, F. Liao, Z. Yan, L. Huang, S. A. Khan, M. Gao, T. Pan, H. Zhang, W. Jing, D. Guo, S. Zhang, H. Yao, X. Zhou, Q. Li, Y. Xia, and Y. Lin, "A Ferroelectric Ceramic Polymer Composite-Based Capacitive Electrode Array for In Vivo Recordings", *Advanced Healthcare Materials*, vol. 6, no. 16, p. 1 700 305, 2017 (page 1).

[11] E. Yin, Z. Zhou, J. Jiang, Y. Yu, and D. Hu, "A Dynamically Optimized SSVEP Brain Computer Interface (BCI) Speller", *IEEE Transactions on Biomedical Engineering*, vol. 62, no. 6, pp. 1447–1456, 2015 (page 1).

[12] X. Chen, Y. Wang, M. Nakanishi, X. Gao, T.-P. Jung, and S. Gao, "High-speed spelling with a noninvasive brain computer interface", *Proceedings of the National Academy of Sciences*, vol. 112, no. 44, E6058–E6067, 2015 (page 1).

[13] J. J. S. Norton, D. S. Lee, J. W. Lee, W. Lee, O. Kwon, P. Won, S.-Y. Jung, H. Cheng, J.-W. Jeong, A. Akce, S. Umunna, I. Na, Y. H. Kwon, X.-Q. Wang, Z. Liu, U. Paik, Y. Huang, T. Bretl, W.-H. Yeo, and J. A. Rogers, "Soft, curved electrode systems capable of integration on the auricle as a persistent brain computer interface", *Proceedings of the National Academy of Sciences*, 2015 (page 1).

[14] H. T. Epstein, "Stages in human brain development", *Developmental Brain Research*, vol. 30, no. 1, pp. 114–119, 1986 (page 1).

[15] A. Meyer-Lindenberg, "The evolution of complexity in human brain development: an EEG study", *Electroencephalography and Clinical Neurophysiology*, vol. 99, pp. 405–411, 1996 (page 1).

[16] N. S. Suhaimi, C. T. B. Yuan, J. Teo, and J. Mountstephens, "Modeling the affective space of 360 virtual reality videos based on arousal and valence for wearable EEG-based VR emotion classification", *2018 IEEE 14th International Colloquium on Signal Processing Its Applications (CSPA)*, pp. 167–172, 2018 (page 1).

[17] S. Iranmanesh and E. Rodriguez-Villegas, "A 950 nW Analog-Based Data Reduction Chip for Wearable EEG Systems in Epilepsy", *IEEE Journal of Solid-State Circuits*, vol. 52, no. 9, pp. 2362–2373, 2017 (page 1).

[18] J. Xu, S. Mitra, C. V. Hoof, R. F. Yazicioglu, and K. A. A. Makinwa, "Active Electrodes for Wearable EEG Acquisition: Review and Electronics Design Methodology", *IEEE Reviews in Biomedical Engineering*, vol. 10, pp. 187–198, 2017 (page 1).

[19] V. P. Rachim, Y. Jiang, H.-S. Lee, and W.-Y. Chung, "Demonstration of long-distance hazard-free wearable EEG monitoring system using mobile phone visible light communication", *Optics Express*, vol. 25, no. 2, pp. 713–719, 2017 (page 1).

[20] X. Zhang, J. Li, Y. Liu, Z. Zhang, Z. Wang, D. Luo, X. Zhou, M. Zhu, W. Salman, G. Hu, and C. Wang, "Design of a Fatigue Detection System for High-Speed Trains Based on Driver Vigilance Using a Wireless Wearable EEG", *Sensors*, vol. 17, no. 3, 2017 (page 1).

[21] S. M. Lee, J. H. Kim, C. Park, J. Hwang, J. S. Hong, K. H. Lee, and S. H. Lee, "Self-Adhesive and Capacitive Carbon Nanotube-Based Electrode to Record Electroencephalograph Signals From the Hairy Scalp", *IEEE Transactions on Biomedical Engineering*, vol. 63, no. 1, pp. 138–147, 2016 (page 1).

[22] U. Ha, Y. Lee, H. Kim, T. Roh, J. Bae, C. Kim, and H. Yoo, "A Wearable EEG-HEG-HRV Multimodal System With Simultaneous Monitoring of tES for Mental Health Management", *IEEE Transactions on Biomedical Circuits and Systems*, vol. 9, no. 6, pp. 758–766, 2015 (page 1).

[23] N. Meziane, J. G. Webster, M. Attari, and A. J. Nimunkar, "Dry electrodes for electrocardiography", *Physiological Measurement*, vol. 34, no. 9, R47, 2013 (pages 1–2).

[24] G. Li, B.-L. Lee, and W.-Y. Chung, "Smartwatch-Based Wearable EEG System for Driver Drowsiness Detection", *IEEE Sensors Journal*, vol. 15, no. 12, pp. 7169–7180, 2015 (page 2).

[25] Y. Chen, B. Lin, and J. Pan, "Novel Noncontact Dry Electrode With Adaptive Mechanical Design for Measuring EEG in a Hairy Site", *IEEE Transactions on Instrumentation and Measurement*, vol. 64, no. 12, pp. 3361–3368, 2015 (page 2).

[26] A. Searle and L. Kirkup, "A direct comparison of wet, dry and insulating bioelectric recording electrodes", *Physiological Measurement*, pp. 271–283, 2000 (pages 2, 14).

[27] M. Oehler, V. Ling, K. Melhorn, and M. Schilling, "A multichannel portable ECG system with capacitive sensors", *Physiological Measurement*, vol. 29, no. 7, pp. 783–793, 2008 (pages 2, 17).

[28] H. J. Baek, H. S. Kim, J. Heo, Y. G. Lim, and K. S. Park, "Brain-computer interfaces using capacitive measurement of visual or auditory steady-state responses", *Journal of Neural Engineering*, vol. 10, no. 2, p. 024 001, 2013 (page 2).

[29] Y. G. Lim, K. K. Kim, and K. S. Park, "ECG Measurement on a chair without Conductive Contact", *IEEE Transactions on Biomedical Engineering*, vol. 53, pp. 956–959, 2006 (page 2).

[30] C. J. Harland, T. D. Clark, N. S. Peters, M. J. Everitt, and P. B. Stiffell, "A compact electric potential sensor array for the acquisition and reconstruction of the 7–lead electrocardiogram without electrical charge contact with the skin", *Physiological Measurement*, vol. 26, pp. 939–950, 2005 (page 2).

[31] J. H. Kim, S. M. Lee, and S. H. Lee, "Capacitive monitoring of bio and neuro signals", *Biomedical Engineering Letters*, vol. 4, pp. 142–148, 2014 (page 2).

[32] B. Babusiak, M. Gala, M. Penhaker, M. Cerny, and J. Kraus, "Indirect-Contact Surface Electrocardiography Measurements by Capacitive Electrodes", in *The 15th International Conference on Biomedical Engineering: ICBME 2013, 4th to 7th December 2013, Singapore*, J. Goh, Ed. Cham: Springer International Publishing, 2014, pp. 663–666 (page 2).

[33] M. Walter, B. Eilebrecht, T. Wartzek, and S. Leonhardt, "The smart car seat: personalized monitoring of vital signs in automotive applications", *Personal and Ubiquitous Computing*, vol. 15, no. 7, pp. 707–715, 2011 (page 2).

[34] B. Chamadiya, S. Heuer, U. G. Hofmann, and M. Wagner, "Towards a capacitively coupled electrocardiography system for car seat integration", in *4th European Conference of the International Federation for Medical and Biological Engineering*, J. V. Sloten, P. Verdonck, M. Nyssen, and J. Haueisen, Eds., Berlin, Heidelberg: Springer Berlin Heidelberg, 2009, pp. 1217–1221 (page 2).

[35] M. Naangmenkpeong, S.-I. Kim, J.-S. Park, Y.-H. Joung, and W. S. Choi, "Electrode Characteristics of Non-contact Electrocardiographic Measurement", *IEEE Transactions on Electron Devices*, vol. 16, pp. 42–45, 2015 (page 2).

[36] V. P. Rachim and W. Y. Chung, "Wearable Noncontact Armband for Mobile ECG Monitoring System", *IEEE Transactions on Biomedical Circuits and Systems*, vol. 10, no. 6, pp. 1112–1118, 2016 (page 2).

[37] P. Richardson, "Some new electrode techniques for long-term physiological monitoring", *Aerospace Med.*, vol. 39, pp. 745–750, 1968 (pages 2, 15).

[38] L. A. Geddes and L. E. Baker, *Principles of applied biomedical instrumentation*, 3rd ed. Wiley New York, 1989 (pages 2, 13).

[39] T. J. Sullivan, S. R. Deiss, and G. Cauwenberghs, "A Low-Noise, Non-Contact EEG/ECG Sensor", *2007 IEEE Biomedical Circuits and Systems Conference*, pp. 154–157, 2007 (page 2).

[40] B. Eilebrecht, J. Willkomm, A. Pohl, T. Wartzek, and S. Leonhardt, "Impedance Measurement System for Determination of Capacitive Electrode Coupling", *IEEE Transactions on Biomedical Circuits and Systems*, vol. 7, no. 5, pp. 682–689, 2013 (page 2).

[41] Y. M. Chi, C. Maier, and G. Cauwenberghs, "Ultra-high input impedance, low noise integrated amplifier for noncontact biopotential sensing", *IEEE Journal on Emerging and Selected Topics in Circuits and Systems*, vol. 1, no. 4, pp. 526–535, 2011 (page 2).

[42] K.-R. Mueller, B. Blankertz, G. Curio, and M. Schilling, "Sensor system and methods for the capacitive measurement of electromagnetic signals having a biological origin", pat. PCT/DE2005/002319, 2009 (page 2).

[43] S. N. Asl, M. Oehler, and M. Schilling, "Noise Model of Capacitive and Textile Capacitive Noncontact Electrodes for Bioelectric Applications", *IEEE Transactions on Biomedical Circuits and Systems*, pp. 851–859, 2018 (pages 2, 15, 17, 42, 55–62, 64–65, 67).

[44] S. N. Asl, F. Ludwig, and M. Schilling, "Noise properties of textile, capacitive EEG electrodes", *Current Directions in Biomedical Engineering*, vol. 1, pp. 34–37, 2015 (pages 2, 17–18).

[45] H. Li, X. Chen, L. Cao, C. Zhang, C. Tang, E. Li, X. Feng, and H. Liang, "Textile-based ECG acquisition system with capacitively coupled electrodes", *Transactions of the Institute of Measurement and Control*, vol. 39, no. 2, pp. 141–148, 2017 (page 2).

[46] M. Gerloff, "Kapazitives EEG-Helmsystem für BCI-Anwendungen", PhD thesis, Technische Universität Carolo-Wilhelmina Braunschweig, 2017 (pages 2, 19–20).

[47] M. Oehler, "Kapazitive Elektroden zur Messung bioelektrischer Signale", PhD thesis, Technische Universität Carolo-Wilhelmina Braunschweig, 2009 (pages 2, 14, 17, 19–20, 59–61).

[48] K. Olze, "Erzeugung, Erfassung und interindividuelle Übertragung von Biosignalen", PhD thesis, Technische Universität Carolo-Wilhelmina Braunschweig, 2017 (pages 2, 20, 50, 52, 77).

[49] C. J. Wehrmann, "Aufbau eines drahtlosen kapazitiven Helmsystems", Master's thesis, Technische Universität Carolo-Wilhelmina Braunschweig, 2011 (pages 2, 14, 19–20, 50, 52).

[50] M. Walter, B. Eilebrecht, T. Wartzek, and S. Leonhardt, "The smart car seat: personalized monitoring of vital signs in automotive applications", *Personal and Ubiquitous Computing*, vol. 15, pp. 707–715, 2011 (page 2).

[51] T. Wartzek, B. Eilebrecht, J. Lem, H. Lindner, S. Leonhardt, and M. Walter, "ECG on the Road: Robust and Unobtrusive Estimation of Heart Rate", *IEEE Transactions on Biomedical Engineering*, vol. 58, no. 11, pp. 3112–3120, 2011 (page 2).

[52] T. Matsuda and M. Makikawa, "ECG monitoring of a car driver using capacitively-coupled electrodes", in *2008 30th Annual International Conference of the IEEE Engineering in Medicine and Biology Society*, 2008, pp. 1315–1318 (page 2).

[53] D. T. Godin, P. A. Parker, and R. N. Scott, "Noise characteristics of stainless-steel surface electrodes", *Medical and Biological Engineering and Computing*, vol. 29, no. 6, pp. 585–590, 1991 (page 2).

[54] C. Gondran, E. Siebert, S. Yacoub, and E. Novakov, "Noise of surface bio-potential electrodes based on NASICON ceramic and Ag-AgCl", *Medical and Biological Engineering and Computing*, vol. 34, no. 6, pp. 460–466, 1996 (page 2).

[55] E. Huigen, "Noise in biopotential recording using surface electrodes", PhD thesis, University of Amsterdam Section Medical Physics, 2000 (page 2).

[56] E. Huigen, A. Peper, and C. A. Grimbergen, "Investigation into the origin of the noise of surface electrodes", *Medical and Biological Engineering and Computing*, vol. 40, no. 3, pp. 332–338, 2002 (page 2).

[57] J. Clark, "The origin of biopotentials", *Medical Instrumentation: Application and Design*, pp. 126–188, 1998 (pages 5–12, 15).

[58] A. L. Hodgkin and A. F. Huxley, "A quantitative description of membrane current and its application to conduction and excitation in nerve", *The Journal of Physiology*, vol. 117(4), pp. 500–544, 1952 (page 6).

[59] J. H. Schwartz, S. A. Siegelbaum, and A. J. Hudspeth, *Principles of Neural Science, Fifth Edition*, E. R. Kandel, T. M. Jessell, J. H. Schwartz, S. A. Siegelbaum, and A. J. Hudspeth, Eds. McGraw Hill Professional, 2013 (page 7).

[60] B. Henning, S. Anastasiadou, and C. M. zu Reckendorf, *Faszinierendes Gehirn: Eine bebilderte Reise in die Welt der Nervenzellen.* Springer Spektrum, 2016 (page 7).

[61] H. Berger, "Über das Elektrenkephalogramm des Menschen", *Archiv für Psychiatrie und Nervenkrankheiten*, vol. 87, no. 1, pp. 527–570, 1929 (page 8).

[62] E. K. S. Louis and L. C. Frey, *Electroencephalography(EEG): An introductory text and atlas of normal and abnormal findings in adults, children and infants.* Chicago IL: American Epilepsy Societ, 2016 (pages 9, 12, 14–15, 20).

[63] S. Zschocke, *Klinische Elektroenzephalographie*. Springer, 2012 (pages 9, 12, 16).

[64] J. S. Kumar and P. Bhuvaneswari, "Analysis of Electroencephalography (EEG) Signals and Its Categorization - A Study", *Procedia Engineering*, vol. 38, pp. 2525–2536, 2012 (pages 10–11).

[65] I. Feinberg and T. Floyd, “Systematic Trends Across the Night in Human Sleep Cycles”, *Psychophysiology*, vol. 16, pp. 283–291, 1979 (page 12).

[66] E. Hartmann, “The 90-minute sleep-dream cycle”, *Archives of General Psychiatry*, vol. 18, no. 3, pp. 280–286, 1968 (page 12).

[67] J. V. Odom, M. Bach, C. Barber, M. Brigell, M. F. Marmor, A. P. Tormene, G. E. Holder, and Vaegan, “Visual evoked potentials standard”, *Documenta Ophthalmologica*, vol. 108, pp. 115–123, 2004 (page 13).

[68] M. Stöhr, J. Dichgans, U. W. Buettner, and C. W. Hess, *Evozierte Potenziale*, 4th ed. Springer, 2005 (page 13).

[69] C. S. Herrmann, “Human eeg responses to 1-100 Hz flicker: Resonance phenomena in visual cortex and their potential correlation to cognitive phenomena.”, *Experimental Brain Research*, vol. 137(3-4), pp. 346–353, 2001 (page 13).

[70] K. Maurer, N. Lang, and J. Eckert, *Praxis der evozierten Potentiale*, 2nd ed. Springer, 2005 (page 13).

[71] Y. M. Chi, T. P. Jung, and G. Cauwenberghs, “Dry-Contact and Noncontact Biopotential Electrodes: Methodological Review”, *IEEE Reviews in Biomedical Engineering*, vol. 3, pp. 106–119, 2010 (page 14).

[72] H. Helmholtz, “Studien über Electrische Grenzschichten”, *Annalen der Physik und Chemie*, pp. 337–382, 1879 (page 14).

[73] R. M. David and W. M. Portnoy, “Insulated electrocardiogram electrodes”, *Medical and biological engineering*, vol. 10, no. 6, pp. 742–751, 1972 (page 15).

[74] H. J. Baek, H. J. Lee, Y. G. Lim, and K. S. Park, “Conductive Polymer Foam Surface Improves the Performance of a Capacitive EEG Electrode”, *IEEE Transaction on Biomedical Engineering*, vol. 59, no. 12, pp. 3422–3431, 2012 (page 17).

[75] P. Husar, *Biosignalverarbeitung*. Springer Berlin Heidelberg, 2010 (page 20).

[76] B. Carter, “Op Amp for Everyone”, in. Texas Instrument, 2003, ch. Op Amp Noise Theory and Applications, pp. 123–145 (pages 21, 23, 56).

[77] W. Schottky, “Über spontane Stromschwankungen in verschiedenen Elektrizitätsleitern”, *Annalen der Physik*, vol. 362, no. 23, pp. 541–567, 1918 (page 22).

[78] H. W. Ott, *Noise reduction techniques in electronic systems*, 2. ed. New York: Wiley, 1988 (pages 21, 23–25, 65).

[79] P. Stoica and R. Moses, *Spectral analysis of signals*, T. Robbins, Ed. Prentice Hall, 2005 (pages 25, 29, 32).

[80] *Spectrum Analysis Basics*, Keysight Technologies, 2016 (pages 25–28).

[81] C. Rauscher, V. Janssen, and R. Minihold, *Grundlagen der Spektrumanalyse*. Rohde & Schwarz, 2007 (page 26).

[82] A. V. Oppenheim and R. W. Schafer, *Discrete-time Signal Processing*. Prentice Hall, 1989 (pages 29, 32).

[83] G. Heinzel, A. Rüdiger, and R. Schilling, "Spectrum and spectral density estimation by the Discrete Fourier transform (DFT), including a comprehensive list of window functions and some new flat-top windows.", Max-Planck-Institut fur Gravitationsphysik (Albert-Einstein-Institut) Teilinstitut Hannover, Tech. Rep., 2002 (pages 29–30, 32, 34–37, 39).

[84] P. D. Welch, "The Use of Fast Fourier Transform for the Estimation of Power Spectra: A Method Based on Time Averaging Over Short, Modified Periodograms", *IEEE TRANSACTIONS ON AUDIO AND ELECTROACOUSTICS*, vol. AU-15, no. 2, pp. 70–73, 1967 (page 29).

[85] A. Quinquis, "Power Spectral Density Estimation", in *Digital Signal Processing using MATLAB*. Wiley-Blackwell, 2013, ch. 10, pp. 241–278 (pages 29, 32, 36).

[86] R. G. Lyons, *Understanding digital signal processing*. Prentice Hall, 1997 (pages 30, 39).

[87] F. Harris, "On the Use of Windows for Harmonic Analysis With the Discrete Fourier Transform", *Proceedings of the IEEE*, vol. 66, pp. 51–83, 1978 (pages 35–36).

[88] *Shieldex Knitted Fabrics*, Statex Produktions & Vertriebs GmbH, Kleiner Ort 11 28357 Bremen Germany (page 46).

[89] C. L. Pudwell, "Textiler cEEG-Helm", Master's thesis, Technische Universität Carolo-Wilhelmina Braunschweig, 2018 (page 49).

[90] *Composite PLA - Electrically Conductive Graphite*, Accessed 10. November 2016, ProtoPlant, makers of Proto-pasta (page 50).

[91] X. Liu, A. Demosthenous, and N. Donaldson, "Platinum electrode noise in the ENG spectrum", *Medical Biological Engineering Computing*, vol. 46, no. 10, pp. 997–1003, 2008 (page 55).

[92] A. Hassibi, R. Navid, R. W. Dutton, and T. H. Lee, "Comprehensive study of noise processes in electrode electrolyte interfaces", *Journal of Applied Physics*, vol. 96, no. 2, pp. 1074–1082, 2004 (page 55).

[93] A. I. Ianov, H. Kawamoto, and Y. Sankai, "Development of noise resistant hybrid capacitive-resistive electrodes for wearable robotics, computing and welfare", *RSJ International Conference on Intelligent Robots and Systems*, pp. 4249–4254, 2013 (page 55).

[94] M. C. Medeiros, A. Mestre, P. Inácio, S. Asgarif, I. M. Araújo, P. C. Hubbard, Z. Velez, M. L. Cancela, P. R. Rocha, D. M. de Leeuw, F. Biscarini, and H. L. Gomes, "An electrical method to measure low-frequency collective and synchronized cell activity using extracellular electrodes", *Sensing and Bio-Sensing Research*, vol. 10, pp. 1–8, 2016 (page 55).

[95] *http://www.analog.com/media/en/training-seminars/*, Analog Devices (page 56).

[96] F. N. Hooge, "1/f noise sources", *IEEE Transactions on Electron Devices*, vol. 41, no. 11, pp. 1926–1935, 1994 (page 66).

[97] F. N. Hooge, T. G. M. Kleinpenning, and L. K. J. Vandamme, "Experimental studies on 1/f noise", *Reports on Progress in Physics*, vol. 44, no. 5, pp. 479–532, 1981 (page 66).

[98] S. Butterworth, "On the theory of filter amplifiers", *Experimental Wireless and the Wireless Engineer*, vol. 7, pp. 536–541, 1930 (page 74).

[99] M. Ungureanu, C. Bigan, R. Strungaru, and V. Lazarescu, "Independent Component Analysis Applied in Biomedical Signal Processing", *Measurement science review*, vol. 4, pp. 1–8, 2004 (page 74).

[100] *https://martinos.org/mne/stable/generated/mne.preprocessing.ICA.html* (page 74).

[101] *https://sccn.ucsd.edu/wiki/Chapter-09:-Decomposing-Data-Using-ICA* (page 75).

[102] K. Olze, C. J. Wehrmann, L. Mu, and M. Schilling, "Obstacles in using a computer screen for steady state visually evoked potential stimulation", *Biomedical Engineering / Biomedizinische Technik*, vol. 63, pp. 377–382, 2017 (page 77).